Thesis for The Degree of Doctor of Philosophy

Localized dynamics of organic cations in metal halide perovskites

Investigated using neutron scattering techniques

Kanming Shi

Department of Chemistry and Chemical Engineering
Chalmers University of Technology
Gothenburg, Sweden, 2026

Localized dynamics of organic cations in metal halide perovskites
Investigated using neutron scattering techniques

Kanming Shi

ISBN 978-91-8103-392-2
Doktorsavhandlingar vid Chalmers tekniska högskola, Ny serie nr 5849.
ISSN 0346-718X

Department of Chemistry and Chemical Engineering
Chalmers University of Technology
SE-412 96 Göteborg
Sweden
Phone: +46(0)31 772 1000

Cover:
Neutrons are scattered by a virtual structure of metal halide perovskite. The Lorentzian functions approximately to the dynamical structure factor are shouwn in the background.

Printed by Chalmers Digitaltryck
Gothenburg, Sweden 2026.

Localized dynamics of organic cations in metal halide perovskites

Investigated using neutron scattering techniques

Kanming Shi

Department of Chemistry and Chemical Engineering
Chalmers University of Technology

Abstract

Metal halide perovskites (MHPs) are currently accumulating significant attention in the last decade because of their excellent optoelectronic properties and great potential for applications in, for example, solar cells and light-emitting diodes. However, the nature of local structure and dynamics underpinning these optoelectronic properties remain insufficiently understood.

This thesis focuses on investigations of local structure and dynamics in some important MHP materials, by using quasielastic neutron scattering (QENS) and inelastic neutron scattering (INS) techniques. More specifically, the QENS studies focus on the lower-dimensional MHPs $MBAMnCl_3 \cdot 2H_2O$, $A PbBr_4$ (A = 1,3-PDA; 1,4-PDA; 1,3-XDA; 1,4-XDA) and $(1,3-\mathrm{XDA})_2PbBr_6$. Further QENS studies have been performed on the three-dimensional (3D) lead-free MHPs $FASnX_3$ (X= Br, I), the vacancy-ordered double perovskite variant FA_2SnI_6. The INS study with a *in-situ* illuminance environment has performed on a prototypical 3D MHP $MAPbBr_3$.

For $MBAMnCl_3 \cdot 2H_2O$, the results unraveled the nature of rotational dynamics of the MBA cations and how they evolve with temperature. Specifically, it is shown that the dynamics evolve from the functional groups -NH_3, -CH_3 rotational diffusion to a coupled multi-axial reorientation of the entire cation.

For $A PbBr_4$ (A = 1,3-PDA; 1,4-PDA; 1,3-XDA; 1,4-XDA) and $(1,3-\mathrm{XDA})_2PbBr_6$, it is shown that the nature of the organic cation dynamics can be correlated to the length and symmetry of the respective cation. Additionally, a comparison of the dynamical results with the photoluminescent spectra of the materials indicate that slower dynamics correlate with a lower thermal stability of photoluminescence due to less dynamic disorder.

For $FASnX_3$ (X= Br, I) and FA_2SnI_6 the QENS results unravel the reorientational dynamics of the FA cations and how they depend on halide ion and vacancy-ordering, which modify the ratio of organic cation and the volume of the sublattice cavity.

In the study of $MAPbBr_3$, for which the effect of light illumination on the local structure and vibrational dynamics was investigated, the INS results reveal a small yet distinct change of the local coordination of the MA cations upon light illumination and polaron formation.

Keywords

molecular dynamics, quasielastic neutron scattering, inelasic neutron scattering, metal halide perovskite, photoelectric conversion

List of Papers

Appended papers

This thesis is based on the following papers:

I **K. Shi**, W. Cai, J. Qin, F. Juranyi, F. Gao, and M. Karlsson, *Reorientational Dynamics of Methylbenzylammonium Cations in the Chiral Metal Halide Composite* $MBAMnCl_3 \cdot 2H_2O$
Submitted.

II **K. Shi**, L. Malavasi, F. Juranyi, and M. Karlsson, *Rotational dynamics of diammonium cations in lead bromide composites investigated by quasi-elastic neutron scattering*
Phys. Chem. Chem. Phys., DOI:10.1039/D5CP04945H.

III **K. Shi**, R. Lavén, L. Malavasi, F. Juranyi, and M. Karlsson, *Rotational dynamics of formamidinium cations in* $FASnX_3$ *(X = Br, I) and* FA_2SnI_6 *type metal halide perovskites investigated with quasi-elastic neutron scattering*
In manuscript.

IV **K. Shi**, H. Cavaye, R. Lavén, and M. Karlsson, *Inelastic Neutron Scattering Study of the Optically Excited State of* $MAPbBr_3$
Submitted.

Contribution report

My contributions to the included papers:

I–IV I contributed to the planing of the neutron scattering experiments. I was the main responsible for data collection and analysis, and writing the first draft of the manuscript. For paper I, I also took part in the SC-XRD measurement.

In memory of my grandfather
Guoliang Deng (1937–2025)

Contents

List of Acronyms

e.g.	*exempli gratia* (for example)
EFWS	Elastic fixed window scan
EISF	Elastic incoherent structure factor
FA	Formamidinium
FWHM	Full width at half maximum
HWHM	Half width at half maximum
i.e.	*id est* (that is)
INS	Inelastic neutron scattering
J-PARC	Japan Proton Accelerator Research Complex
MA	Methylammonium
MBA	Methylbenzylammonium
MHP	Metal halide perovskite
PDA	Phenylenediammonium
PL	Photoluminescence
PSI	Paul Scherrer Institute
P-XRD	Powder X-ray diffraction
QENS	Quasielastic neutron scattering
SC-XRD	Single crystal X-ray diffraction
ToF	Time-of-flight
VESTA	Visualization for Electronic and Structure Analysis
XDA	Xylylenediammonium
XRD	X-ray diffraction

$\mathbf{n}^0$


^{1}H

Chapter 1

Introduction

"Nature uses only the longest threads to weave her patterns, so each small piece of her fabric reveals the organization of the entire tapestry."

Richard Feynman

From the celestial motions to the atomic vibrational modes, from the architecture of superclusters to the symmetries of crystal lattices, understanding the structure and dynamics of matter has remained a continual and foundational objective of scientific research. In a more practical context, a profound understanding of the structure and dynamics of materials facilitates the rational design, predictive modeling, and performance optimization of novel functional materials. Concurrently, rapid technological progress has further intensified the urgency of developing materials for high-efficiency and sustainable energy solutions, particularly with the recent surge in artificial intelligence (AI) technologies as supercomputer centers now demand massive amounts of electrical power.[1] Within this landscape, the study of photovoltaic materials represents one of the most impactful frontiers which enable the transduction of immense energy potential from the Sun into clean electrical power. Beyond energy conversion, these optoelectronic materials also play critical roles in diverse fields, including communication, advanced displays, and lighting.[2,3]

Perovskite is a class of material which has a special crystal structure. It was first discovered almost two hundred years ago as $CaTiO_3$,[4] and it has regained attention in the last decade due to its subclass of metal halide perovskites (MHPs, typical chemical formula: ABX_3 where A is usually an organic cation, B is a metal cation, and X is a halide ion), which exhibit outstanding potential in optoelectronic conversion devices.[5,6] The conversion efficiency of the semiconductor materials is a crucial property that directly impacts the performance of the device, where the efficiency of a single-junction solar cell based on MHPs has increased from 14% to 27% over the past thirteen years.[7*] Compared to other common inorganic semiconductors, one of the special characteristics of MHPs is the lattice softness, which results in low-energy optical phonons.[9,10] At room temperature, both the A-site cations and the metal-halide sub-lattice

*The theoretical efficiency limit for a single-junction solar cell, known as the Shockley-Queisser limit, is approximately 33.7%.[8]

exhibit pronounced dynamic disorder.[9] As a result, the system hosts a complex landscape of coupled interactions between the *A*-site cations, the inorganic sublattices, and various quasiparticles or excitations, including excitons, phonons, molecular rotors, and polarons. Meanwhile, as a critical research premise of these, the local structure and dynamics of most MHPs remain insufficiently understood.[11] This absence presents a profound challenge to deciphering the intricate internal interaction and coupling mechanism. Furthermore, the lack of fundamental understanding hinders the development, integration, and commercialization of devices based on these promising materials.

Neutron scattering is an advanced technique utilizing the neutron beams for investigating structural and dynamical properties of materials. Benefiting from its electrical neutrality and a mass on the same order as atomic nuclei, the neutron, in contrast to photons and electrons, enables momentum and energy transfer with the nuclei. This unique characteristic renders neutron scattering a powerful technique for probing both the crystal structure of materials and their internal dynamics, specifically across the picosecond to nanosecond timescales. On the other hand, owing to the significantly larger incoherent scattering cross-section of hydrogen compared to the other elements, neutrons are highly sensitive to, and frequently employed for investigating, the dynamics of organic molecules. Thus, neutron scattering has been broadly used in probing the cation dynamics and crystal structure of MHPs.[12–32] The aim of this thesis is to systematically measure, analyze, and understand the dynamical properties of different organic cations, including methylbenzylammonium ($C_6H_5CHCH_3NH_3^+$), phenylenediammonium ($C_6H_4(NH_3)_2^{2+}$), xylylenediammonium ($C_6H_4(CH_2NH_3)_2^{2+}$), formamidinium ($HC(NH_2)_2^+$), and methylammonium ($CH_3NH_3^+$), within some of the most promising MHPs on the picosecond timescales. Furthermore, this thesis comparatively investigates the correlations and interactions between the cation dynamics in MHPs and the intrinsic structures of the organic cations, the inorganic sub-lattices, and photogenerated excitons. The final aim is to construct a more comprehensive landscape that systematically describes what influences the organic cation dynamics and how they interact with their local environment, serving as the "small piece of fabric" envisioned by Feynman that advances our understanding of the interactions and couplings among the local dynamics, lattices, and quasiparticles in soft-lattice, dynamically disordered functional materials. The primary techniques employed for this study are quasielastic neutron scattering (QENS) and inelastic neutron scattering (INS).

Chapter 2

Metal halide perovskites

General characteristics

The word "perovskite" refers to a specific crystal structure first defined by Gustav Rose's discovery of the mineral calcium titanate ($CaTiO_3$) in 1839.* The crystal structure was first described in 1926 from Victor Goldschmidt's work on tolerance factors.[33] However, its structure determination was not achieved until 1945 when the crystal structure of the similar material barium titanate ($BaTiO_3$) was determined with XRD.[34]

Metal halide perovskites (MHPs) refer to perovskite structured materials, similar to $CaTiO_3$ and $BaTiO_3$, but with the oxide ion (O^{2-}) substituted for a halide ion (*e.g.* Cl^-, Br^-, and I^-). MHPs show great potential for application in optoelectronic conversion devices.[2,35] Specifically, by benefiting from a suitable and tunable bandgap, strong optical absorption, high defect tolerance, and high free charge carrier density, MHPs show excellent performance in generating, absorbing, and transferring photons and, hence, are promising for application in both solar cells and light-emitting diodes (LEDs).[6] Additionally, they are relatively easy to synthesize.[2,35]

With the increasing amount of research on MHPs over the last decade, the conversion efficiency record of MHP single-junction solar cells increased from 14.1% to 26.7% (Figure 2.1), which is close to the best recorded silicon-based solar cells (27.3%),[7] better than the conventional solar cell (14–19%) and close to the single bandgap efficiency limit of 32.9%.[36] Simultaneously, the photoluminescence (PL) quantum yield† of MHPs such as $MAPbBr_3$ (MA = methylammonium, $CH_3NH_3^+$) can approach 95-100%, which is promising towards application in high-performance MHP LED devices.[37,38] Additionally, due to MHPs generally high absorption/emission efficiency and high defect tolerance, they (*e.g.* $MAPbBr_3$ and $CsPbBr_3$) are promising for applications in lasers.[39–41] Owing to their tunable absorption, MHPs (*e.g.* $MAPbCl_3$ and $MAPbI_3$) have also achieved significant progress in the fields of photodetection in the ultraviolet and infrared regions, respectively.[42–44] Still, the extensive commercial application of MHPs in actual devices continues to encounter

*The name *perovskite* comes after another mineralogist named *Lev Perovski.*

†Quantum yield is the number of photons emitted as a fraction of the number of photons absorbed.

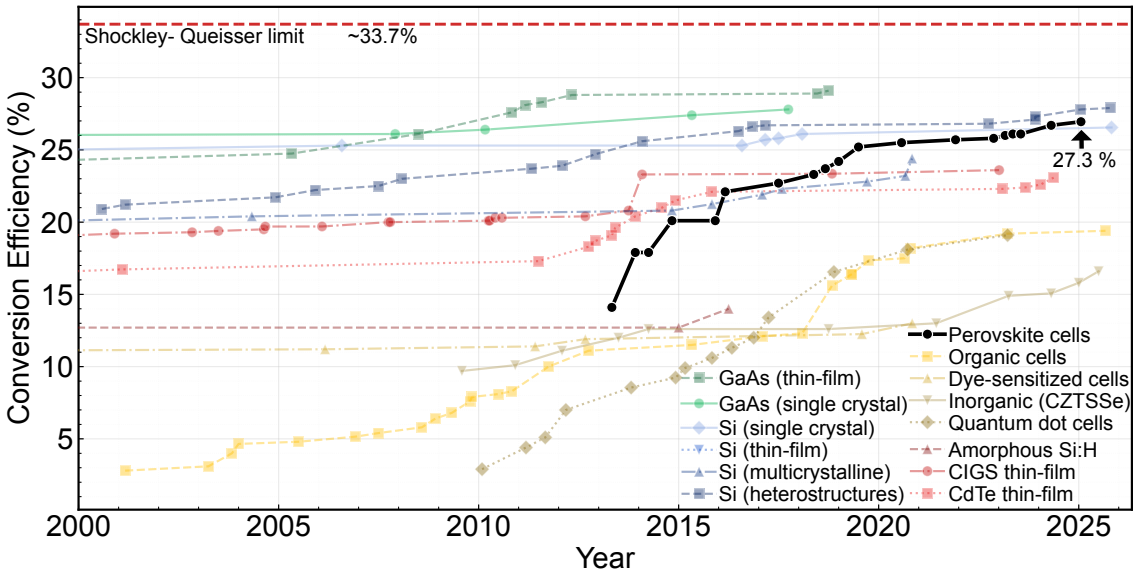

Figure 2.1: Chart of the highest confirmed conversion efficiencies for research single junction cells without solar power concentrator for a range of photovoltaic technologies, plotted from 2000 to 2025.[7] This plot is courtesy of the National Renewable Energy Laboratory, Golden, CO.

barriers because of their limited stability (especially in humid environments), large-scale device performance, and environmental hazard risk.

2.1 Structural properties

A typical MHP exhibits the three-dimensional (3D) ABX_3 perovskite structure where A is an organic cation (*e.g.* MA^+: methylammonium, FA^+: formamidinium) or an alkali metal cation (*e.g.* Cs^+, Rb^+), B is a divalent metal cation (*e.g.* Pb^{2+}, Sn^{2+}, and Mn^{2+}), and X is a halide anion (*e.g.* Cl^-, Br^-, and I^-). Each A-site cation is surrounded by eight $[BX_6]$ octahedra, where each divalent metal ion is located inside of the octahedron, and each anion is shared by 2 octahedra (Figure 2.2). Different modes of $[BX_6]$ octahedra connectivity may result in structures of lower dimensions. Two-dimensional (2D) MHPs are characterized by that each octahedron shares four vertexes with four other octahedra and expands in a plane (*e.g.* $[CH_3(CH_2)_8NH_3]_2PbI_4$), as shown in Figure 2.3.[45] One-dimensional (1D) MHPs are characterised by that each octahedron shares the vertex with the two closest octahedra shaped as a line structure (*e.g.* $C_4N_2H_{14}PbBr_4$).[46] For zero-dimensional (0D) MHPs, each octahedron does not connect or share any vertex to any other octahedra (*e.g.* Cs_4PbI_6).[47]

Several 3D MHPs have a cubic phase at relatively high temperatures and a tetragonal or orthorhombic phase at lower temperatures. For example, as shown in Figure 2.4, $MAPbI_3$ has an orthorhombic phase below 165 K, a tetragonal phase between 165 and 327 K, and a cubic phase above 327 K.[48] $FAPbI_3$ has a tetragonal phase below 151 K, another tetragonal phase (less distorted from

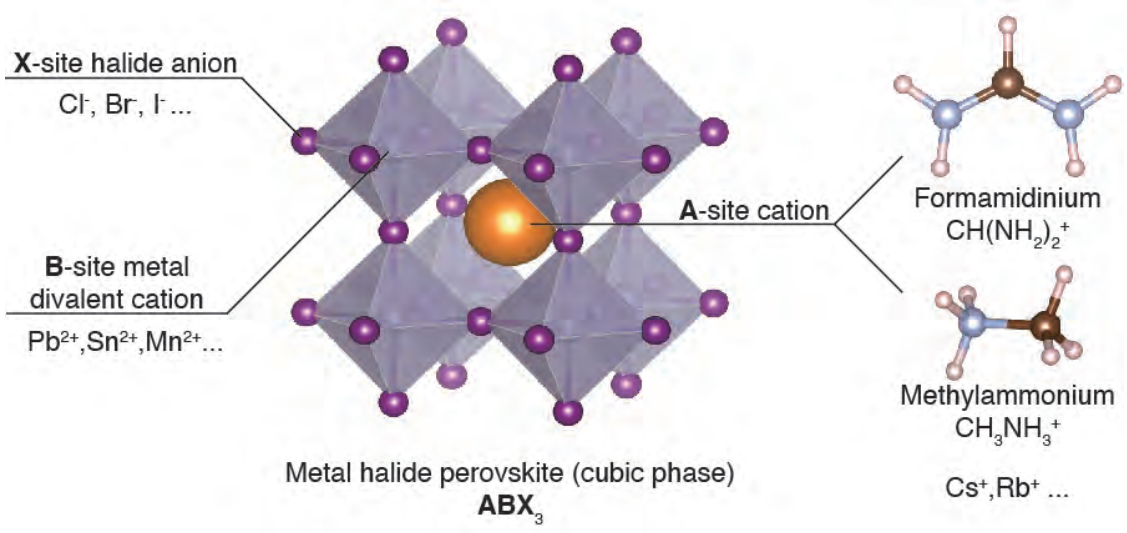

Figure 2.2: Schematic illustration of the cubic ABX_3 MHP structure. Color scheme: purple spheres (halide anions), gray spheres (metal cations), orange spheres (A-site cations), brown spheres (carbons), light blue spheres (nitrogens), light pink spheres (hydrogens).

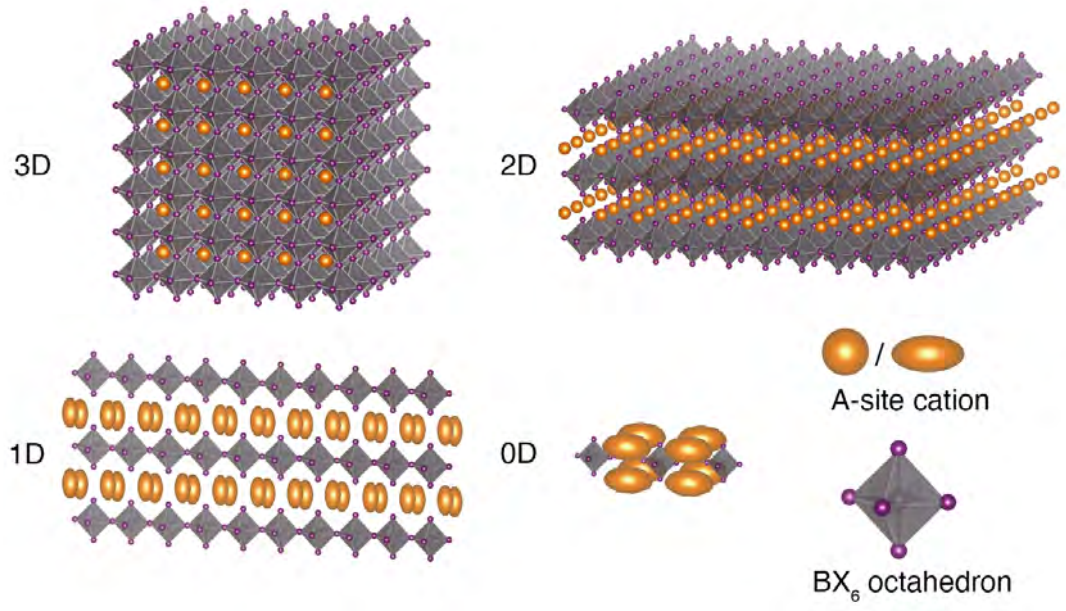

Figure 2.3: Schematic of the various "dimensionality" of MHPs. Color scheme: orange spheres/ellipsoids (A-site cations), gray spheres (B-site metal cations), purple spheres (X-site halide anions).

cubic phase) between 151 and 299 K, and a cubic phase above 299 K.[49] These different phase change temperatures, from the same inorganic sublattice but differnt A-site cations, show the clear relation from organic cation dynamics to the MHP structure aligned with the previous study.[12,13,27,30,31]

In the last decade, lower-dimensional MHPs have been proposed as alternatives to their 3D counterparts, because the benefit of their more stable

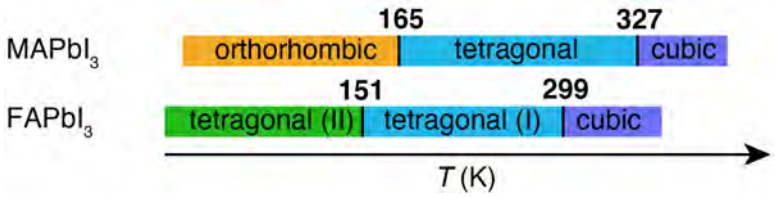

Figure 2.4: Phase transition temperatures diagram of $MAPbI_3$ [48] and $FAPbI_3$ [49].

exciton with fast radiative decay can improve the luminescence efficiency of this class of semiconductors. At the same time, the lower dimensional architecture gives them stability and relaxes geometrical constraints, giving access to a wider range of chemical compositions,[50] and has emerged as promising white phosphors.[51]

In addition to the effects that the octahedral framework has on the structure of MHPs, adjusting the A-site cation can also introduce unique structural and optoelectronic properties. Recently, there has been a growing trend of using chiral organic cations.[‡] Chiral MHPs are becoming attractive to researchers because of their unique characteristics including circular dichroism (CD), and circularly polarized PL spectrum.[52,53] Interestingly, studies have shown that the chirality of the organic cation is transferred to the inorganic sub-lattice, which implies that the luminescence is circularly polarized.[52] By adjusting the sequence of enantiomer (R or S) of the chiral organic cation in MHPs, the polarization direction of circularly polarized PL can be modulated.[52] Since the first chiral MHP s-methylbenzylammonium (Figure 2.5a) lead bromide ([(S)-MBA][$PbBr_3$]) was reported,[54] a series of 2D/1D chiral MHPs have indeed been developed.[52] Figure 2.5b shows the crystal structures of the 2D chiral MHPs (R-/(S)-MBA)PbI_3, as well as of the racemic composition ((R)-MBA)I:((S)-MBA)I = 1:1.[52] Though some reports about the dynamics in chiral MHPs have been published,[55,56] very little generally is known about the dynamics in these materials.

2.2 Dynamical properties

As described previously, the structural properties of MHPs profoundly influence their optical characteristics. However, it has been discovered that the dynamics of these materials influence both the structure and optical performance of MHPs.[57–60] Hence, understanding the dynamical properties of MHPs is key to optimizing them for various technological applications.

The dynamical properties of MHPs may be divided into vibrational dynamics of the inorganic perovskite lattice,[61,62] rotational and vibrational dynamics of

[‡]Chirality refers to a fundamental structural property that a chiral structure cannot be completely superimposed on a mirror image of itself through rotation and translation, one of a pair of chiral symmetric structures is called an enantiomer which can be differentiated between R and S. R comes from the Latin *rectus* (right), S comes from the Latin *sinister* (left). When the R and S cations account for 50% each, the circularly polarized luminescence characteristics of the material may disappear, and the material is called racemic (rac).

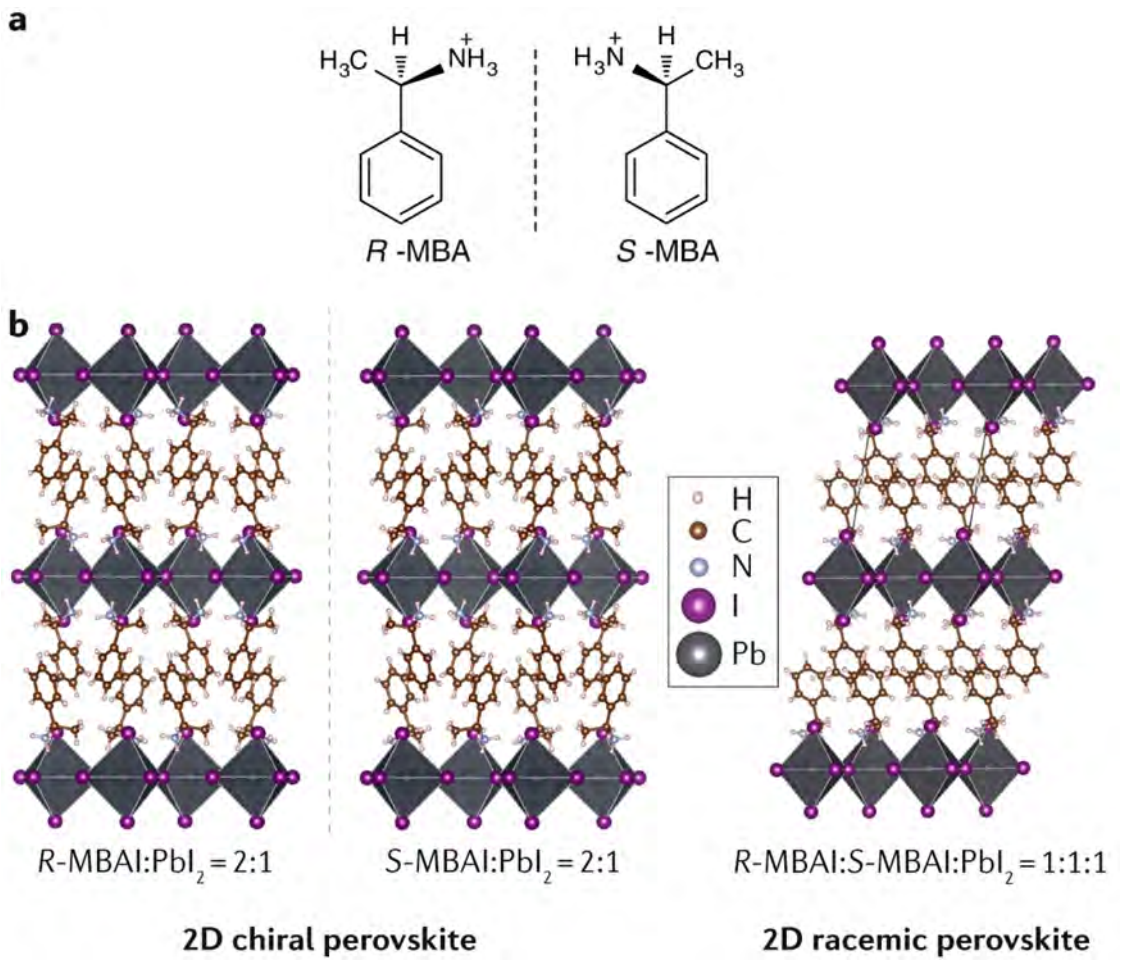

Figure 2.5: Schematic diagrams of **a.** The chiral ligands: MBA (methylbenzylammonium), and **b.** Single-crystal structures of 2D chiral MHPs : (R)-MBA_2PbI_4, (S)-MBA_2PbI_4, and 2D achiral MHP: rac-MBA_2PbI_4 with their different precursors ratio (R-/(S)-MBA)I:PbI_2 for synthesis. The dashed lines can be considered as the "mirror" for enantiomers.[52] Used with permission of © Springer Nature BV, from Long, G., Sabatini, R., Saidaminov, M.I. et al. *Chiral-perovskite optoelectronics.* Nat Rev Mater 5, 423–439 (2020); permission conveyed through Copyright Clearance Center, Inc.

the organic cation,[12,63,64] and possibly, but with lower probability, translational dynamics of ions.[65,66]

Of particular concern in this thesis is the organic cation dynamics, which have been invoked to explain several structural and optoelectronic properties of MHPs, besides being of great fundamental interest. As an example from 1978, structural studies of $MAPbBr_3$ suggested that at room temperature the $PbBr_6$ octahedra remain undistorted due to the dynamics of the MA cations.[67] As another example, the rotation of the MA cation has been suggested to lead to the formation of ferroelectric domains, which in turn control the ferroelectric polarization of MHPs.[13,68] Subsequent research revealed that the reorientation of the organic cations affects the tilting of the perovskite octahedra, which can break and help in the formation of hydrogen bonds between the organic

cation and the octahedra, and this is considered one of the reasons for phase separation in MHPs.[69] Lately, there also have been several studies suggesting that the reorientational dynamics of cations are one of the causes of charge screening, with consequent stabilization of photogenerated charge carriers and prevention of fast charge recombination.[57,70]

Rotational diffusion

In recent years, dynamical properties of organic cations have been investigated through QENS,[12–16,18,20,21,24–30] nuclear magnetic resonance (NMR),[71–73] and infrared (IR) spectroscopy.[74,75] Meanwhile, a lot of computational work by molecular dynamics (MD) simulations has been also performed.[76–78] These experiments and simulations have characterized the timescale, geometry, and activation energy of the dynamics of organic cations in various MHPs, and in some cases explored their correlation with properties such as antiferroelectric or ferroelectric behaviour,[13] crystal structure,[59] stability,[60] and photovoltaic hysteresis.[79] Most studies have focused on $MAPbX_3$ (X = Cl, Br, and I) and $FAPbX_3$ (X = Cl, Br, and I). These results show that the dynamics of the organic cation can be generally explained as localized "jump-diffusion"[§] dynamics over a specific number of sites which depends on the symmetry of the organic cation as well as the symmetry of the surrounding inorganic MHP framework.

Table 2.1 shows a summary of key dynamical properties for $MAPbI_3$ and $FAPbI_3$, as obtained from previous studies. As can be seen, the localized dynamics of MA and FA cations occur on the timescale of picoseconds. For $MAPbI_3$, the dynamics evolve from 3-fold (C_3) jump-diffusion of methyl and ammonium around the C–N axis, in the low-temperature ($T<$ 165 K) orthorhombic phase, to C_3 jump diffusion coupling with 4-fold (C_4) jump diffusion of the C–N axis in the intermediate-temperature (165 K $<T<$ 327 K) tetragonal phase and high-temperature ($T>$ 327 K) cubic phase (Figure 2.6).[12] For $FAPbI_3$, the dynamics evolve from C_4 jump diffusion around the N–N axis in the low-temperature ($T<$ 285 K) tetragonal phase to isotropic reorientational diffusion[31] or tri-axis (N–N axis, C–H axis, and the vertical axis) rotational diffusion[?] in the high-temperature ($T>$ 285 K) cubic phase (Figure 2.6). Besides $MAPbI_3$ and $FAPbI_3$, the organic cations dynamics in the halogen-substituted materials $MAPbBr_3$,[14,15] $MAPbCl_3$,[20,21] and $FAPbBr_3$,[25,27,30] have been also investigated using QENS. The results of these studies show that the MA and FA cation dynamics are affected by the type of X-site halide, but the main types of jump-diffusion mechanisms persist. Furthermore, mixed-cation systems, such as $FA_xMA_{1-x}PbI_3$,[26,27] and $MAPbI_{2.94}Cl_{0.06}$,[20] have been investigated. In general, the A-site organic cation dynamics in these MHPs with different X-site ions show similar geometry in the same phase with a variance in the timescale and the activation energy of the dynamics.

Compared to 3D MHPs, fewer QENS studies have focused on investigations

[§]Jump diffusion refers to an atom "jumping" from one site to another. The time for a jump is considered to be negligible. The time between two consecutive jumps is called the residence time.

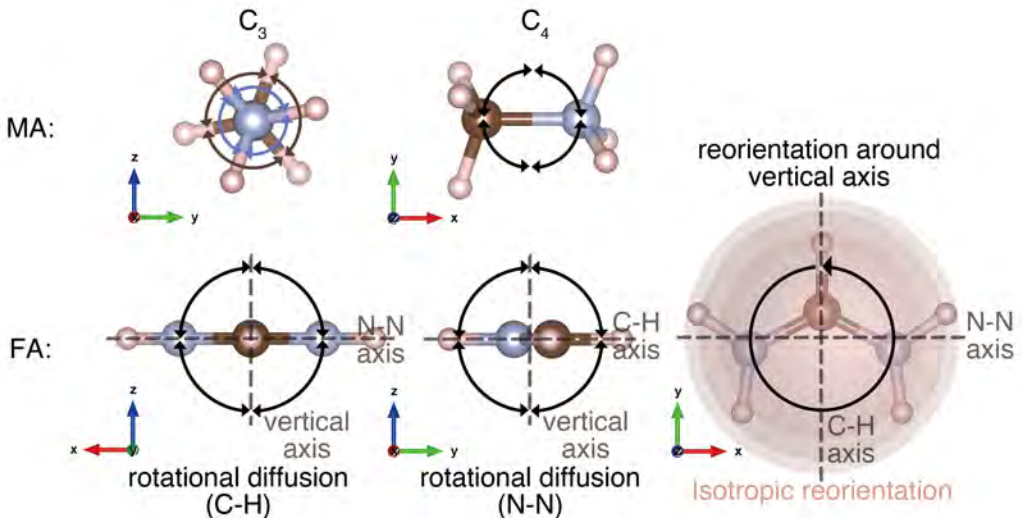

Figure 2.6: Schematic illustration of localized dynamics of MA and FA cations in $A\mathrm{Pb}X_3$ (A = MA, FA; X = Cl, Br, and I).

Table 2.1: Compilation of dynamics data for MA and FA dynamics in $MAPbI_3$ and $FAPbI_3$, respectively.

	Method	C_3 (τ, T)	C_4 (τ, T)	Reference No.
$MAPbI_3$ (tetragonal)	QENS	0.82 ps 300 K	4.70 ps 300 K	12
	NMR (^{2}H, ^{14}N)	0.576 ps 300 K	1.73 ps 300 K	72
	NMR (^{2}H, ^{14}N)	0.15 ps 298 K	1.95 ps 298 K	?
	2D IR		3 ps room temperature	74
	2D IR		3 ps room temperature	75
	Method	rotational diffusion (τ, T)		Reference No.
$FAPbI_3$ (cubic)	QENS	64 - 9.4 ps C_4 N-N axis 140 - 285 K (tetragonal)	1.5 ps Isotropic 350 K	31
	NMR (^{2}H, ^{14}N)		8.7 ps Isotropic 294 K	73
	NMR (^{2}H, ^{14}N)	0.38 ps N-N axis 1.05 ps C-H axis 1.3 ps vertical axis 298 K		?

of the organic cation dynamics in lower dimensional MHPs. These studies are limited to QENS studies of the 2D MHP $(OA)_2PbI_4$ (OA = octylammonium), and A_2PbBr_4 [A = n-butylammonium (nBA), 1,8-diaminooctammonium (ODA), and 4-aminobutyric acid (GABA)]. Figure 2.7 shows that the organic cation octylammonium has 2-fold (C_2) rotation of the head group NH_3–CH_2, C_3 rotation of the terminal -CH_3 and -NH_3 groups, and librations of the -CH_2- group at different temperatures.[22] Figure 2.8 shows that the organic cation nBA and ODA exhibits C_2 rotation of the head group NH_3–CH_2, C_3 rotation of the terminal -CH_3 and -NH_3 groups, and librations of the -CH_2- group. The organic cation GABA only has C_3 rotation of the partial -NH_3 group.[28] It has also been reported that the larger A-site cation dynamics radii could lead to less broadband luminescence by reducing the octahedral out-of-plane tilt angle in layered halide perovskites.[28]

Vibrational dynamics

Because of the strong exciton-phonon coupling in MHPs, probing and comprehending these vibrational modes is essential to understanding the mechanisms of their optoelectronic properties. There have been many reports about the vibrational dynamics of MHPs. On the theoretical side, density functional theory (DFT) and molecular dynamics (MD) simulations have been widely

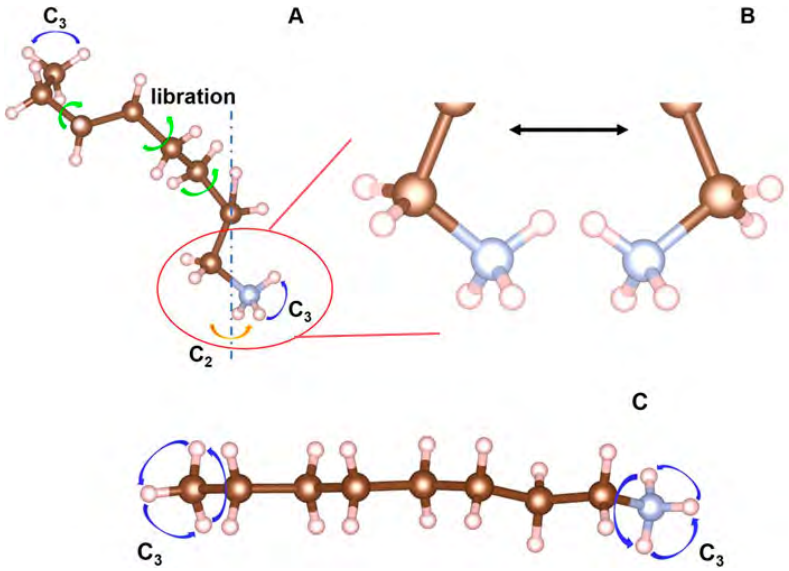

Figure 2.7: Rotational diffusion modes of the OA cation in different phases of $(OA)_2PbI_4$ including (A), (B): high-temperature orthorhombic phase: C_3 of -CH_3, $C_2 \otimes C_3$ of -NH_3, C_2 of the adjacent -CH_2-, and slow librations of other -CH_2- groups. And (C): intermediate and low-temperature monoclinic phases: C_3 of -CH_3 and -NH_3.[22] Used with permission of © American Institute of Physics, from Hu, Xiao; Zhang, Depei et al. *Crystal structures and rotational dynamics of a two-dimensional metal halide perovskite $(OA)_2PbI_4$.* Chem. Phys. 7 January 2020; 152 (1): 014703; permission conveyed through Copyright Clearance Center, Inc.

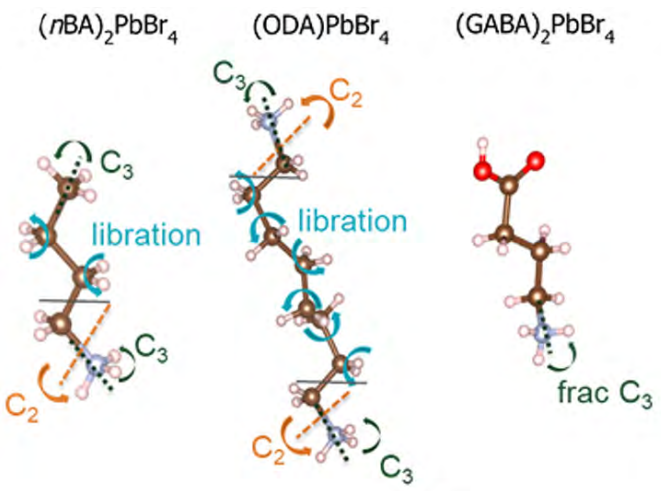

Figure 2.8: Rotational diffusion modes of the cations in A_2PbBr_4 (A = nBA, ODA, and GABA).[28] Copyright © 2022 American Chemical Society, CC BY, from Alexandra A. Koegel, James R. Neilson, et. al.

applied,[76,80,81] while experimental study to phonon dynamics has relied on infrared (IR) spectroscopy,[58,82,83] Raman spectroscopy,[84–86] and inelastic neutron scattering (INS).[16,87–89]

Using the prototypical MHP $MAPbI_3$ as an example, its vibrational modes are commonly classified into internal vibrations of the organic MA cations, internal vibrations of the inorganic framework, and low-frequency cation librations that are intimately coupled to framework motions (Fig 2.9).[81] Owing to the intrinsically soft lattice of MHPs, these vibrational degrees of freedom give rise to rich and unconventional lattice dynamics, including overdamped phonons, significant anharmonicity, and dynamic octahedral tilting.[90,91] Beyond lattice dynamics in equilibrium, increased attention has been paid to the interaction between photogenerated excitations and phonons. In this context, polaron-based descriptions have emerged as a central theoretical framework for capturing charge–lattice coupling in MHPs.[57,92,93] Experimentally, only a small number of studies have employed transient mid-infrared (MIR) spectroscopy to directly track light-induced modifications of the inorganic lattice vibrations.[94–96] Even fewer investigations have addressed how photoexcitation perturbs the orientational and vibrational dynamics of the organic cations, leaving this aspect of nonequilibrium lattice dynamics largely unexplored.[70]

2.3 Metal halide perovskites studied in this thesis

The work in this thesis has focused on studies of different cations in the different dimension of MHPs, including the 3D formamidinium (FA = $HC(NH_2)_2^+$) tin halide perovskite ($FASnX_3$, X = Cl, Br), FA_2SnI_6, and methylammonium (MA, $CH_3NH_3^+$) lead bromide ($MAPbBr_3$). the 2D phenylenediammonium/ xylylenediammonium PDA/XDA, PDA = $C_6H_4(NH_3)_2^{2+}$,XDA = $C_6H_4(CH_2NH_3)_2^{2+}$)) lead bromide perovskite (APbBr$_4$, A = 1,3-PDA; 1,4-PDA; 1,4-XDA), the 0D MHP 1,3-$(XDA)_2PbBr_6$, and the methylbenzylammonium (MBA = $C_6H_5CHCH_3NH_3$)

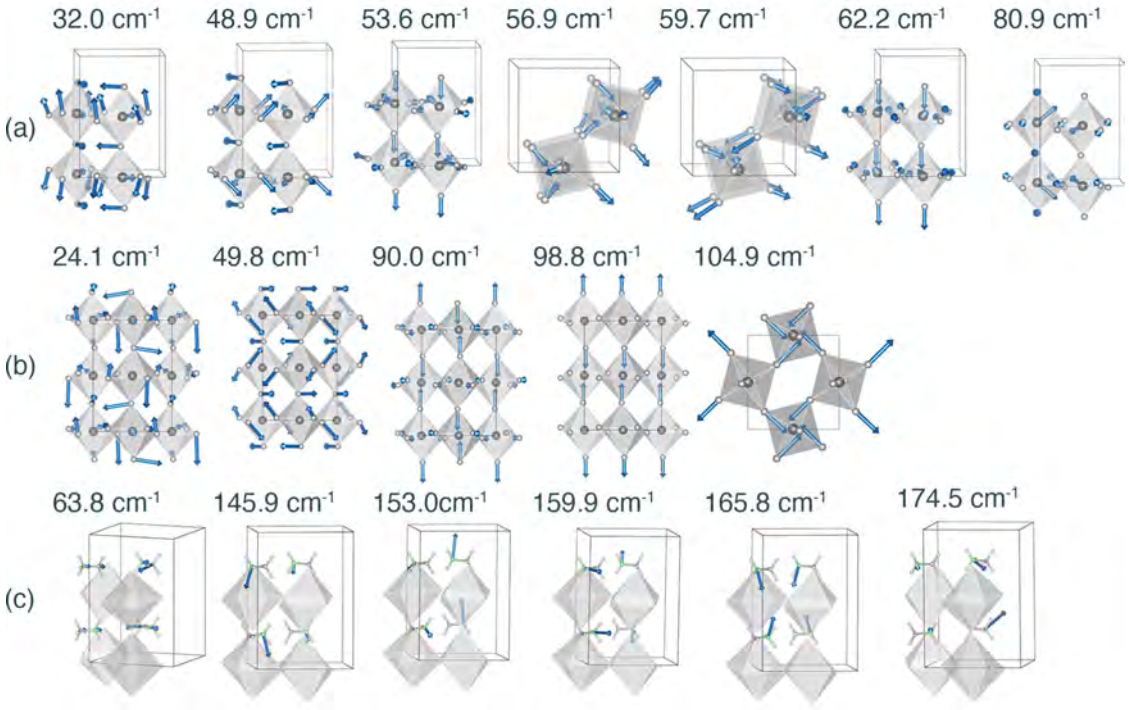

Figure 2.9: Schematic representation of some representative normal modes of vibration of (a) the PbI inorganic framework measured by IR, (b) the PbI inorganic framework measured by Raman, and (c) the librations/translations of the MA cations measured by IR. The PbI octahedra are shaded, the Pb and I atoms are in black and gray color, respectively. Used with permission of © American Chemical Society, from Miguel A. Perez-Osorio; Feliciano Giustino et al. *Vibrational Properties of the Organic–Inorganic Halide Perovskite* $CH_3NH_3PbI_3$ *from Theory and Experiment: Factor Group Analysis, First-Principles Calculations, and Low-Temperature Infrared Spectra.* J. Phys. Chem. C 2015, 119, 46, 25703–25718; permission conveyed through Copyright Clearance Center, Inc.

manganese halide chiral perovskite ($MBAMnCl_3{\cdot}2H_2O$). This study aims to comprehensively analyze and understand the factors that influence the organic cation dynamics within MHPs from the different compositions (different A, B, X-site ions) and structures (geometry of the organic cations and lattice structure).

2.3.1 (R)-/(S)-$MBAMnCl_3{\cdot}2H_2O$

(R)-/(S)-$MBAMnCl_3{\cdot}2H_2O$ represents a novel chiral 0D MHP, that was first reported in 2022 and that exhibits white light emission upon excitation at 330 nm.[97] Structurally, (R)-/(S)-$MBAMnCl_3{\cdot}2H_2O$ exhibits a monoclinic structure of the P_{21} group, with the lattice parameters of a = 6(2) Å, b = 36.409 Å, and c = 6.377 Å.[97] It may be described as a 0D structure where two Mn-Cl octahedra, with two of the Cl^- replaced by H_2O molecules, bridge by two of these H_2O molecules. This is then surrounded by large hydrogen-bonded MBA

cations (Figure 2.10).

These structural results were obtained from single crystal XRD (SC-XRD) on a single crystal sample at 100 K, however, with an non-neglectable, and crystallographically unacceptable large uncertainty in the lattice parameter a = 6(2) Å.[97] For this purpose, I have re-investigated the crystal structure of (R)-/(S)-MBAMnCl$_3$·2H$_2$O, using SC-XRD, with the aim of a more accurate description of the crystal structure. In addition, I have investigated the nature of organic cation dynamics in (R)-/(S)-MBAMnCl$_3$·2H$_2$O by using QENS, with the following main questions being targeted:

- Is it possible to obtain a more accurate description of the crystal structure of MBAMnCl$_3$·2H$_2$O on the basis of SC-XRD measurements?
- Is there any different phase of MBAMnCl$_3$·2H$_2$O? If so, which is the main phase in the sample?
- What is the nature of the localized dynamics of the chiral organic cation (R)-MBA and (S)-MBA in (R)-/(S)-MBAMnCl$_3$·2H$_2$O including its geometry and timescale of the dynamics? How do the dynamics correlate to the investigated temperature and the type of enantiomer?

2.3.2 *A*PbBr$_4$ (*A* = 1,3-PDA; 1,4-PDA; 1,4-XDA) and (1,3-XDA)$_2$PbBr$_6$

The here investigated materials, *i.e.*, *A*PbBr$_4$ (*A* = 1,3-PDA; 1,4-PDA; 1,4-XDA) 2D MHPs and (1,3-XDA)$_2$PbBr$_6$ 0D MHP [Figure 2.11(a)] represent a new series of low-dimensional MHPs with interesting structural and optical properties.[98] Specifically, the shorter cations (1,3-PDA and 1,4-PDA) result in a broad emission centred at around 550 nm, whereas the longer cations (1,3-XDA and 1,4-XDA) result in a narrower emission centred at around 430 nm [Figure 2.11(b)]. In this context, the organic cation dynamics in these different materials have been investigated to reveal if and how the dynamics could have influence to their different luminescence. The following main questions have been targeted:

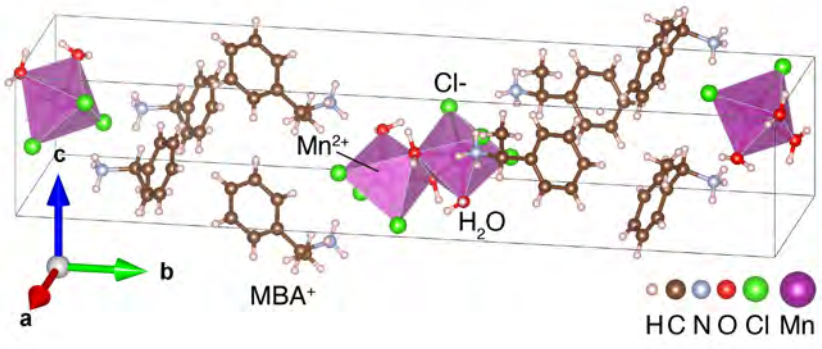

Figure 2.10: Schematic illustration of the MBAMnCl$_3$·2H$_2$O structure, with the unit cell indicated.

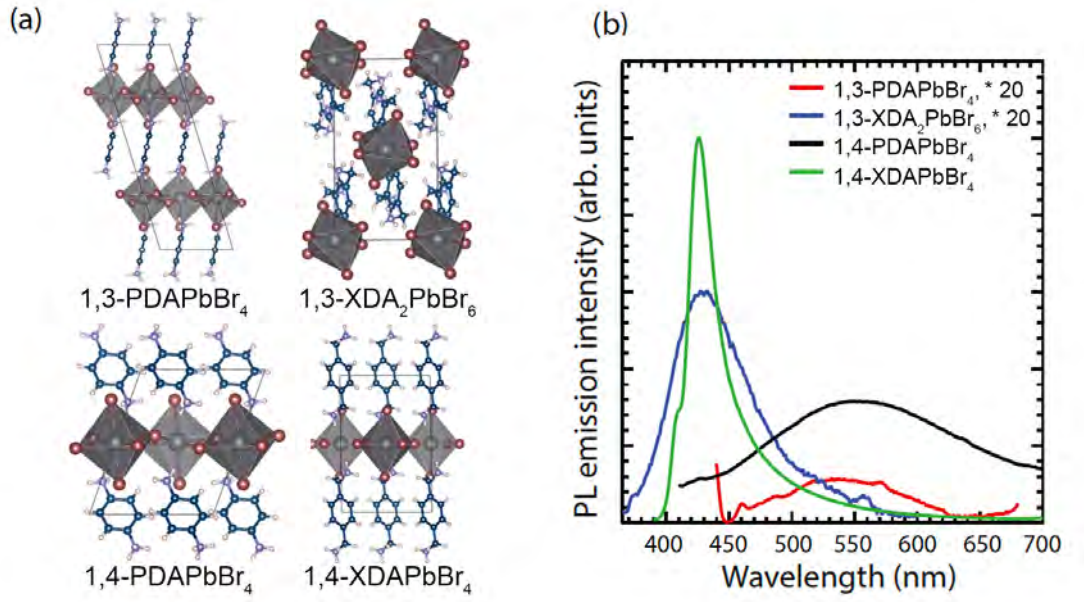

Figure 2.11: (a) Crystal structures of APbBr$_4$ (A = 1,3-PDA; 1,4-PDA; 1,4-XDA) 2D MHPs and (1,3-XDA)$_2$PbBr$_6$ 0D MHP, as determined by single-crystal X-ray diffraction. (b) PL emission spectra of the respective material (the weaker intensity from 1,3-PDAPbBr$_4$ and (1,3-XDA)$_2$PbBr$_6$ have been shown as 20 times stronger in the figure).[98]

- What is the nature of the localized diffusional dynamics of organic cations in APbBr$_4$ (A = 1,3-PDA; 1,4-PDA; 1,4-XDA) and (1,3-XDA)$_2$PbBr$_6$, and how does it depend on temperature?
- What is the relation among the localized distortions of the PbBr$_6$ octahedron, structure of different diammoniums, and the localized diffusional dynamics of organic cations?
- What is the correlation between organic cation dynamics and luminescence?

2.3.3 FASnX_3 (X=Cl, Br) and FA$_2$SnI$_6$

Although Pb-based MHPs such as FAPbI$_3$ and MAPbI$_3$ show promising photoelectric conversion performance, regrettably, Pb is toxic which brings a potential hazard risk to the environment. Therefore, much research is currently focused on the investigation of Pb-free MHPs.[99–102] In this context, Sn-based MHPs are considered to be one of the most attractive substitutions of Pb-based MHPs.[103]¶ With the suitable ionic radius of Sn^{2+} and bandgap for optoelectronic applications, Sn-based MHPs are considered as a new way for lead-free MHPs.[104] Similarly to FAPbI$_3$, FASnI$_3$ undergoes temperature-dependent phase changes. More specifically, FASnI$_3$ exhibits a cubic α phase (space group $Pm\bar{3}m$) at above 275 K, a tetragonal β phase (space group $P4/mbm$) at 150

¶It is worth pointing out that the acidic degradation subproducts and oxidation of the Sn^{2+} are also considered as potential hazard risks.[103]

- 250 K, and an orthorhombic γ phase (space group *Pnma*) at below 125 K (Figure 2.12).[105] As it may have been noticed, there are temperature gaps between different phases because $FASnI_3$ shows a second-order phase transition with mixed phases.[105] FA_2SnI_6 is a vacancy-ordered metal halide double perovskite‖ (Figure 2.13).[106] However, the dynamical properties of these materials, especially regarding the FA cation dynamics, are still unknown. Here, I have focused on the investigations of the following unsolved research questions:

- What is the nature of localized diffusional dynamics of FA in $FASnX_3$ (X

‖Double perovskites refer to a perovskite [$A_2B(II)B'(II)X_6$ or $A_2B(IV)X_6$] with a long-range ordered unit cell whose size is doubling the $AB(II)X_3$ perovskite.

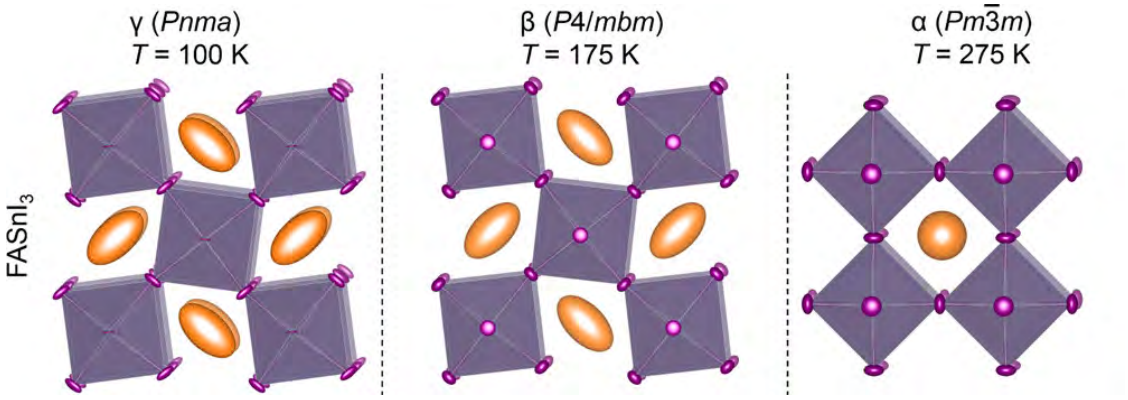

Figure 2.12: Structural evolution of $FASnI_3$ with temperature. Atomic displacement parameters are shown as 50% probability ellipsoids. Colour scheme: orange spheres (FA), purple spheres (I).[105] Copyright © American Chemical Society, CC BY, from Emily C. Schueller, Geneva Laurita, et. al.

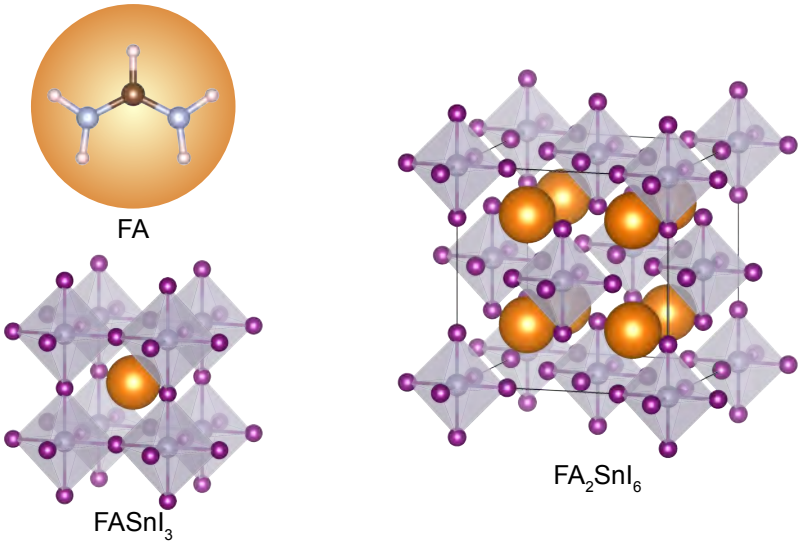

Figure 2.13: Schematic illustration of the inorganic framework of the cubic phase of $FASnI_3$ and FA_2SnI_6. The black lines refer to the unit cell. Colour scheme: orange spheres (FA), brown sphere (C), light blue speheres (N), light pink spheres (H), purple spheres (I), grey spheres (Sn).[105,106]

= Cl, Br) and FA_2SnI_6, such as the geometry, timescale, and activation energy of the dynamics?

- How do the localized dynamics of FA cations change with temperature in $FASnX_3$ (X=Cl, Br) and FA_2SnI_6?
- How does the FA cation dynamics compare with the FA cation dynamics in prototypical $FAPbX_3$ (X=Cl, Br, I)?

2.3.4 $MAPbBr_3$

$MAPbBr_3$ is a prototypical 3D MHP that has been extensively studied for solar cell and LED applications due to its exceptional power conversion efficiency. It exhibits a cubic phase ($Pm\bar{3}m$) at room temperature, transitioning to a tetragonal phase ($I4/mcm$) below approximately 240 K and an orthorhombic phase ($Pnma$) below approximately 150 K (Figure 2.14). Its absorption and emission peaks are located at approximately 525 nm and 540 nm, respectively. However, the mechanisms underlying its superior optoelectronic performance remain a subject of debate, particularly regarding the influence and specific role of the organic cations.

In this context, the vibrational dynamics of $MAPbBr_3$ have been investigated through INS under *in-situ* illumination conditions. Here, I have focused on the investigations of the following unsolved research questions:

- What is the nature of vibrational dynamics of $MAPbBr_3$?
- What is the nature of vibrational dynamics of optical-excited-state $MAPbBr_3$?
- How does the exciton affect the vibrational dynamics of $MAPbBr_3$?

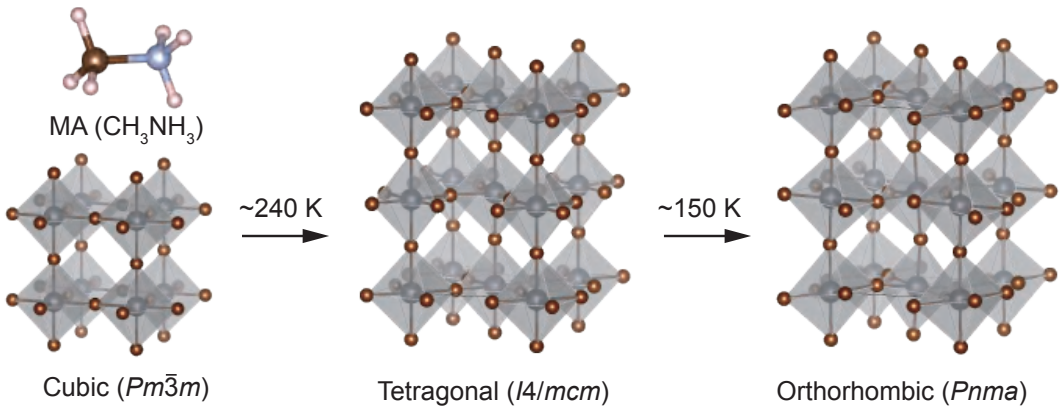

Figure 2.14: Schematic illustration of the MA cation and inorganic framework of $MAPbBr_3$ in different phases. Colour scheme of inorganic framework: Brown spheres (I), grey spheres (Pb).[107,108]

Chapter 3

Methodology of Neutron scattering

This chapter begins with a short historical account of the discovery and basic properties of the neutron and then gives the theoretical background needed to understand the key characteristics of the main experimental techniques used in this thesis, *i.e.* QENS and INS.

3.1 The basic properties of neutron

The concept of the neutron was built by Ernest Rutherford in 1920, named by William Harkins in 1921, and the evidence of its existence was found by James Chadwick in 1931 and published in 1932.[109–111] The neutron is a subatomic particle, whose mass is close to the proton and much larger than the electron.[112] Compared to the proton, a neutron is composed of one up quark, two down quarks, and gluons, which leads to its electrical neutrality. Still, the distribution of quarks with spin angular momentum $\pm 1/2\ \hbar$ makes the neutron possess a weak magnetic moment.[113] It has a relatively long mean lifetime ($\tilde{8}85.7$ s) compared to most other unstable subatomic particles.[114] With electrical neutrality, weak magnetic moment, and a relatively long lifetime neutron scattering techniques can be used to investigate the structure, dynamics, and magnetism of a material. The probed length and energy scales are closely related to the wavelength and energy of the neutron (Table 3.1). In this thesis, cold neutrons (0.05 meV $<E<$ 14 meV) have been used.

3.2 Scattering theory*

Figure 3.1 shows the general geometry of a neutron scattering process, in which an incident neutron with wavevector $\boldsymbol{k}_\mathrm{i}$ and kinetic energy E_i is scattered on a sample. The neutron is scattered to a solid angle $\mathrm{d}\Omega$ with scattering angle θ and azimuthal angle Φ, and the wavevector and kinetic energy of the scattered neutron are $\boldsymbol{k}_\mathrm{f}$ and E_f.

*Magnetic neutron scattering is out of the scope for the thesis, hence the description of the scattering theory is focused on nuclear neutron scattering.

Table 3.1: Classification of neutrons according to their energy and wavelength .

Classification	**Energy**	**Wavelength**
Ultra cold neutron	$\leq$ 0.05 meV	40 Å $\leq$
Cold neutron	0.05 meV - 14 meV	2.4 - 40 Å
Thermal neutron	14 meV - 200 meV	0.6 - 2.4 Å
Hot neutron	200 meV - 1 eV	0.3 - 0.6 Å
Epithermal neutron	1 eV $\leq$	$\leq$ 0.3 Å

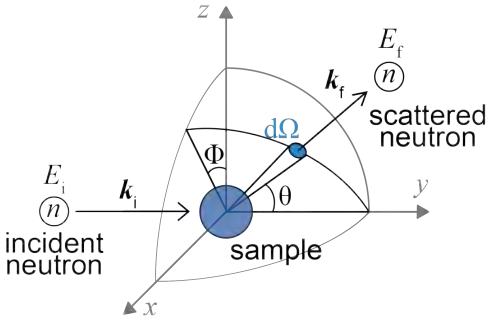

Figure 3.1: Schematic illustration of the scattering geometry. The incident neutrons with wavevector $\boldsymbol{k}_\mathrm{i}$ and kinetic energy E_i scatter on the sample with the scattering angle θ and azimuthal angle ϕ. The neutrons with wavevector $\boldsymbol{k}_\mathrm{f}$ and kinetic energy E_f are scattered into the solid angle element $\mathrm{d}\Omega$.

One of the most crucial aspects of a material subjected to neutron scattering is its ability to scatter, transmit, and absorb neutrons. Except for the absorption, these abilities may be described by the neutron scattering cross-section σ which describes the ratio of scattered neutron rate to the incident neutron flux Ψ [115]:

$$\sigma = \frac{n_{\mathrm{scattered/sec.}}}{\Psi} \tag{3.1}$$

$$\frac{d\sigma}{d\Omega} = \frac{1}{\Psi}\frac{n_{\mathrm{d}\Omega/\mathrm{sec.}}}{d\Omega} \tag{3.2}$$

The magnitude of the scattering strength depends on the nuclei, which varies with the isotope and can be described by its scattering length b (more detailed definition and derivation can be found in Appendix B.1):

$$\frac{d\sigma}{d\Omega} = b^2 \tag{3.3}$$

During the scattering, the exchange of momentum is defined as:

$$p = \hbar(\boldsymbol{k}_i - \boldsymbol{k}_f) = \hbar\mathbf{Q} \tag{3.4}$$

where $\mathbf{Q}$ is the change of neutron wavevector, and the exchange of energy:

$$E = E_\mathrm{i} - E_\mathrm{f} = \hbar\omega \tag{3.5}$$

where ω represents the change in the neutron wave's angular frequency.

Due to the consideration of energy variation, energy dependence needs to be accounted for in the scattering equations. This is done in the double differential cross section which is proportional to the number of neutrons scattered per time unit into a small solid angle with final energy from E_f to $E_f + dE_f$:

$$\frac{d^2\sigma}{d\Omega dE_f} = \frac{1}{\Psi} \frac{n_{\mathrm{d}\Omega/\mathrm{sec.}} \in [E_f; E_f + dE_f]}{d\Omega dE_f} \tag{3.6}$$

The structure factor $S(\mathbf{Q}, E)$, as a more experimental index that focuses on the $\mathbf{Q}$ and E from the sample but not the incident or scattered neutron can be adapted from the double differential cross-section:

$$\frac{d^2\sigma}{d\Omega dE_f} = \frac{\sigma}{4\pi} \frac{k_f}{k_i} S(\mathbf{Q}, E) \tag{3.7}$$

By taking the Fourier transform of $S(\mathbf{Q}, E)$ one can obtain the time-related intermediate function $I(\mathbf{Q}, t)$, and the Van Hove correlation function $G(\mathbf{R}, t)$, respectively. The space-time correlation function $G(\mathbf{R}, t)$ describes the probability of finding a particle at position $\mathbf{R}$ at time t.

$$S(\mathbf{Q}, E) \overset{FT}{\rightleftharpoons} I(\mathbf{Q}, t) \overset{FT}{\rightleftharpoons} G(\mathbf{R}, t) \tag{3.8}$$

Therefore, the relation between the neutron scattering process and the space-time information of atoms in the material can be found, and the dynamical properties of the atoms can be further analyzed. For a more detailed definition and derivation of the double differential cross section and correlation functions, the reader is referred to Appendix B.2.

3.3 Coherent and incoherent scattering

Nuclear neutron scattering involves both coherent and incoherent parts. Coherent scattering involves correlations between the position of a nucleus j at the initial time and the position of the other nucleus j' at a later time. Therefore, it describes the interference effect of waves produced by neutrons interacting with all the nuclei in the sample. It provides information about the collective motions and correlations among different nuclei, such as phonons or structural arrangements in a material. Incoherent scattering, on the other hand, involves correlations between the position of the same nucleus j at an initial time and its position at a later time t. In incoherent scattering, the scattered waves from different nuclei do not interfere with each other. In dynamics studies, incoherent scattering reflects the motion of individual atoms or molecules rather than collective motions. The strength of the coherent and incoherent scattering depends on the coherent and incoherent cross-section of the isotopes in the sample. As shown in Figure 3.2, ^{1}H has a very large total scattering cross-section (mainly contributed by the incoherent cross-section) which shows that neutron scattering is often a very powerful technique for the study of single-particle self-dynamics of hydrogen in many materials. The detailed derivation of the coherent and incoherent cross section can be found in Appendix B.2.

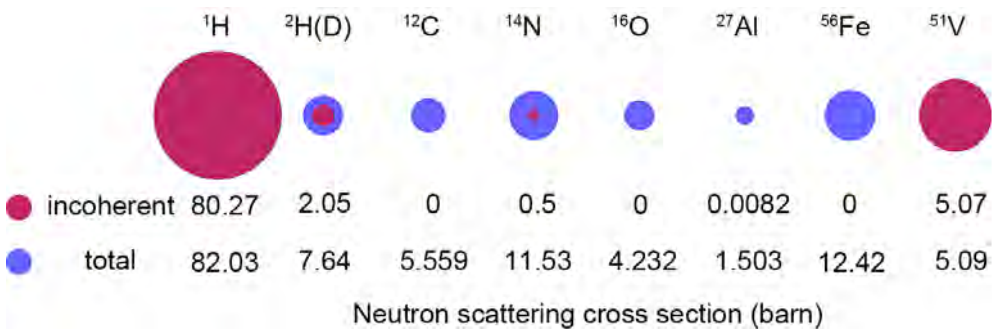

Figure 3.2: Schematic illustration and data of the incoherent and total cross section for different nuclei (1 barn = $1 \cdot 10^{-28}$ m^2).

3.4 Quasielastic neutron scattering

Figure 3.3 shows a general neutron scattering spectrum, plotted as scattering intensity versus energy transfer. The spectrum may be divided into three parts: elastic scattering, quasielastic scattering, and inelastic scattering. Elastic scattering refers to scattering with no energy transfer between the neutron and the nuclei. Quasielastic neutron scattering refers to scattering with a slight energy transfer between the neutron and the nuclei. It is characterized by a broadening of the elastic peak usually coming from atomic diffusion.

While quasielastic and inelastic scattering can be coherent in nature, this thesis focuses on studies of hydrogen dynamics in material. Since hydrogen scatters mainly incoherently (see Figure 3.2), the quasielastic signal can be approximately treated as incoherent [$S(\mathbf{Q}, E) \approx S_{\mathrm{inc}}(\mathbf{Q}, E)$, $I(\mathbf{Q},t) \approx I_{\mathrm{inc}}(\mathbf{Q},t)$]. The correlation function $G(\mathbf{R},t)$ for the incoherent scattering can be used to describe the probability of an atom itself can be found at position $\mathbf{R}$ marked as $G_{\mathrm{s}}(\mathbf{R},t)$. The links among these three correlation functions through the reversible Fourier transform are the key to investigating the atomic self-

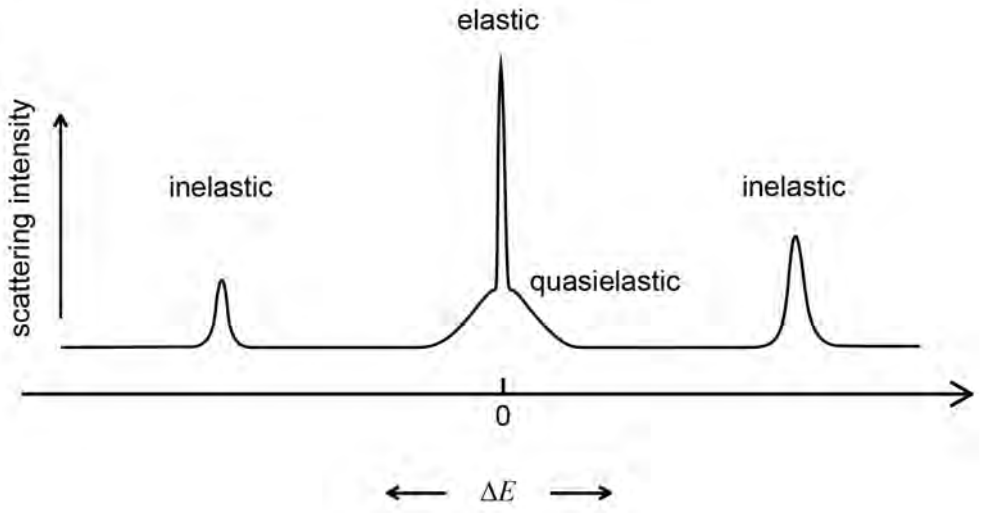

Figure 3.3: Schematic of elastic, quasielastic, and inelastic scattering peaks in $S(E)$.

diffusional dynamics through quasielastic neutron scattering:

$$S_{\mathrm{inc}}(\mathbf{Q}, E) \overset{FT}{\rightleftharpoons} I_{\mathrm{inc}}(\mathbf{Q}, t) \overset{FT}{\rightleftharpoons} G_{\mathrm{s}}(\mathbf{R}, t) \tag{3.9}$$

Analysis of QENS data

In the analysis of QENS data, the neutron scattering spectrum is normally approximated with a function of the form:

$$S_{\mathrm{inc}}(Q, E) \propto A_{i=0}(Q)\delta(E) + \sum_{i\neq 0} A_i(Q)\mathcal{L}_i(Q, E) \tag{3.10}$$

Here, the first term $A_{i=0}(Q)\delta(E)$ describes the elastic scattering. The second term is a series of Lorentzian functions $\mathcal{L}(Q, E)$:

$$\mathcal{L}(Q, E) = \frac{1}{\pi}\frac{\gamma(Q)}{E^2 + [\gamma(Q)]^2} \tag{3.11}$$

with half-width-at-half-maximum (HWHM) γ, which describes the quasielastic scattering. The $0 \leq A_i(Q) \leq 1$ are the normalized Q dependent amplitude of structure factors ($\sum_i A_i(Q) = 1$). The γ has a reciprocal relation to the correlation time τ ($\gamma = \hbar/\tau$), and $\gamma/\hbar$ can describe the diffusion rate of the diffusing atom from one position to the other correlated positions.

The QENS can arise from long-range translational diffusion and/or localized diffusion of atoms. Long-range translational diffusion, which refers to the probability of the mobile species returning to the initial position approaches zero after a relatively long time [$G_s(\mathbf{R}(t = 0), t \to +\infty) = 0$], is commonly observed in liquid samples and ionic conductors. For long-range diffusion, the correlation time $\tau(Q)$ follows Brownian translational diffusion and the incoherent scattering function can be found at a limited Q-value which can be described by Einstein's random walk theory [115]:

$$S_{\mathrm{inc}}(Q, \hbar\omega) = \frac{1}{\pi}\frac{DQ^2}{\omega^2 + (DQ^2)^2} \tag{3.12}$$

$$\tag{3.13}$$

where D is the diffusion coefficient, and $\tau(Q)^{-1} = DQ^2$ when $\gamma(Q) = \hbar/\tau(Q) = \hbar DQ^2$.

Localized diffusion refers to the probability of the mobile species to return to the initial position approaches a constant c ($0 < \mathrm{c} < 1$) after a relatively long time [$G_s(\mathbf{R}(t = 0), t \to +\infty) = \mathrm{c}$]. For localized diffusion, two important conclusions can be found:
1. The HWHM $\gamma(Q)$ of Lorentzian is Q independent, which can be understood by the probability, that the nuclei can be found at position R at a long enough time, is independent of the initial position;
2. The amplitude A_0 does not equal 0 at Q→0 of the localized diffusion, unlike the long diffusion which can be obtained from the Fourier transform: $G_s(\mathbf{R}, t \to +\infty) = 0 \overset{FT}{\Rightarrow} I_{\mathrm{inc}}(\mathbf{R}, t \to +\infty) = 0 \overset{FT}{\Rightarrow} A_0 = 0$.

These statements can thus help to distinguish whether the dynamics observed in an experiment are of long-range or localized character. For the localized diffusion, the correlation time (τ) from the dynamics giving rise to QENS can be derived from:

$$\tau = \hbar/\gamma \tag{3.14}$$

In a limited temperature range ($T_0 \leq T \leq T_1$) with a relatively ideally tiny change of the external influence (*e.g.* the same crystal phase), the molecular dynamical activation energy E_a often can be found by following the Arrhenius equation through the fitting of temperature-dependent τ results:

$$\tau(T) = \tau(T_0) \cdot e^{-E_a/[k_{\mathrm{B}}(T)]} \tag{3.15}$$

where k_{B} is the Boltzmann constant.

As described before, the localized diffusion will bring a fixed probability that a self-diffusing nucleus can be found within a bounded space, $[G_s(\mathbf{R}_{t=0}, t \rightarrow +\infty) \rightarrow c]$, where the relative intensity of this elastic component is known as the elastic incoherent structure factor (EISF=A_0) (the derivation process can be obtained in Appendix B.4). EISF can be experimentally calculated by the ratio of the area of the elastic peak to the area of the elastic peak plus quasielastic peak(s) *i.e.*:

$$\mathrm{EISF} = \frac{\mathrm{Area}_{\mathrm{elastic}}}{\mathrm{Area}_{\mathrm{elastic}} + \mathrm{Area}_{\mathrm{quasielastic}}} \tag{3.16}$$

The EISF contains information about the geometry of localized dynamics. As shown in Figure 3.4, it decays from 1 at $Q = 0$, and varies by the spatial information of the atom including the number of residence positions N and the distances d among the positions ($d = |\mathbf{R}_{\mathrm{i}} - \mathbf{R}_{\mathrm{j}}|$). For the simple equivalent site jump-diffusion cases (equal mean residence time and jump distance), the EISF is approaching the reciprocal of the number of residence positions at larger Q, and the Q position of the lowest value of EISF is proportional to the reciprocal of the jump distance. The information about geometry contained by EISF needs to be extracted by a suitable diffusion model which can fit the EISF and also follows the laws of physics and chemistry.

Figure 3.5 shows several commonly used diffusion models, including the 2-site jump-diffusion model which considers the particle jump between 2 sites. Its mean residence times are τ_1 and τ_2 and jump distance is $d = |\mathbf{R}_1 - \mathbf{R}_2|$ [Figure 3.5(a)].[115] And the N-fold jump-diffusion model which is supposed that the particle can only directly jump to the nearest 2 sites on the circle, for instance in Figure 3.5(b), when the particle is on the site $\mathbf{R}_i$ the next jump of it can only jump to $\mathbf{R}_{i-1}$ or $\mathbf{R}_{i+1}$. In other words, $\tau_{i,j}^{-1} = 0$ when $|i - j|>1$. The isotropic reorientation model is similar to the underlying logic of the previous model, where an equivalent site model is also considered, but considering the spatial angle instead of the plane angle [Figure 3.5(c)].

3.5 Inelastic neutron scattering

Inelastic scattering is identified by an energy transfer between the neutron and nucleus and, distinguished from QENS, which appears as peaks at $\Delta E \neq 0$

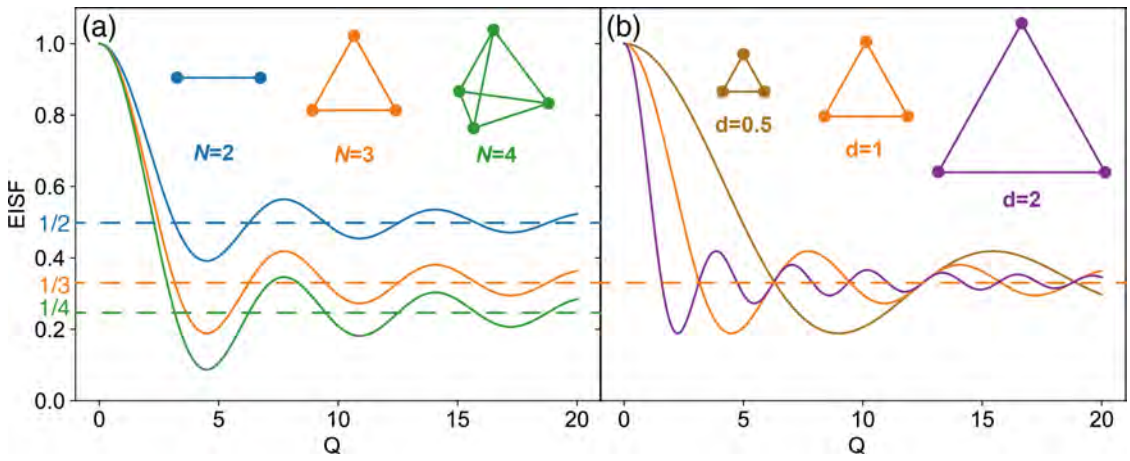

Figure 3.4: EISF for the jump diffusion over equivalent sites with (a) $d = 1$ and for different N values, and (b) $N = 3$ with different d values.

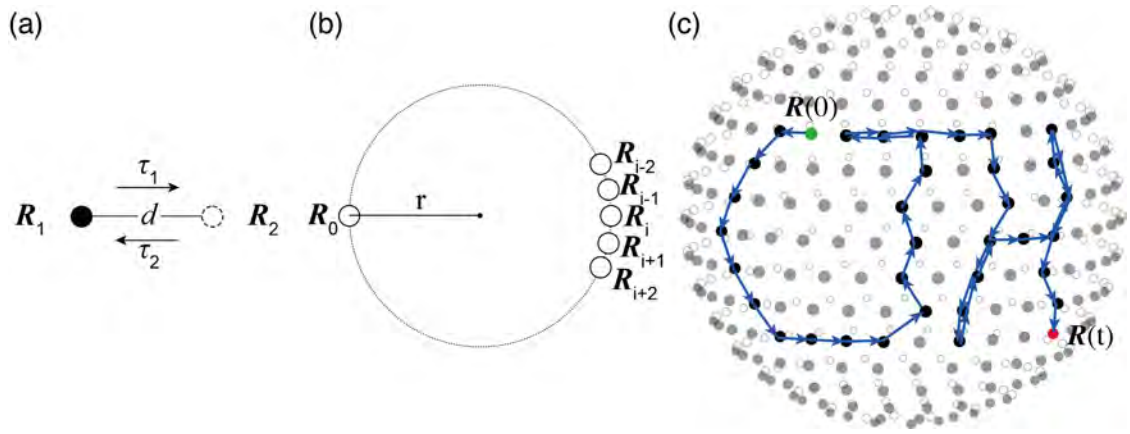

Figure 3.5: Diffusion models of (a) 2-site jump-diffusion, (b) N-fold jump diffusion on a circle, and (c) diffusion on a sphere (commonly found from the isotropic reorientation). The hollow and solid circles represent a large enough amount of evenly distributed positions on the sphere, where the hollow circles represent the positions of the back of the sphere from this perspective, the blue arrows represent one of the random diffusion routes from the position at beginning $R(0)$ (green circle) to the position $R(t)$ (red circle) at time t.

(Figure 3.3). INS peaks arise from the energy and momentum exchange between the incident neutron and nucleus. They can, for examples, originate from quantum tunneling and atomic vibrations at millielectronvolt scale.

Vibrational dynamics in molecular crystals are systematically classified based on their characteristic eigenvectors and energy ranges.† Internal modes, also known as intramolecular vibrations, correspond to high-frequency optical branches. In contrast, external modes involve the displacement of the molecule as a rigid unit within the lattice. These external dynamics are further divided into librations, which are rotational oscillations corresponding to external optical phonons; and translations, which manifest as acoustic branches when

†The discussions regarding the INS spectra in this thesis pertain to vibrational dynamics.

molecules move in-phase, or as optical branches during antiphase motions (Figure 3.6).[116]

As introduced in section 3.3, INS is also contributed by coherent and incoherent scattering, which yield fundamentally different insights into lattice dynamics. Coherent inelastic scattering arises from the collective interference of neutrons scattered by different nuclei, thereby preserving information regarding both the wavevector ($\mathbf{k}$) and frequency (ω) of phonons. This allows for the experimental determination of phonon dispersion relations, $\omega(\mathbf{k})$, across the Brillouin zone. Incoherent inelastic scattering is a self-correlation process that reflects the dynamics of individual nuclei over time, independent of their spatial relative positions.[‡] It provides information only on the frequency of vibrations, manifesting as the density of vibrational states [DOS or $g(\omega)$]. In this thesis, the measured INS intensity is overwhelmingly dominated by scattering on the ^{1}H isotope, which possesses an incoherent cross-section ($\sigma_{inc} \approx 80.3$ barns, Figure 3.2). Therefore, the INS spectra obtained for $MAPbBr_3$ (where MA = CH_3NH_3) intrinsically contain the information of the DOS which is mainly contributed by hydrogen (Figure 3.7).

In a simple situation, assuming single scattering and accounting for the powder average of an isotropic system, the scattering intensity is given by the equation[116]:

$$S(\mathbf{Q},\omega) = Q^2u^2 \exp(-Q^2u^2) \tag{3.17}$$

where u^2 denotes the mean-square displacement of the atom. The pre-exponential term, Q^2u^2, increases as the momentum transfer, or the scattering atom displacement increases. The exponential term, $\exp(-Q^2u^2)$, is called Debye-Waller factor, decreases as the momentum transferred, or the scattering atom dis-

[‡]Within the scope of this thesis, all INS analyses focus on incoherent scattering.

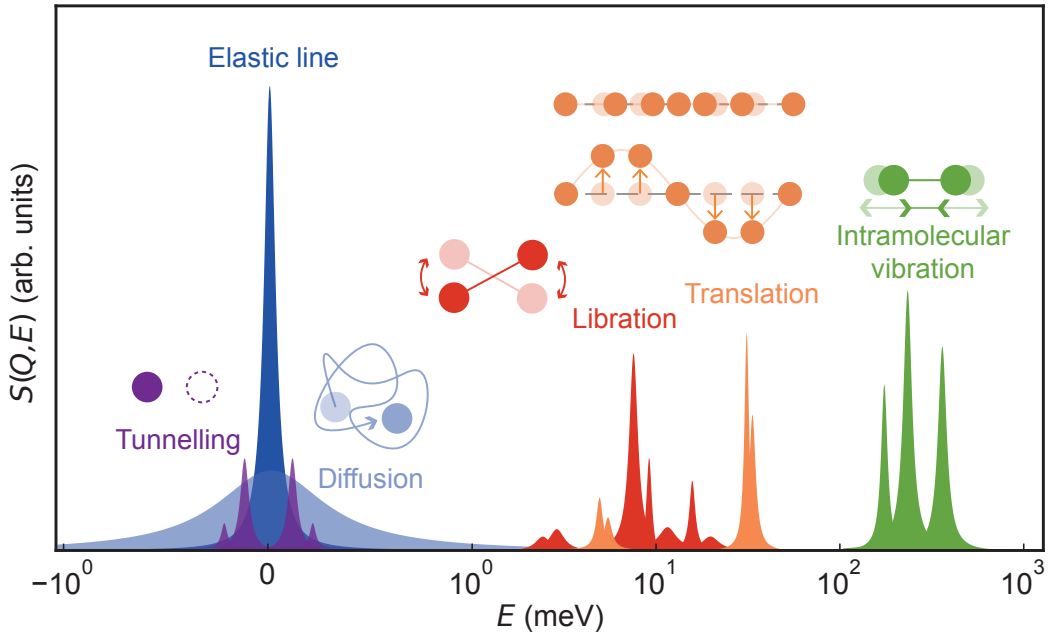

Figure 3.6: The INS map originates from various of molecular dynamical modes.

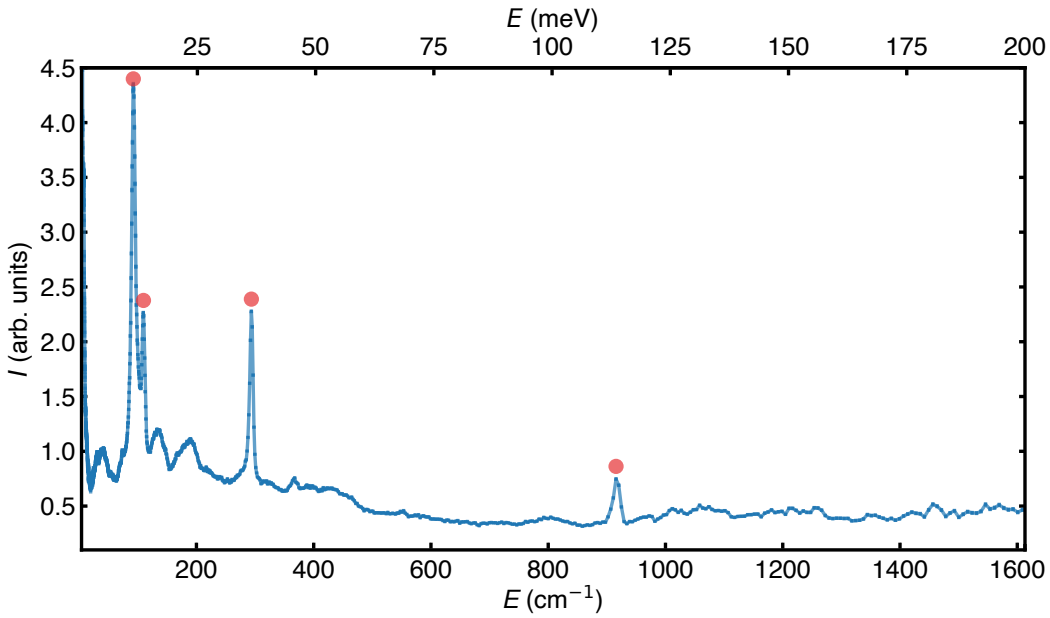

Figure 3.7: INS spectrum of $MAPbBr_3$, as measured at 50.7 K. The distinct peaks, at around 93, 109, and 294 cm^{-1}, are contributed from the MA nodding (65-120 cm^{-1}), C-N torsion (295 cm^{-1}) motions, and MA intramolecular vibration (916 cm^{-1}), marked by red circles.

placement increases. Apparently, the pre-exponential term (Q^2u^2) increase slower than the Debye-Waller factor decreases when it is at a relatively high value, where the INS intensity is proportional to $\exp(-Q^2u^2)$. Physically, the Debye-Waller factor functions as a dynamic thermal parameter that quantifies the time-averaged variance of an atom's deviation from its equilibrium lattice site, which is driven by thermal fluctuations. Consequently, the INS intensity shows temperature dependence. The intensity of the fundamental single-phonon transitions undergoes exponential reduction at elevated temperatures or within the high-Q scattering regime which is dictated by the Debye-Waller factor. The increased thermal population of low-energy external modes also enhances the probability of multiphonon scattering processes. This results in broadening of spectral features which cover the discrete vibrational peaks so called phonon wings. Therefore, samples should be studied at cryogenic temperatures to increase the observed intensities and reduce the effects of phonon wings when Q is fixed at a relatively high value from the instrument.[116]

Chapter 4

Experimental details

This chapter gives a brief introduction to the facilities and instruments used, and to the procedures, analysis and processing of the results of the QENS and INS experiments that have been performed in this thesis.

4.1 Quasielastic neutron scattering

QENS experiments can be performed using several different types of instruments, including the spin-echo spectrometer, backscattering spectrometer, and time-of-flight (ToF) spectrometer. Utilizing different types of instruments enables the investigation of dynamics over a time range between 10^{-7} s to 10^{-13} s and a length scale from 0.1 to 1000 Å.[117]

4.1.1 Time-of-flight spectrometer: FOCUS

In this thesis, direct geometry ToF spectrometer FOCUS, which is located at the Swiss spallation neutron source (SINQ)* at the Paul Scherrer Institute in Switzerland, was used (Figure 4.1).

FOCUS is a time and space focusing ToF spectrometer, which uses both a Fermi-chopper and a monochromator for neutron beam focusing, for cold incident neutrons (Figure 4.2).[119,120] The broad band ("white") neutron beam is reduced in size by means of a vertically converging neutron guide, then chopped by a pre-selector disc chopper, reflected by a focusing monochromator crystal, and further chopped by a Fermi chopper to focus on the sample, making the incident neutron wavelength monochromized with confirmed incident neutron energy to the sample (Figure 4.2). By fixing the distance from the sample to the detector and recording the time-of-flight of the scattered neutrons as they reach the detector, the ToF spectrometer can calculate the speed of the scattered neutrons, thereby determining their energy after scattering. Additionally, using spatially distributed detectors, it can measure the neutron scattering angles, allowing for the calculation of the E and Q transfer.

Due to limitations such as neutron flux, the shape, size, and quantity of the samples are very important. Generally, the geometry of the sample is selected

*SINQ is the first and only continuous spallation neutron source in the world.[118]

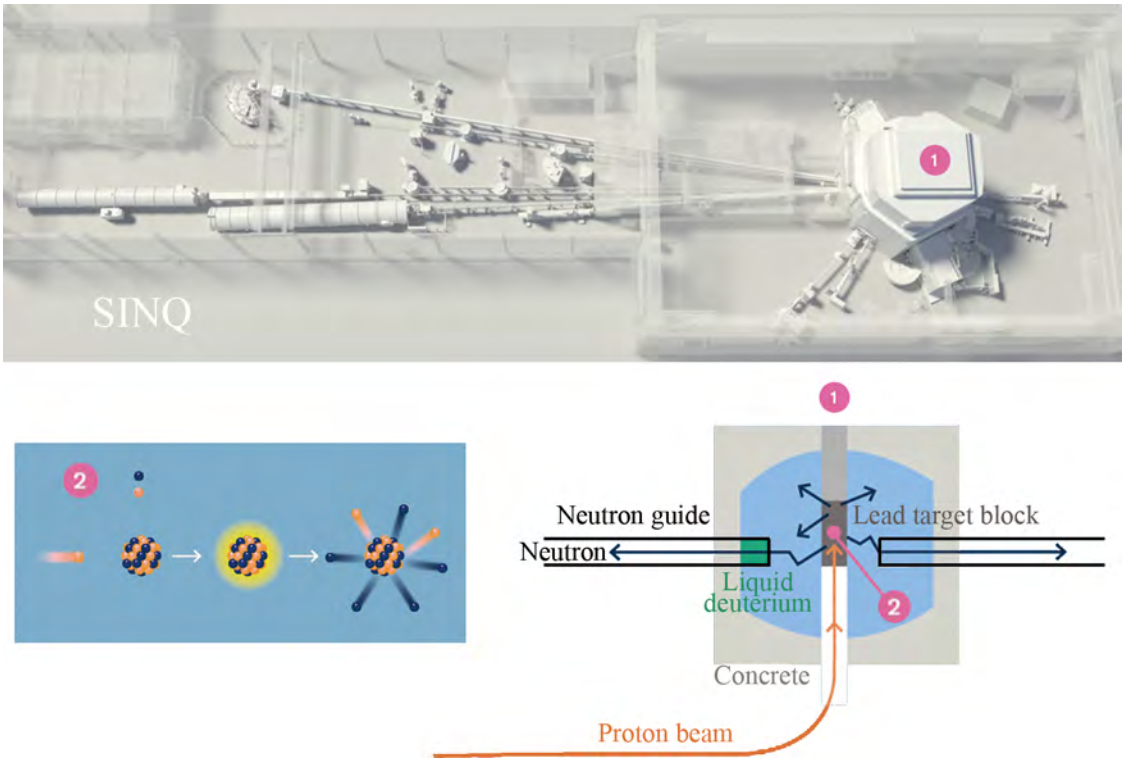

Figure 4.1: Schematic illustration of SINQ (1) shows the neutron source, where the neutrons are transferred to each instrument by neutron guides, and (2) shows the mechanism of producing the neutron through proton beam and lead target. © 2024 PSI (Credit: Paul Scherrer Institute / Mahir Dzambegovic)

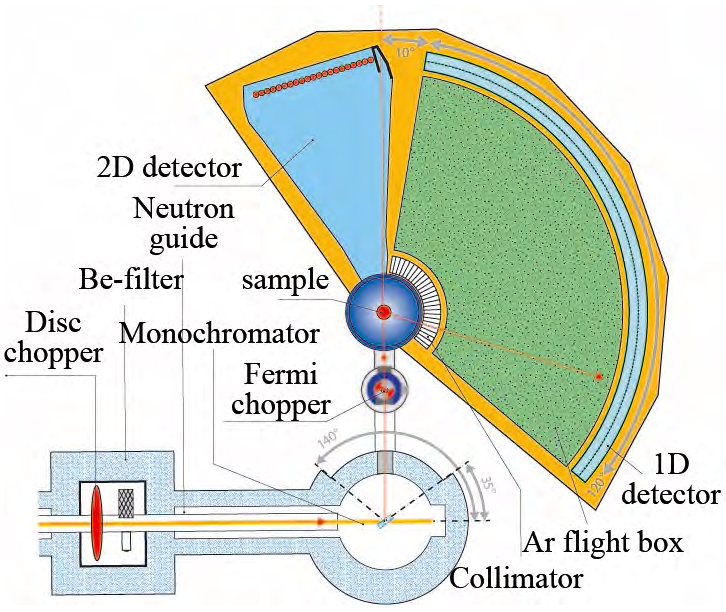

Figure 4.2: Schematic illustration of FOCUS.[121] © 2024 PSI (Credit: Paul Scherrer Institute)

aiming for a scattering probability less than 10%, thereby reducing the impact of multiple scattering and allowing the experiment to be conducted within

a controllable measuring time. A cylindrical aluminium sample cell, which has been chosen for my QENS experiments, is used to allow each neutron to traverse a similar sample thickness during the scattering, whereas a flat cell might cause the neutron to go through more samples with a higher probability of having multiple scattering when it is scattered to the angle parallel to the cell (Figure 4.3).

4.1.2 Near backscattering ToF spectrometer: DNA

To probe the slower organic cation dynamics at low temperatures, the near-backscattering ToF spectrometer: DNA, located at the Japan Proton Accelerator Research Complex (J-PARC), was employed to investigate the sub-nanosecond timescale dynamics. As illustrated in Figure 4.4(a), the DNA spectrometer is equipped with a pulse-shaping chopper and silicon crystal analyzers. These silicon crystal analyzers are housed within a vacuum vessel [Figure 4.4(b)]. The scattered neutrons are recorded by ^{3}He position-sensitive gas detectors (PSD). These detectors are arranged with upward and downward offsets along a circumference centered on the scattering position, operating in a near-backscattering geometry with a Bragg angle of $\theta \approx 87.5°$.[122]

As illustrated in Figure 4.5, the energy resolution and the accessible energy transfer (E) range of the spectrometer can be tuned by adjusting the rotational frequency and the slit size of the pulse-shaping chopper. The accessible momentum transfer (Q) range is modified by selecting different Silicon analyzer reflections (specifically, the (111) or (311) crystal planes). When the pulse-shaping chopper is operated at 225 Hz with a 10 mm slit size, a high energy resolution of 2.4 μeV is achieved, covering an E range from -40 to +100 μeV. When the chopper is in a fully open position (0 Hz), the energy resolution relaxes to 14 μeV, which substantially extends the measurable E range from -500 to +1500 μeV. Regarding the scattering vector, selecting the Si(111) reflection provides access to a Q range of 0.08 to 1.98 Å^{-1}, whereas switching to the Si(311) reflection shifts the corresponding Q window to higher values, spanning from 1.79 to 3.39 Å^{-1}.[123] The best energy resolution can

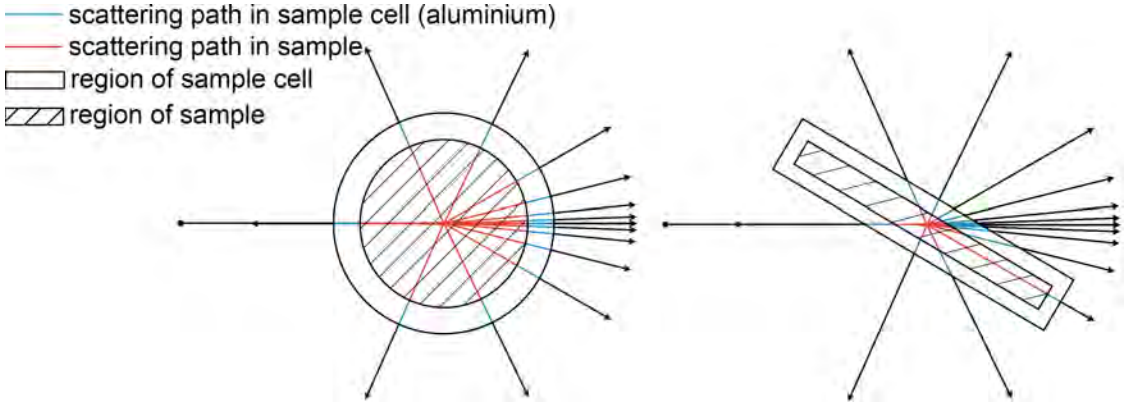

Figure 4.3: Schematic diagram of the sections of the cylindrical sample cell (left), flat sample cell (right), and the potential neutron scattering paths.

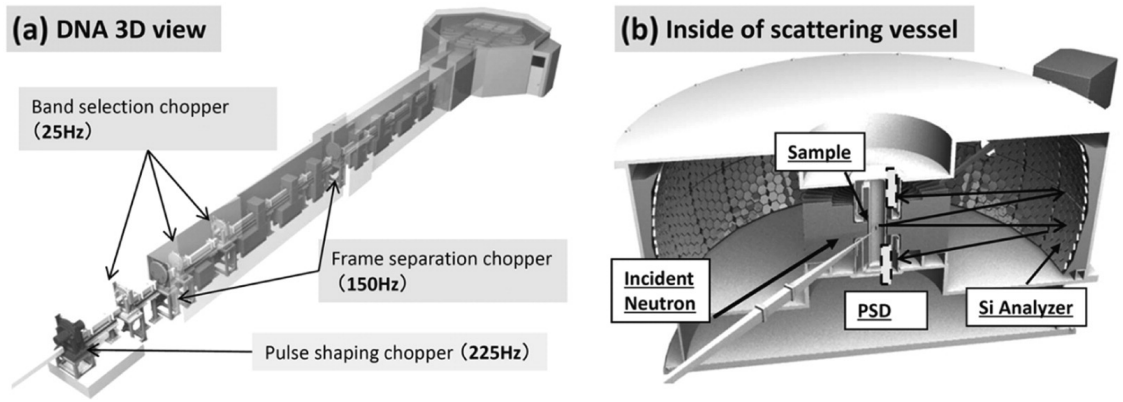

Figure 4.4: (a) Schematic view of DNA spectrometer. The pulse shaping chopper and six disk choppers of three types are installed on the neutron super mirror guide beamline.(b) At the end of neutron guide, the incident neutron beam was focused on the sample position. The scattered neutron at sample was selected by Bragg reflection of Si analyzer, and detected by ^{3}He gas detectors (PSD).[122] Copyright © Elsevier B.V, CC BY-NC-ND 4.0, from Hideki Seto, et. al.

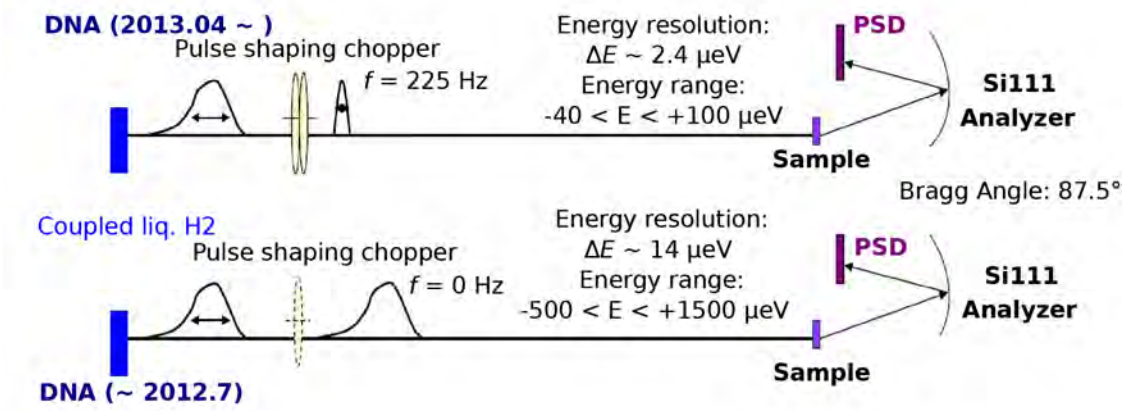

Figure 4.5: Principle of DNA spectrometer optics and two measurement conditions.[123] Copyright © hysical Society of Japan, CC BY 4.0, from Kaoru Shibata, et. al.

achieve 1.4 μeV, with using restricted 1 cm sample height and the setting of pulse-shaping chopper is 10 mm $\times$ 10 mm slit and 300 Hz.[124]

4.1.3 QENS data processing

The main goal of the QENS data processing is to obtain the dynamical structure factor $S(Q, E)$. This is obtained by a series of data reductions, calibrations, and corrections applied to the raw ToF data $N(2\theta, t)$ where the θ is the scattering angle and t is the neutron flying time. The main steps are described in the

following and shown in Figure 4.6. Firstly, the measurement of an empty cell is subtracted from the raw data. Secondly, the data is normalized to the monitor counts. Thirdly, the efficiency of the detectors is corrected by a measurement and subsequent normalization to a vanadium standard, which is an almost pure incoherent and elastic scatterer. Fourthly, the ToF raw data $N(2\theta,\ t)$ is transferred from time (t) to the energy (E) domain. Finally, the data is convoluted from the scattering angle (θ) to Q, thereby obtaining the structure factor $S(Q,E)$. Because the nature of scattering data is asymmetric, which can be briefly understood from the fact that a system at its ground state cannot find the energy to transfer to the neutrons, sometimes the process of detailed balance is necessary for this step to make the $S(Q,E)$ symmetrized to allow fitting with symmetric Lorentzian functions (see Appendix B.5).

Once the structure factor has been obtained, the evidence of the existence or non-existence of QENS can be found by comparison to the resolution function $R(Q,E)$. $R(Q,E)$ can be usually obtained by a measurement at a very low temperature (*e.g.* $T = 10$ K), where the scattering can be normally approximated as elastic. If a QENS signal is found, it can be usually analyzed by fitting to a sum of Lorentzians (see also section 3.4). The fitted $S(Q,E)$ needs to be convoluted with the $R(Q,E)$:

$$S(Q,E) \rightarrow [A_{i=0}(Q)\delta(E) + \sum_{i\neq 0} A_i(Q)\mathcal{L}_i(Q,E)] \circledast R(Q,E) \tag{4.1}$$

Sometimes, it is important to set an E independent constant bkg (background) to represent the contribution from inelastic peak and the part of QENS which has a broader linewidth than the instrumental E range. Then a fitted result

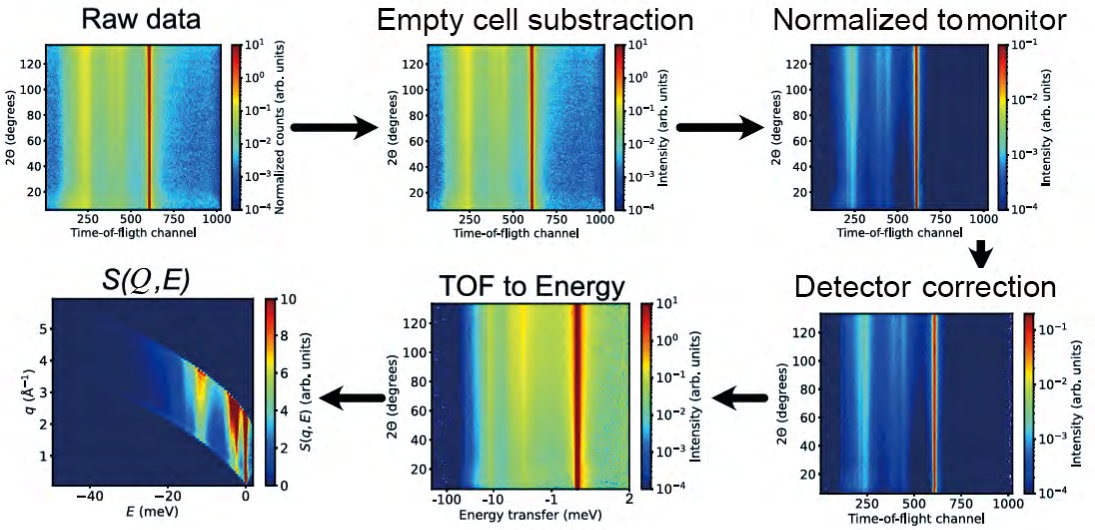

Figure 4.6: Flow chart of how the ToF raw data is corrected and reduced to $S(Q,E)$.[125] Used with permission of © Rasmus Lavén, 2023, from *Dynamical properties of metal halide and oxyhydride perovskite.* Doktorsavhandlingar vid Chalmers tekniska högskola, Ny series nr 5319.

can be collected for the QENS spectrum (example shown in Figure 4.7):

$$S(Q,E)_{\text{fitted}} = [A_0(Q)\delta(E) + \sum_{i\neq 0} A_i(Q)\mathcal{L}_i(Q,E) + bkg] \circledast R(Q,E) \quad (4.2)$$

Performing a fixed window scan (FWS) is commonly a useful and tool for analyzing the temperature dependence of QENS intensity. It can be obtained through a series of temperature scans over a specific energy transfer range which can give an overview of the dynamics of a sample. Experimentally, FWS can be measured by the spectrometers through the monochromator to choose the neutron wavelength, or it can be obtained by θ-integrated ToF spectrometer data. Elastic fixed window scans (EFWSs) can show the onset of motion whose correlation time is within the instrumental time window (Figure 4.8). The linear decreasing of EFWSs is from the mean square displacement $\langle u^2 \rangle(T)$ of atomic thermal vibration described by Debye-Waller factor [115]:

$$DWF = e^{-Q^2\langle u^2 \rangle} \quad (4.3)$$

4.2 Inelastic neutron scattering

INS is frequently employed to probe the internal vibrational dynamics of molecular crystals. Characterizing these vibrational dynamics via INS spectrometers lays a crucial foundation for understanding the macroscopic properties of materials, which are often determined by a complex balance or strong coupling between competing physical phenomena. INS instruments are broadly categorized into Triple-Axis Spectrometers (TAS) and Time-of-Flight (ToF) spectrometers.

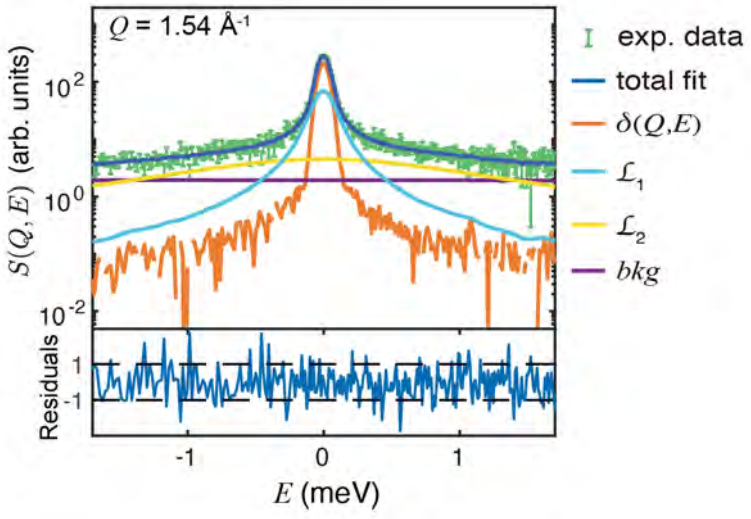

Figure 4.7: $S(Q,E)$ fitting example from the Paper 3 on a MHP sample at Q = 1.54 Å^{-1}, residual = $[S(Q,E)_{\text{fitted}} - S(Q,E)_{\text{exp.}}]/S(Q,E)_{\text{exp.error}}$.

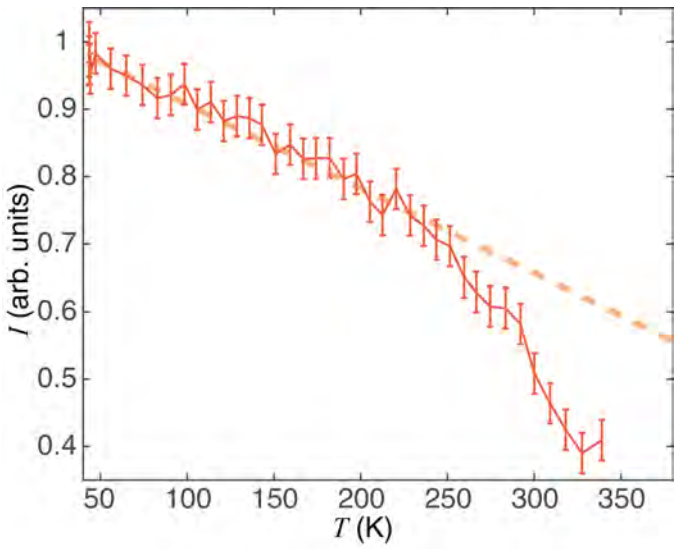

Figure 4.8: EFWSs example from Paper 3 where the dashed straight line can be described by Debye-Waller factor.

4.2.1 Indirect geometry spectrometer: TOSCA

TOSCA is an indirect geometry neutron spectrometer located at the ISIS Neutron and Muon Source in the UK. The instrument is specifically optimised for the study of molecular vibrations in the solid state.[126] As shown in Figure 4.9, the spectrometer consists of a cryostat, forward and backscattering analysers, and detectors.[127] Specifically, operating as an indirect geometry instrument, TOSCA does not monochromate the incident neutron energy, instead, it fixes the final scattered energy. After being scattered by the sample, the neutrons first pass through a pyrolytic graphite analyser and a beryllium filter maintained at cryogenic temperatures (< 50 K) to eliminate higher-order Bragg reflections. This configuration can fix the final neutron energy (E_f) at approximately 3.3 meV. Neutrons are finally collected by ^{3}He gas detectors. These detectors are arranged in a circular array and divided into two primary banks: forward scattering (corresponding to a scattering angle of approximately 45°) and backscattering (corresponding to a scattering angle of approximately 135°). It is worth noting that, this angle difference gives a **Q** difference. From the equation 3.17, at low E range (the momentum transfer Q is correspondingly small and the Debye-Waller factor approaches 1), the inelastic scattering intensity is proportional to Q^2. Due to the difference in Q^2 between these two trajectories at low energies, the observed INS peaks exhibit noticeable intensity variations between the forward and backward scattering spectra at low E range.[128] Following a series of recent upgrades aimed at reducing background noise and enhancing the signal-to-noise ratio, TOSCA can now cover an energy transfer range from -24 to 4000 cm^{-1} with a spectral resolution of approximately 1.25% of the energy transfer.[126,128]

To investigate the impact of illumination conditions on molecular vibrational modes, such as photoisomerization and the photoexcited state sample in our case, a specialized *in-situ* illumination environment was developed by the TO-

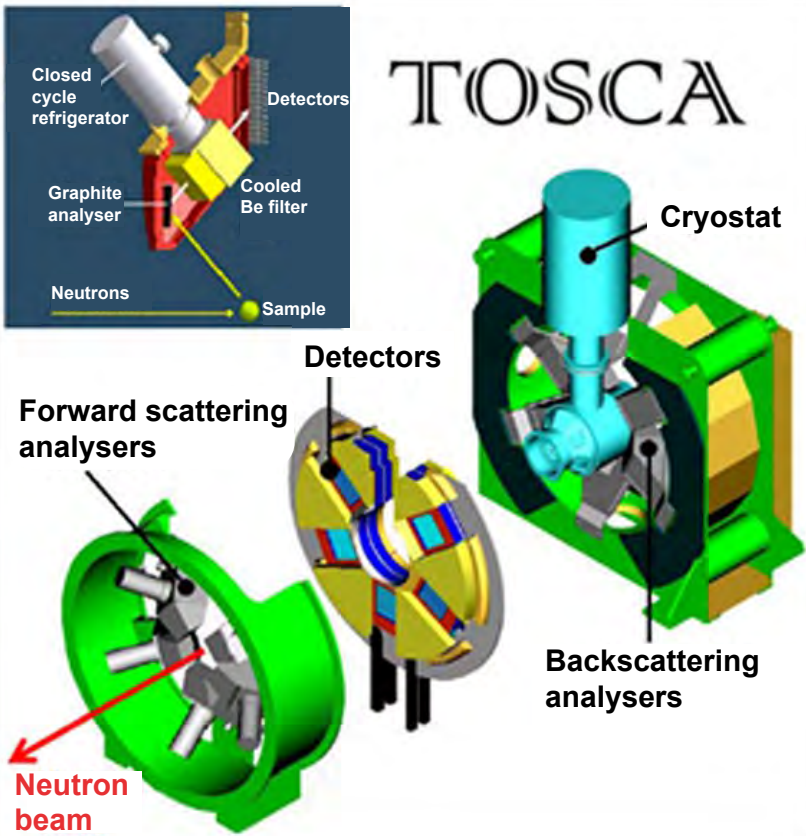

Figure 4.9: Schematic diagram of TOSCA. The inset shows a cross sectional view of a detector module.[128] Copyright © Institute of Physics, CC BY 3.0, from Stewart F Parker, et. al.

SCA beamline group.[129] As illustrated in Figure 4.10, this setup comprises an LED array (on both sides of the disk sample cell) integrated with an aluminum sample cell featuring transparent quartz windows. This unique environment paves the way for the investigations presented in this thesis regarding the organic cation dynamics of MHPs in their photo-excited states. It is worth noting that due to the inherent heat load generated by the operating LEDs, the minimum sample temperature within this setup is limited to approximately 50 K.

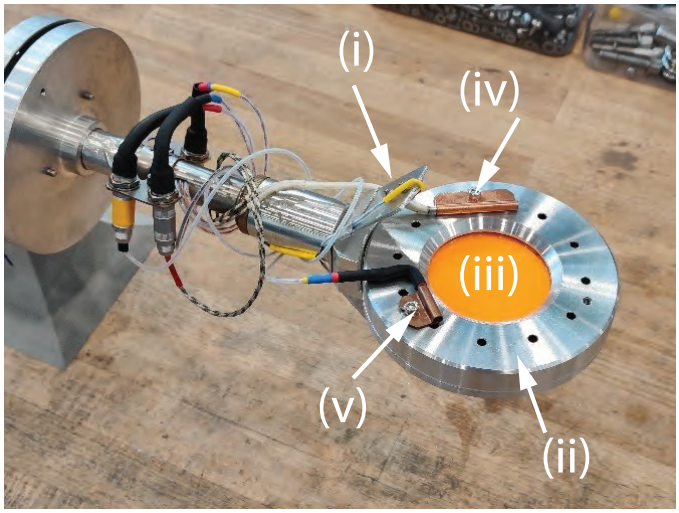

Figure 4.10: A photograph of the metal LED bracket (i) and illumination cell (ii) containing the $MAPbBr_3$ sample (iii), for use on TOSCA. Also visible are the cartridge heater (iv) and temperature sensor (v) for thermal control.

Chapter 5

Results and discussion

This chapter begins with a brief summary of the appended papers and finishes with a collective discussion of the results with a focus on how these results add to the current literature on dynamics in MHPs.

5.1 Localized organic cation dynamics in semi-0D metal halide composite $MBAMnCl_3{\cdot}2H_2O$ (Paper I)

In recent years, a semi-0D metal halide composite, $MBAMnCl_3 \cdot 2H_2O$, has been synthesized. Its unique crystal structure and composition enable it to have two photoluminescence (PL) emission centers, enabling excitation-dependent emission across different wavelength bands.[97] Furthermore, since MBA is a chiral organic cation, whether its specific chiral symmetry affects its localized dynamics poses an interesting question. Therefore, we investigated its structure using single-crystal X-ray diffraction (SC-XRD) and studied its organic cation dynamics via the QENS technique. The results of this study are presented below.

• Is it possible to obtain a more accurate description of the crystal structure of $MBAMnCl_3{\cdot}2H_2O$ on the basis of SC-XRD measurements?

As a technique based on the fitting of elastic peak broadening, QENS analysis relies on finding reasonable motion models which highly depend on the sample's structural properties. In order to get a better understanding of the MBA rotational dynamics properties in the novel MHP $MBAMnCl_3$, it is necessary to determine the crystal structure while the reported structure has an non-neglectable, and crystallographically unacceptable large uncertainty in the lattice parameter $a = 6$ (2) Å. A better SC-XRD result with higher accuracy of $MBAMnCl_3{\cdot}2H_2O$ monoclinic ($P2_1$) phase is obtained by our measurement (Figure 5.1a).

• Is there any different phase of $MBAMnCl_3{\cdot}2H_2O$? If so, which is the main phase in the sample?

Furthermore, the SC-XRD result from the same batch of samples but different crystals show a new monoclinic ($P2_1$) phase with ethanol ligands where the chemical formula is $MBAMnCl_3{\cdot}C_2H_5OH$ (Figure 5.1b). Interestingly, a similar but chloride-based perovskite system also has both 1D and 0D structures

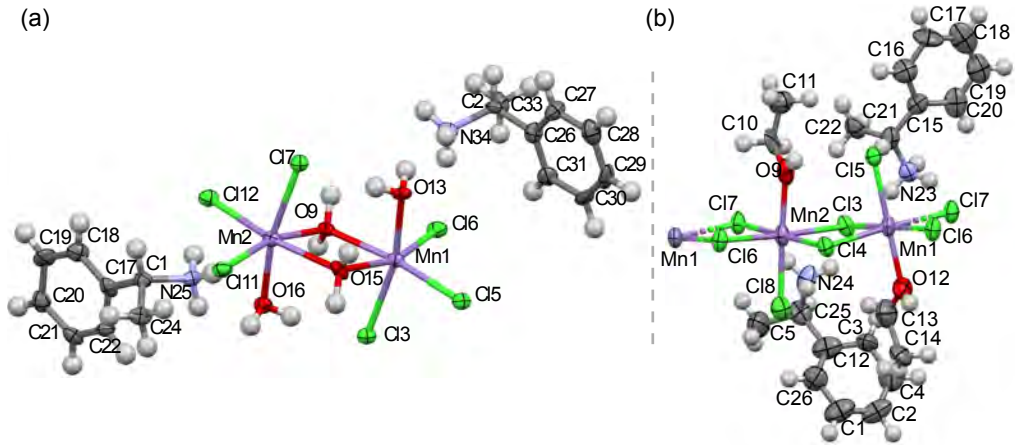

Figure 5.1: A view of the molecular crystal structure of (a) $MBAMnCl_3{\cdot}C_2H_5OH$ at 107 K, and (b) $MBAMnCl_3{\cdot}2H_2O$ at 100 K. The light grey spheres represent the hydrogen atoms.

where the transformation is because of the change in environment humidity.[130] This new phase might be transformed from $MBAMnCl_3{\cdot}2H_2O$ because of the different environments of storage and XRD sample preparation. However, P-XRD results show the main component of the crystals in the sample should still be $MBAMnCl_3{\cdot}2H_2O$ dimer structure. Therefore, the QENS analysis on this sample is still based on the $MBAMnCl_3{\cdot}2H_2O$ phase but with better quality of the structure information.

• What is the nature of the localized dynamics of the chiral organic cation (R)-MBA and (S)-MBA in (R)-/(S)-$MBAMnCl_3{\cdot}2H_2O$ including its geometry and timescale of the dynamics? How do the dynamics correlate to the investigated temperature and the type of enantiomer?

Building on our XRD structural study of $MBAMnCl_3{\cdot}2H_2O$, we investigated the dynamics of the MBA cation by QENS at FOCUS, PSI. Figure 5.2(a) shows the EFWSs results which have the similar temperature intensity changes for two samples upon heating and the onset of MBA diffusional dynamics can be found at around 275 K. Interestingly, comparing the EFWSs (elastic fixed windows scans) data upon heating with the data upon cooling, the thermal hysteresis of the elastic scattering intensity can be found from both samples (Figure 5.2a), and the full map of scattering temperature scans during cooling (Figure 5.2b) shows the (R)-$MBAMnCl_3{\cdot}2H_2O$ has a larger hysteresis than (S)-$MBAMnCl_3{\cdot}2H_2O$.

The key result of the geometry of the MBA cation dynamics is obtained from the EISF (elastic incoherent structure factor) fitting. A series of dynamical models which can fit the experimental data have been used, *i.e.* the jump-diffusion and rotational diffusion for the functional groups (*e.g.* -NH_3, -CH_3, and -C_6H_5), and the model at a higher temperature ($\geq$ 350 K) where the whole cation can have another rotation axis and hydrogens have biaxial rotational dynamics (Figure 5.3). The onset of methyl and ammonium 3-fold jump diffusion of MBA cation from $MBAMnCl_3{\cdot}2H_2O$ occurs at 270 K, and the 2-fold jump diffusion of phenyl could occur at 325 K. The QENS intensity increases

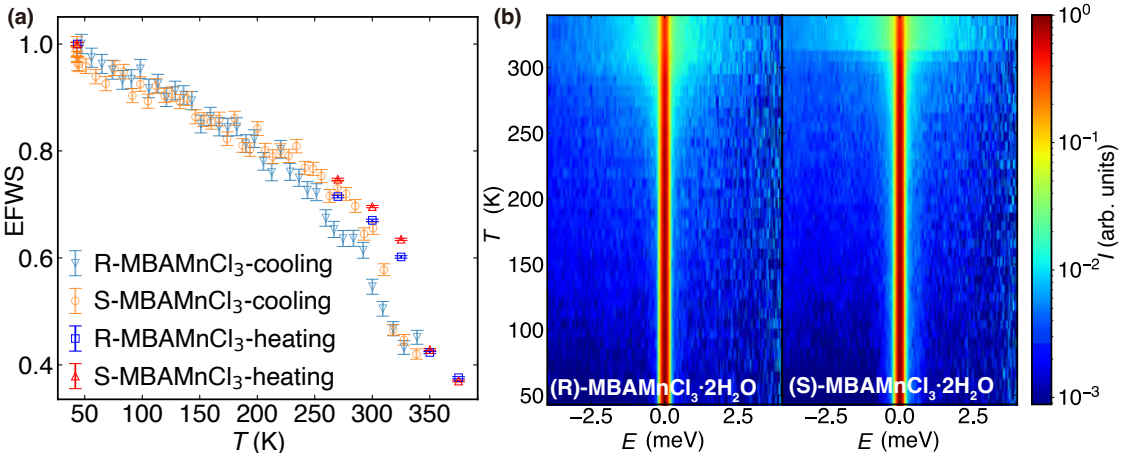

Figure 5.2: (a) EFWSs, and (b) temperature-dependent E distributed neutron scattering intensity $I(T,E)$ heatmaps of $MBAMnCl_3 \cdot 2H_2O$.

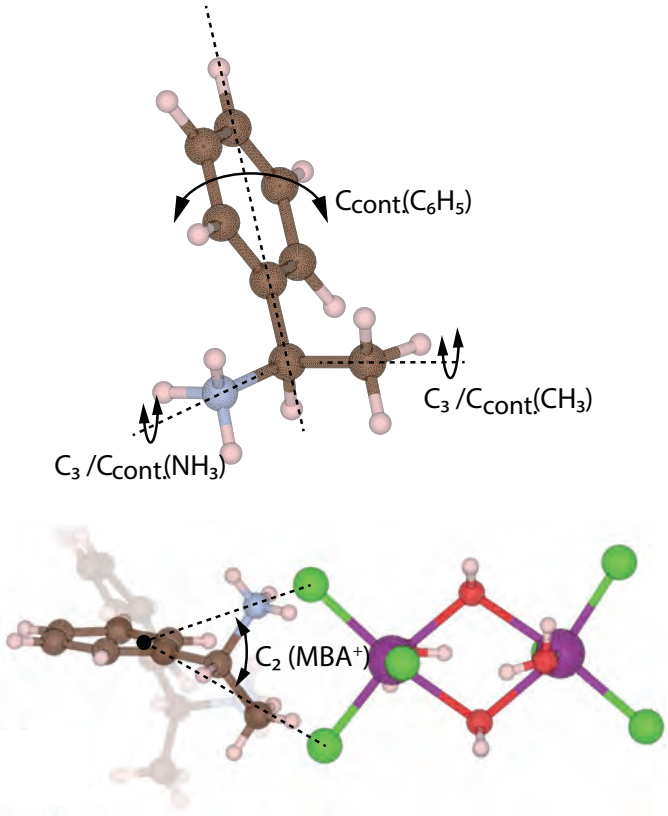

Figure 5.3: Schematic illustration of function groups (*e.g.* $-NH_3$, $-CH_3$, and $-C_6H_5$) jump-diffusion model, continuous rotational diffusion model, and whole cation C_2 jump-diffusion model.

rapidly from 325 to 350 K. At temperatures above 350 K, the dynamics become more complex, it has been considered as biaxial rotational diffusion where the second axis passes through the MBA mass centre and is perpendicular to the plane containing the mass centre and the two closest halide ions (Figure 5.3). The rotation angle of 48° comes from the angle of <Cl - mass centre - Cl> (Figure 5.3).

Compared to the other low-dimensional MHPs which also have relatively larger organic cations (ionic radius larger than $\sqrt{3} \times B{-}X$ bond length),[22,28] MBA also show localized function group's rotational dynamics in $MBAMnCl_3{\cdot}2H_2O$, but at higher temperature, MBA can have whole cation C_2 rotational diffusion which has not been reported from QENS study. The more complicated dynamics with a higher spatial freedom level could be led by the smaller energy barrier of MBA cation localized rotational diffusion, since each organic cation in semi-0D $MBAMnCl_3{\cdot}2H_2O$ is surrounded by fewer amount of halide ion than in other 2D MHPs in the same volume of crystal.

5.2 Rotational dynamics of organic cations in low-dimensi -onal MHP: the effect of the geometry of the organic cation (Paper II)

Recently, a new class of Dion-Jacobson type MHPs, with A = 1,3-phenylenediam -monium (1,3-PDA, PDA = $C_6H_5(NH_3)_2^{2+}$), 1,4-phenylenediammonium (1,4-PDA), and 1,4-xylylenediammonium (1,4-XDA, XDA = $C_6H_5(CH_2NH_3)_2^{2+}$), M = Pb, and X = Br, as well as the chemically similar but structurally dissimilar material $(1,3\text{-XDA})_2PbBr_6$ were reported.[98] This series of materials shares the same inorganic sublattice and similar diammonium organic cations, providing a great opportunity to systematically study how the geometry of the organic cation affects its localized dynamics.

Here are the results from the QENS measurements in FOCUS, PSI.

• What is the nature of localized diffusional dynamics of organic cations in $A PbBr_4$ (A = 1,3-PDA; 1,4-PDA; 1,4-XDA) and $(1,3\text{-XDA})_2PbBr_6$, and how does it depend on temperature?

For $A PbBr_4$ (A = 1,3-PDA, 1,4-PDA, 1,4-XDA) 2D MHP and 1,3-XDA_2 $PbBr_6$ 0D MHP, the Q-independent FWHM of fitted QENS signals and the EISF fitting reveals these cations have localized rotational diffusion in the picosecond time scale (Figure 5.4). The onset of ammonia 3-fold jump diffusion of 1,3-BA is at 200 K, of 1,3-BMA and 1,4-BA are at 250 K, of 1,4-BMA is at 350 K.

• What is the relation among the localized distortions of the $[PbBr_6]$ octahedron, structure of different diammoniums, and the localized diffusional dynamics of organic cations?

With a shorter and more asymmetric structure, which is less flexible, $(1,3\text{-PDA})PbBr_4$ has the most distorted local inorganic framework with the largest Br-Pb-Br angle in the octahedra and the largest angle between the octahedra.[98] With less flexible organic cation, the dynamics are also faster and more activated at the same temperature. At 350 K, the FWHM results show $\gamma_{(1,3-\mathrm{PDA})} > \gamma_{(1,3-\mathrm{XDA})} > \gamma_{(1,4-\mathrm{PDA})} > \gamma_{(1,4-\mathrm{XDA})}$. The immobile fraction of organic cations $c_{(1,4-\mathrm{PDA})} > c_{(1,4-\mathrm{XDA})} > c_{(1,3-\mathrm{XDA})} > c_{(1,3-\mathrm{PDA})}$.

• What is the correlation between organic cation dynamics and luminescence?

In general conclusion from the QENS results, it has been found that with higher symmetry (1,4->1,3-) and longer organic cation (XDA>PDA), the

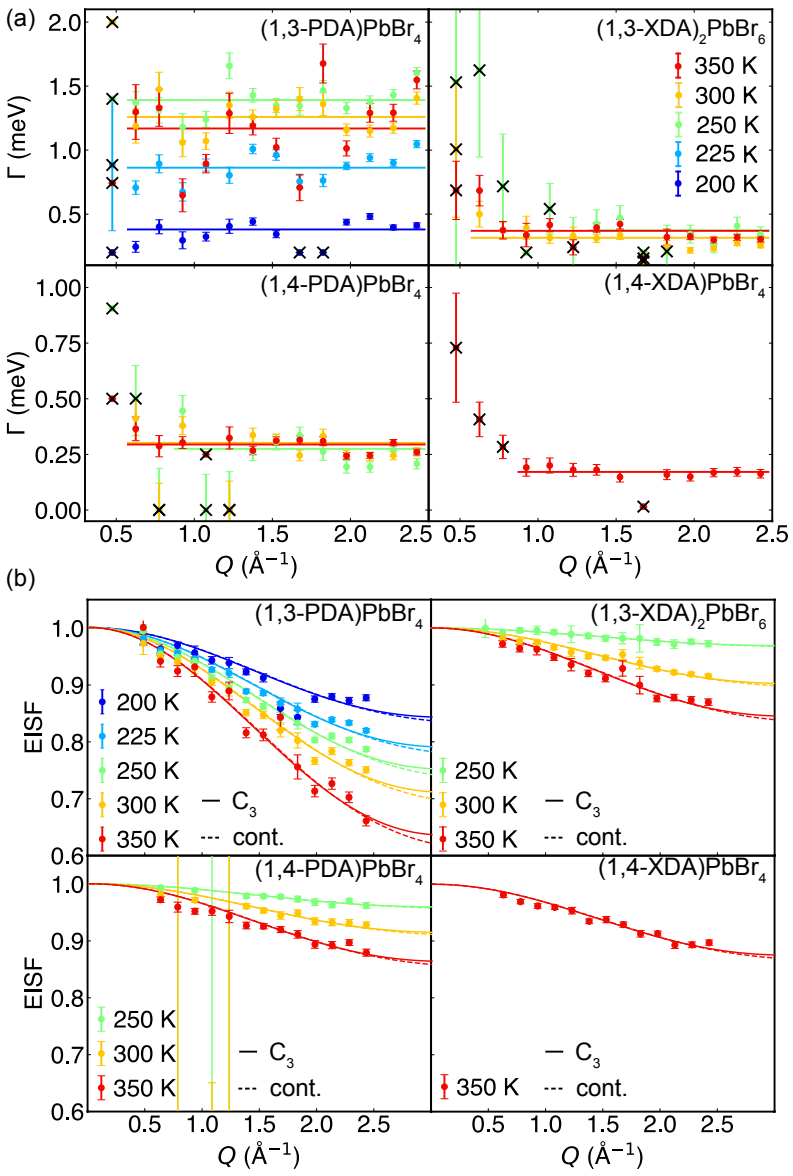

Figure 5.4: QENS results of 1,3/1,4-(PDA)$PbBr_4$, 1,3-XDA_2PbBr_6, and 1,4-(XDA)$PbBr_4$ including (a) linewidths of fitted Lorentzian at $Q \leq 2.5$ Å^{-1} where the solid lines represent the mean value, and (b) fitted EISF from -NH_3 3-fold jump-diffusion model with partial immobile fraction.

2D MHP [1,4-(XDA)$PbBr_4$] which has longer localized diffusional dynamics timescale and higher ratio of immobile fraction at the same temperature can show stronger and narrower PL emission intensity. Compared to other layered perovskites such as OA_2PbI_4 (OA cation = $C_8H_{17}NH_3^+$),[22] and A_2PbBr_4 [A = n-butylammonium (nBA), 1,8- diaminooctammonium (ODA), and 4-aminobutyric acid (GABA)],[28] the QENS results show the picosecond timescale of these big organic cations (compared to the organic cations in the 3D perovskites) dynamics are mainly contributed by their functional groups (*e.g.* methyl, ammonium) but not whole cation diffusion. Interestingly, the PL emission and the QENS study from A_2PbBr_4 [A = n-butylammonium (nBA), 1,8-diaminooctammonium (ODA), and 4-aminobutyric acid (GABA)] shows that

perovskite with smaller effective dynamic radii organic cations and restricted organic cation dynamics will bring less influence of the inorganic framework where the octahedral planes tilted more and cause the material to have more broadband emission.[28] This conclusion does not fully agree with our study where the 1,4-(XDA)$PbBr_4$ with the most restricted organic cation dynamics has the narrowest emission band. The details of the relationship and mechanism between organic cation dynamics and layered perovskite broadband emission need further exploration and discussion.

5.3 Localized dynamics of organic cations in 3D MHPs: the effect of X site anion and of photoexcitation (Paper III&IV)

To better understand the nature of the dynamics of FA cations in tin-based (lead-free) MHPs, $FASnCl_3$, $FASnBr_3$, and FA_2SnI_6 have been measured using QENS technique at FOCUS from PSI and DNA from Jparc. It is worth noting that the results of $FASnCl_3$ have not been mentioned in the paper due to its exact crystallographic structure remains not fully resolved. However, the diffraction data shows it has more distorted and smaller unit cell than other materials in this study, combined with its weak QENS results, it could be a good control group in this study.

• What is the nature of localized diffusional dynamics of FA in $FASnX_3$ (X = Cl, Br) and FA_2SnI_6, such as the geometry, timescale, and activation energy of the dynamics?

• How do the localized dynamics of FA cations change with temperature in $FASnX_3$ (X=Cl, Br) and FA_2SnI_6?

A series of temperature-dependent QENS signals has been probed from these samples (Figure 5.5). The EFWSs (elastic fixed window scans) reveal that the onset temperature of FA cation localized dynamics in $FASnBr_3$ and FA_2SnI_6 is around 150 K, while for $FASnCl_3$ it is around 250 K. Besides the different dynamics onset temperature, it can be observed that the QENS intensity for FA_2SnI_6 increases sharply between 200 and 225 K, for $FASnBr_3$ between 200 and 250 K, whereas for $FASnCl_3$ remains low below 300 K but becomes observable from 350 K (Figure 5.5).

From the Q^2 independent behaviour of the FWHM of the fitted QENS signal one can understand that the dynamics are localized in nature. The FWHM of the narrower Lorentzian ($\mathcal{L}_1$) from the fitting is around 0.1 – 0.5 meV, which translates into a timescale of the FA localized diffusion a few picoseconds. An Arrhenius fit of the temperature-dependent FWHM suggests an activation energy of 66±8 meV for $FASnBr_3$ and 50±8 meV for FA_2SnI_6.

Through the QENS fitting, 2- and 4-fold jump diffusion and isotropic reorientation models (Figure 5.6a) have been built up for $FASnBr_3$ and FA_2SnI_6 of their tetragonal phase (∼150 – 200 K) and cubic phase (∼230 – 350 K). The 24-site jump-diffusion model fits the data worse than the isotropic reorientation model (Figure 5.6b). This important result indicates that the influence of hydrogen bonds (which have directionality and can force hydrogens to point

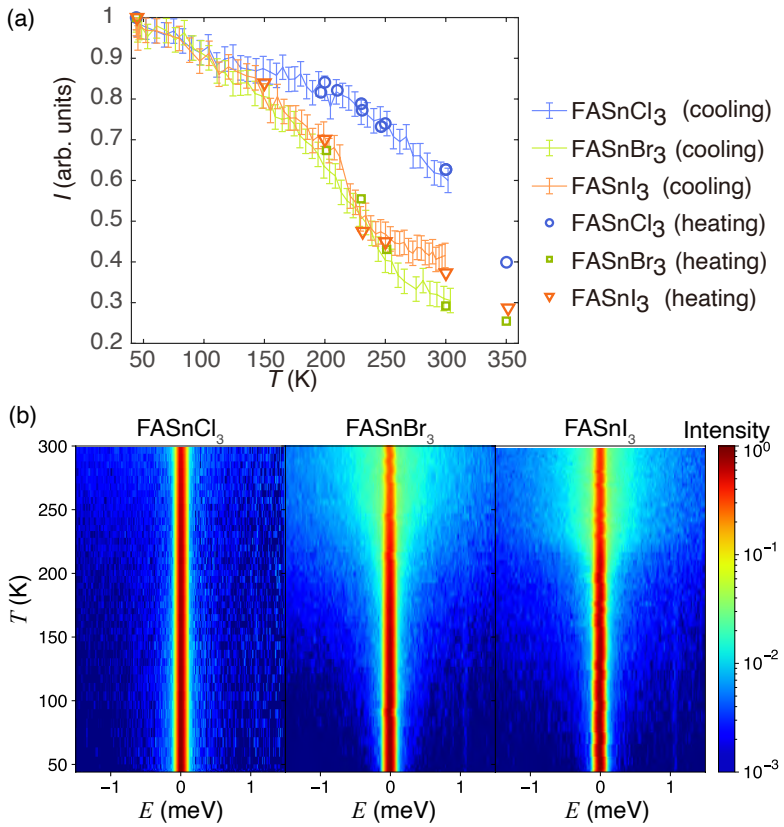

Figure 5.5: (a) EFWSs, and (b) temperature-dependent E distributed neutron scattering intensity $I(T,E)$ heatmaps of $FASnCl_3$, $FASnBr_3$ and FA_2SnI_6.

to halide ions) to FA cation rotational diffusion becomes weaker than in the orthorhombic phase in the cubic phase of $FASnBr_3$ and FA_2SnI_6 , which could be due to a higher unit cell volume (longer and weaker hydrogen bond) bringing lower energy barrier for FA cation diffusion and FA cation having higher thermal energy in cubic phase.

From the QENS results, one can conclude that the dynamical property of FA cation in the tin-based MHP system is dependent on the halide ion. With a longer halide ion radius [r_{I^-} (206 pm) > r_{Br^-} (182 pm) > r_{Cl^-} (167 pm)][131] and a larger unit cell [$a[Sn_{0.5}I_3]$ (6.17 Å)[106] $\gtrsim a[SnBr_3]$ (6.03 Å)[132] $\gtrsim a[SnCl_3]$ (5.79 Å, non-cubic)[133]], the tin-based perovskite can have a stronger QENS intensity at the same temperature. Reflected on the cation dynamics, this represents FA cations can have a faster and higher spatial freedom level of the localized diffusion with a larger halide ion and the same B-site cation in MHPs.

• How does the FA cation dynamics compare with the FA cation dynamics in prototypical $FAPbX_3$ (X=Cl, Br, I)?

Compared to $FAPbX_3$ (X= Br, and I), the localized diffusional dynamics of FA cations are of tin-based perovskite at cubic phase have a similar timescale at 300 K ($FAPbI_3$: 1.26 ps,[31] $FAPbBr_3$: 5.6 ps[25]), and similar activation energy level in the cubic phase ($FAPbI_3$: 52 ± 6 meV,[32] $FAPbBr_3$: 61.8 ± 5 meV[25]), and the same isotropic reorientation geometry to the lead-based perovskite (comprehensive comparison can be found in the SI of Paper 1 Table S2). These results reveal that there is no direct interaction between the dynamics of the

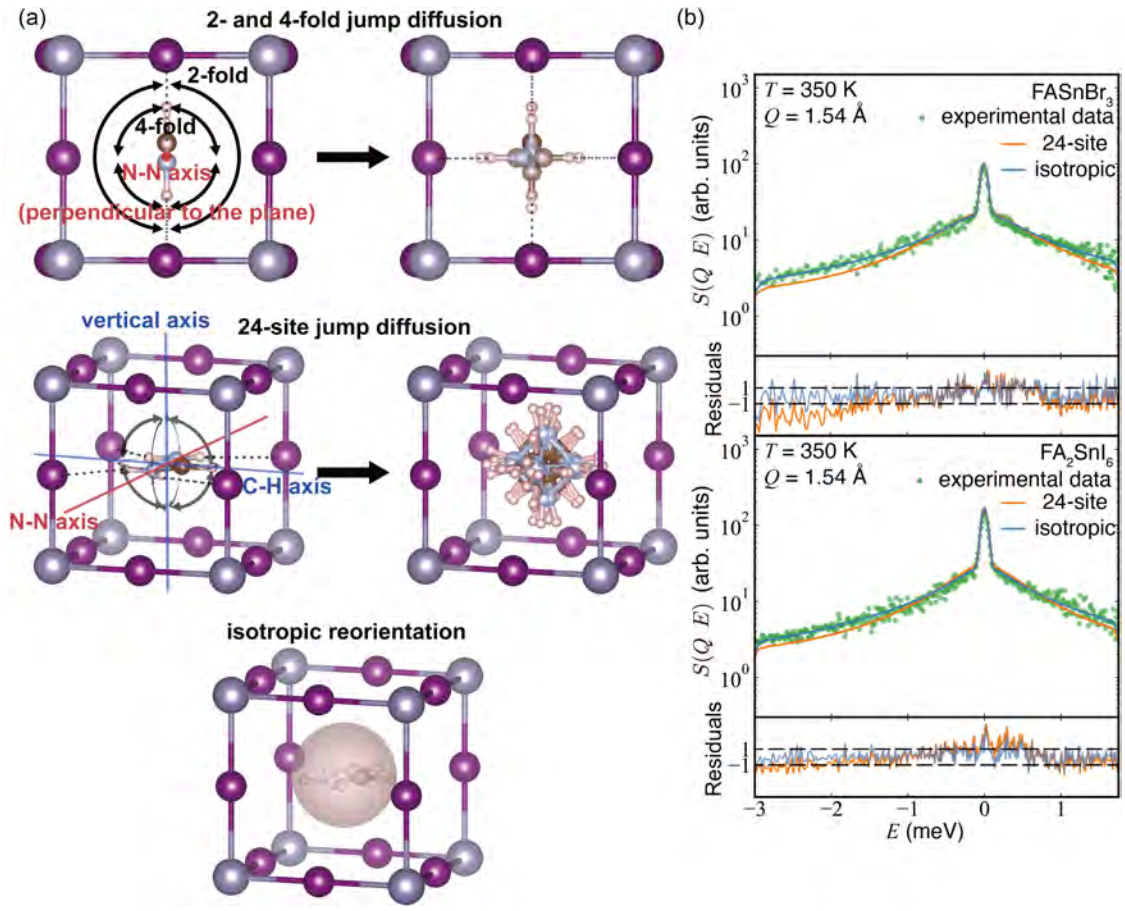

Figure 5.6: (a) Schematic illustration of rotational motion models of the FA cation, and (b) $S(Q, E)$ fitting of $FASnBr_3$, and FA_2SnI_6 at 350 K, $Q = 1.54$ Å.

organic cations and the B-site divalent metal cation, but that the dynamics of the organic cations highly depend on the type of halide anion.

To better understand how organic cation dynamics affect the optoelectronic performance and practical applications of MHPs, we need to investigate if and how these dynamics change under photoexcitation. Using the *in-situ* illumination environment at the TOSCA INS spectrometer, we performed a series of INS measurements on $MAPbBr_3$.

Here are the collected results.

• What is the nature of vibrational dynamics of $MAPbBr_3$?

In agreement with the literature (Figure 5.7), we can find clear bands in the range of 10–65 cm^{-1} are related to octahedral twist motions, bands in the range of 65–120 cm^{-1} are related to nodding motions of the MA cation, bands in the range of 120–210 cm^{-1} are related to lurching motions of the MA cation, and the band at approximately 295 cm^{-1} relates to a C-N torsion motion of the MA cation.[17,89]

• What is the nature of vibrational dynamics of optical-excited-state $MAPbBr_3$?

As illustrated in Figure 5.7 and Figure 5.8, the INS spectra under LED-on and LED-off conditions are similar, with only small intensity variations observed

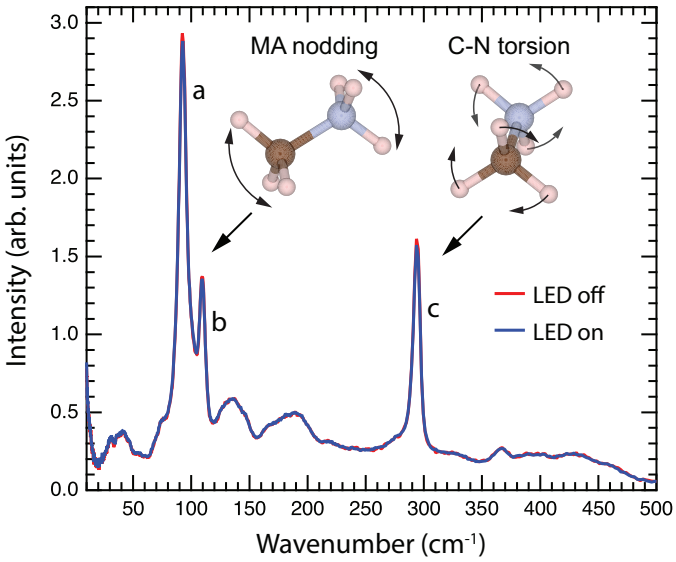

Figure 5.7: INS spectrum of $MAPbBr_3$, as measured at 50.7 K, and for LED off (red color) and LED on (blue color). The strongest bands, at around 90, 110, and 295 cm^{-1}, are marked with a, b, and c. Included in the graph are schematic illustrations of the MA nodding (65–120 cm^{-1}) and C-N torsion (295 cm^{-1}) motions. Light blue spheres represent nitrogen, brown spheres represent carbon, and light pink spheres represent hydrogen.

in a few MA related peaks. This similarity primarily originates from the fact that the light absorption depth is on a sub-micron scale, whereas the sample thickness for the INS experiment is on a sub-millimeter scale. Consequently, the surface-to-volume ratio under the current in-situ illumination environment remains relatively low. Detailed data comparison reveals that these spectral differences are still significant and reproducible under the specific illumination conditions. These affected peaks are attributed to the MA libration and C-N torsion modes.

• How does the exciton affect the vibrational dynamics of $MAPbBr_3$?

Because of the generally soft nature of the lattices of HPs,[87,134] the photogenerated charge carriers or excitons can couple to phonons and molecular

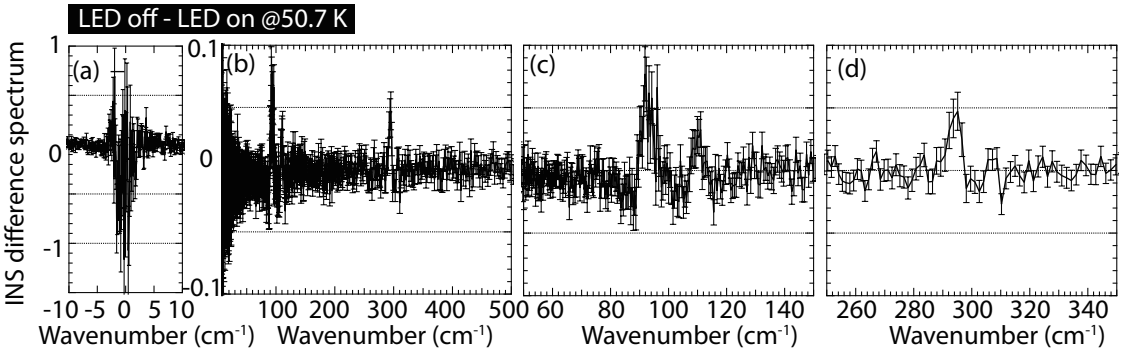

Figure 5.8: INS difference spectrum (LED off - LED on) of $MAPbBr_3$, as measured at 50.7 K and plotted over different energy regions.

vibrational modes, giving rise to polarons or self-trapped excitons, respectively, which subsequently leads to lower charge carrier mobility and influences the probability of charge recombination.[135–137] Whether organic cations actively participate in these processes remains a subject of ongoing debate. Although our current findings do not permit a rigorous quantitative analysis of the specific relationship between cation dynamics and excitons, they provide qualitative evidence supporting their involvement. Given that the observed libration modes are intrinsically coupled with the vibrations of the inorganic octahedral framework, it is reasonable to hypothesize that MA cations engage in a complex coupling mechanism involving both photogenerated excitons and the local structure distortion within HPs. These observations establish a preliminary foundation for future investigations into such intricate mechanisms via neutron scattering, which could be further realized through the optimization of experimental conditions.

5.4 Discussion

The experimental results across this series of MHPs reveal a complex landscape of internal dynamic coupling, fundamentally due to their inherently soft lattices. These dynamics are governed by a multifaceted interplay of factors, including temperature, the intrinsic molecular structure of the cation, the local environment of the inorganic sublattice, and external factors such as photo-induced excitons.

The various localized motions, including diffusion and vibration, are thermally driven which is linked to temperature. As temperature increases, assuming without the phase transitions, the localized diffusion modes of the organic cations generally evolve toward higher frequencies and greater complexity. This is shown as shorter relaxation times (τ) and an increased occupancy of resident sites. For instance, in MBA-based systems, a global C_2 rotation coupled with the functional group's own rotational diffusion emerges above 350 K.

Indeed, the molecular structure of the cation also influences the distortion and connectivity of the inorganic sublattice. Observations from a series of PbBr-based diammonium low-dimensional MHPs indicate that the $Br - Pb - Br$ bond angles and inter-octahedral tilting vary with different A-site diammonium cations. Since DFT calculations suggest no systematic differences in hydrogen bonding strengths across these systems,[98] the variations in NH_3 functional group dynamics likely originate from the cations' intrinsic structure. The QENS results show that the more flexible cations (greater length and symmetry) exhibit higher onset temperatures for picosecond-scale NH_3 dynamics [1,3-PDA (200 K) < 1,4-PDA (250 K) < 1,4-XDA (350 K)] and longer relaxation time (τ) at the same temperature [350 K: 1,3-PDA (1.2 ps) < 1,4-PDA (4.7 ps) < 1,4-XDA (9.5 ps)]. This suggests that these differences stem from a redistribution of thermal energy where higher flexibility introduces more localized dynamical modes. For instance, the benzene rotational diffusion (typically on the nanosecond scale) is potentially present in 1,4-PDA/XDA, which is less likely to be present in 1,3-PDA/XDA due to their stronger steric hindrance or higher activation energy for the rotation.

The dynamics of the same organic cation can also vary in different inorganic sublattices. In this study, the localized diffusion of FA in various Sn-based MHPs using QENS has been systematically investigated. Comparing this with literature data for Pb-based MHPs, we observed that while the modes of motion are similar (C_2/C_4 or isotropic reorientation), the diffusion rates differ based on the sublattice. Generally, the diffusion rate correlates positively with the effective cavity volume of the inorganic octahedra. The halide ion is the primary determinant, where MHPs formed with larger halide radii ($I^- > Br^- > Cl^-$) possess larger unit cells, resulting in faster FA diffusion rates at equivalent temperatures. Conversely, the B-site divalent metal cation has a negligible effect, leading to similar FA diffusion rates in Pb and Sn-based MHPs with the same halide. Notably, the double perovskite FA_2SnI_6, with a sub-unit cell size between $FASnI_3$ and $FASnBr_3$, exhibits an FA diffusion rate that is also intermediate, further supporting our conclusion. This suggests that the effective spatial confinement, specifically the distance between the FA cation and the nearest octahedral cage, dictates the localized hydrogen bonding strength and steric hindrance, thereby modulating the activation energy for localized diffusion. Similarly, the picosecond-scale whole cation rotational dynamics observed in the pseudo-0D structure $MBAMnCl_3 \cdot 2H_2O$ likely benefit from its exceptionally loose crystal packing compared to 2D diammonium systems.

Finally, combining our *in-situ* illumination INS measurement of $MAPbBr_3$, a clearer picture of existence of complex coupling shows among the excitons, the inorganic sublattice, and the organic cations. These complex competing and synergistic dynamics likely provide the mechanistic basis for the high carrier mobility and defect tolerance observed in MHPs. Our findings emphasize that a better understanding of the mechanisms behind high-performance photovoltaic conversion necessitates more dynamical characterization. Such efforts are essential to construct a comprehensive cognitive framework for these unique materials.

Chapter 6

Summary and Conclusions

In summary, by utilizing quasielastic and inelastic neutron scattering techniques, this work has systematically mapped the localized dynamics of various organic cations within metal halide perovskites (MHPs) and elucidated their underlying physical driving forces.

Investigating the effect of semi-0D structural confinement on the cation dynamics in $MBAMnCl_3 \cdot 2H_2O$, we conclude that the large localized free space provided by the unique unit cell enables highly complex and strong diffusional dynamics. This specific structural environment allows for the rotation of functional groups coupled with the entire MBA cation jump diffusion at picosecond timescale, which is unusual for large organic cations in non-3D MHPs.

In the work of 2D diammonium lead bromides, our study of organic cation geometry reveals that increased cation length and flexibility may suppress the rotational diffusion of the terminal ammonium. At a given temperature, more flexible cations likely distribute thermal energy into alternative dynamic modes (such as phenyl ring rotation), thereby increasing the thermal threshold required for the localized rotation of terminal functional groups.

With regards to our study of the effect of X-site anion on the localized dynamics of organic cation in 3D MHPs $FASnX_3$ (X = Br, I) and FA_2SnI_6, we can conclude that these localized dynamics are governed by the cavity volume provided by the inorganic sublattice. Regardless of the specific B-site metal, X-site halide, or vacancy ordering, a larger localized free space consistently correlates with stronger organic cation dynamics, characterized by higher mobility and more complex motion types.

By examining the effect of photoexcitation on the local structural properties of $MAPbBr_3$, the organic cations are suggested as not merely passive structural components. Instead, they interact dynamically with the inorganic sublattice, excitons, and polarons, indicating that organic cation dynamics play an active role in the dynamic optoelectronic response of MHP systems.

Finally, this thesis establishes the feasibility of using neutron scattering to unravel the complex dynamic couplings within MHP systems, providing a foundation for future materials study.

Acknowledgment

Firstly, I would like to thank my supervisor Maths Karlsson, for giving me the opportunity to join this interesting Ph.D. project and for his great support in scientific research and academic writing. I would also like to thank my vice supervisor Feng Gao, for his support and advice in sample preparation and material science. I would like to thank my examiner Bo Albinsson and my study director Itai Panas, for their mature and wise study guidance, advice, and knowledge sharing. I would also like to thank my manager Henrik Leion, and administrator Sandra Nayeri, for their help in my study in Chalmers. I would like to thank my collaborators and mentors Lars Öhrström, Lorenzo Malavasi, Weidong Cai, Fanni Juranyi, Michael Koza, Markus Appel, Masato Matsuura, Hiromu Tamatsukuri, Hamish Cavaye, Michael Marek Koza, Lars-Gunnar Johansson, Svemir Rubic, and Stewart Parker, for all their help in my scientific research, neutron experiments, and sample preparation. I would also like to thank my group mates and friends in Chalmers, Rasmus Lavén, Elena Naumovska, Lucas Fine, Aymen Yangui, Pedram Pakmehr, Joanna Jedon, David Reinsfelt, Oskar Öjstedt, Diego Maini, Hugo Mårtensson, and Erika Magnusson for sharing the happiness, cookies, and beer. I would also like to thank all my friends from the SwedNESS, the time spent with you has been as precious as my youthful school days. I would like to give great thanks to all my family and friends around the world, I cannot wait to meet you again.

Finally, I would like to thank this Ph.D. journey itself. For me, it has been the most human experience I have ever encountered. Though filled with hardships, we still must believe the Ph.D. journey is a happy one, maybe more than what one must imagine Sisyphus happy. To close this chapter, I would like to conclude this journey by quoting the highly respected Professor Dumbledore: "*Nitwit! Blubber! Oddment! Tweak!*"

Thank you all once again! Thank you for reading this far!

Bibliography

[1] E. Masanet, A. Shehabi, N. Lei, S. Smith and J. Koomey, Recalibrating global data center energy-use estimates. *Science*, 2020, **367**, 984–986.

[2] S. D. Stranks and H. J. Snaith, Metal-halide perovskites for photovoltaic and light-emitting devices. *Nat. Nanotechnol.*, 2015, **10**, 391–402.

[3] A. Fakharuddin, M. K. Gangishetty, M. Abdi-Jalebi, S.-H. Chin, A. R. bin Mohd Yusoff, D. N. Congreve, W. Tress, F. Deschler, M. Vasilopoulou and H. J. Bolink, Perovskite light-emitting diodes. *Nat. Electron.*, 2022, **5**, 203–216.

[4] G. Rose, Beschreibung einiger neuen Mineralien des Urals. *Ann. Phys.*, 1839, **124**, 551–573.

[5] J. H. Heo, S. H. Im, J. H. Noh, T. N. Mandal, C.-S. Lim, J. A. Chang, Y. H. Lee, H.-j. Kim, A. Sarkar, M. K. Nazeeruddin, M. Grätzel and S. I. Seok, Efficient inorganic–organic hybrid heterojunction solar cells containing perovskite compound and polymeric hole conductors. *Nat. Photonics*, 2013, **7**, 486–491.

[6] Y. Rong, Y. Hu, A. Mei, H. Tan, M. I. Saidaminov, S. I. Seok, M. D. McGehee, E. H. Sargent and H. Han, Challenges for commercializing perovskite solar cells. *Science*, 2018, **361**, 6408.

[7] `www.nrel.gov/pv/cell-efficiency.html`.

[8] A. Polman, M. Knight, E. C. Garnett, B. Ehrler and W. C. Sinke, Photovoltaic materials: Present efficiencies and future challenges. *Science*, 2016, **352**, aad4424.

[9] D. A. Egger, A. Bera, D. Cahen, G. Hodes, T. Kirchartz, L. Kronik, R. Lovrincic, A. M. Rappe, D. R. Reichman and O. Yaffe, What Remains Unexplained about the Properties of Halide Perovskites? *Adv. Mater.*, 2018, **30**, 1800691.

[10] Z. Guo, J. Wang and W.-J. Yin, Atomistic origin of lattice softness and its impact on structural and carrier dynamics in three dimensional perovskites. *Energy Environ. Sci.*, 2022, **15**, 660–671.

[11] J.-W. Lee, S. Seo, P. Nandi, H. S. Jung, N.-G. Park and H. Shin, Dynamic structural property of organic-inorganic metal halide perovskite. *iScience*, 2021, **24**, 101959.

[12] T. Chen, B. J. Foley, B. Ipek, M. Tyagi, J. R. Copley, C. M. Brown, J. J. Choi and S. H. Lee, Rotational dynamics of organic cations in the $CH_3NH_3PbI_3$ perovskite. *Phys. Chem. Chem. Phys.*, 2015, **17**, 31278–86.

[13] A. M. Leguy, J. M. Frost, A. P. McMahon, V. G. Sakai, W. Kockelmann, C. Law, X. Li, F. Foglia, A. Walsh, B. C. O'Regan, J. Nelson, J. T. Cabral

and P. R. Barnes, Corrigendum: The dynamics of methylammonium ions in hybrid organic-inorganic perovskite solar cells. *Nat. Commun.*, 2015, **6**, 7780.

[14] I. P. Swainson, C. Stock, S. F. Parker, L. Van Eijck, M. Russina and J. W. Taylor, From soft harmonic phonons to fast relaxational dynamics in $CH_3NH_3PbBr_3$. *Phys. Rev. B*, 2015, **92**, 100303.

[15] K. L. Brown, S. F. Parker, I. R. García, S. Mukhopadhyay, V. G. Sakai and C. Stock, Molecular orientational melting within a lead-halide octahedron framework: The order-disorder transition in $CH_3NH_3PbBr_3$. *Phys. Rev. B*, 2017, **96**, 174111.

[16] B. Li, Y. Kawakita, Y. Liu, M. Wang, M. Matsuura, K. Shibata, S. Ohira-Kawamura, T. Yamada, S. Lin, K. Nakajima and S. F. Liu, Polar rotor scattering as atomic-level origin of low mobility and thermal conductivity of perovskite $CH_3NH_3PbI_3$. *Nat. Commun.*, 2017, **8**, 16086.

[17] E. M. Mozur, A. E. Maughan, Y. Q. Cheng, A. Hug, N. Jalarvo, L. L. Daemen and J. R. Neilson, Orientational Glass Formation in Substituted Hybrid Perovskites. *Chem. Mater.*, 2017, **29**, 10168–10177.

[18] J. Li, M. Bouchard, P. Reiss, D. Aldakov, S. Pouget, R. Demadrille, C. Aumaitre, B. Frick, D. Djurado, M. Rossi and P. Rinke, Activation Energy of Organic Cation Rotation in $CH_3NH_3PbI_3$ and $CD_3NH_3PbI_3$: Quasi-Elastic Neutron Scattering Measurements and First-Principles Analysis Including Nuclear Quantum Effects. *J. Phys. Chem. Lett.*, 2018, **9**, 3969–3977.

[19] K. T. Munson, G. S. Doucette, E. R. Kennehan, J. R. Swartzfager and J. B. Asbury, Vibrational Probe of the Structural Origins of Slow Recombination in Halide Perovskites. *J. Phys. Chem. C*, 2019, **123**, 7061–7073.

[20] G. Schuck, F. Lehmann, J. Ollivier, H. Mutka and S. Schorr, Influence of Chloride Substitution on the Rotational Dynamics of Methylammonium in $MAPbI_{3-x}Cl_x$ Perovskites. *J. Phys. Chem. C*, 2019, **123**, 11436–11446.

[21] M. Songvilay, Z. Wang, V. G. Sakai, T. Guidi, M. Bari, Z. G. Ye, G. Xu, K. L. Brown, P. M. Gehring and C. Stock, Decoupled molecular and inorganic framework dynamics in $CH_3NH_3PbCl_3$. *Phys. Rev. Mater.*, 2019, **3**, 125406.

[22] X. Hu, D. Zhang, T. Chen, A. Z. Chen, E. N. Holmgren, Q. Zhang, D. M. Pajerowski, M. Yoon, G. Xu, J. J. Choi and S. H. Lee, Crystal structures and rotational dynamics of a two-dimensional metal halide perovskite $(OA)_2PbI_4$. *Th The Journal of Chemical Physics e Journal of Chemical Physics*, 2020, **152**, 014703.

[23] A. Johnston, G. Walters, M. I. Saidaminov, Z. Huang, K. Bertens, N. Jalarvo and E. H. Sargent, Bromine Incorporation and Suppressed Cation Rotation in Mixed-Halide Perovskites. *ACS Nano*, 2020, **14**, 15107–15118.

[24] E. M. Mozur, M. A. Hope, J. C. Trowbridge, D. M. Halat, L. L. Daemen, A. E. Maughan, T. R. Prisk, C. P. Grey and J. R. Neilson, Cesium Substitution Disrupts Concerted Cation Dynamics in Formamidinium Hybrid Perovskites. *Chem. Mater.*, 2020, **32**, 6266–6277.

[25] V. K. Sharma, R. Mukhopadhyay, A. Mohanty, M. Tyagi, J. P. Embs and D. D. Sarma, Contrasting Behaviors of FA and MA Cations in $APbBr_3$. *J. Phys. Chem. Lett.*, 2020, **11**, 9669–9679.

[26] K. Druzbicki, R. Lavén, J. Armstrong, L. Malavasi, F. Fernandez-Alonso and M. Karlsson, Cation Dynamics and Structural Stabilization in Formamidinium Lead Iodide Perovskites. *J. Phys. Chem. Lett.*, 2021, **12**, 3503–3508.

[27] V. K. Sharma, R. Mukhopadhyay, A. Mohanty, V. G. Sakai, M. Tyagi and D. D. Sarma, Contrasting Effects of FA Substitution on MA/FA Rotational Dynamics in $FA_xMA_{1-x}PbI_3$. *J. Phys. Chem. C*, 2021, **125**, 13666–13676.

[28] A. A. Koegel, E. M. Mozur, I. W. H. Oswald, N. H. Jalarvo, T. R. Prisk, M. Tyagi and J. R. Neilson, Correlating Broadband Photoluminescence with Structural Dynamics in Layered Hybrid Halide Perovskites. *J. Am. Chem. Soc.*, 2022, **144**, 1313–1322.

[29] A. A. Koegel, I. W. H. Oswald, C. Rivera, S. L. Miller, M. J. Fallon, T. R. Prisk, C. M. Brown and J. R. Neilson, Influence of Inorganic Layer Thickness on Methylammonium Dynamics in Hybrid Perovskite Derivatives. *Chem. Mater.*, 2022, **34**, 8316–8323.

[30] V. K. Sharma, R. Mukhopadhyay, A. Mohanty, V. García Sakai, M. Tyagi and D. D. Sarma, Influence of the Halide Ion on the A-Site Dynamics in $FAPbX_3$ (X = Br and Cl). *J. Phys. Chem. C*, 2022, **126**, 7158–7168.

[31] R. Lavén, M. M. Koza, L. Malavasi, A. Perrichon, M. Appel and M. Karlsson, Rotational Dynamics of Organic Cations in Formamidinium Lead Iodide Perovskites. *J. Phys. Chem. Lett.*, 2023, **14**, 2784–2791.

[32] C. Yu, Y. Kawakita, T. Kikuchi, M. Kofu, T. Honda, Z. Zhang, Z. Zhang, Y. Liu, S. F. Liu and B. Li, Atomic Structure and Dynamics of Organic–Inorganic Hybrid Perovskite Formamidinium Lead Iodide. *J. Phys. Chem. Lett.*, 2024, **15**, 329–338.

[33] V. Goldschmidt, Die Gesetze der Krystallochemie. *Naturwissenschaften*, 1926, **14**, 477–485.

[34] H. Megaw, Crystal Structure of Barium Titanate. *Nature*, 1945, **155**, 484–485.

[35] S. D. Stranks, Nonradiative Losses in Metal Halide Perovskites. *Acs Energy Lett.*, 2017, **2**, 1515–1525.

[36] S. Rühle, Tabulated values of the Shockley–Queisser limit for single junction solar cells. *Sol. Energy*, 2016, **130**, 139–147.

[37] J.-H. Wei, X.-D. Wang, J.-F. Liao and D.-B. Kuang, High Photoluminescence Quantum Yield (>95%) of $MAPbBr_3$ Nanocrystals via Reprecipitation from Methylamine-$MAPbBr_3$ Liquid. *ACS Appl. Electron. Mater.*, 2020, **2**, 2707–2715.

[38] S. D. Stranks, V. M. Burlakov, T. Leijtens, J. M. Ball, A. Goriely and H. J. Snaith, Recombination Kinetics in Organic-Inorganic Perovskites: Excitons, Free Charge, and Subgap States. *Phys. Rev. Appl.*, 2014, **2**, 034007.

[39] P. J. Cegielski, A. L. Giesecke, S. Neutzner, C. Porschatis, M. Gandini, D. Schall, C. A. R. Perini, J. Bolten, S. Suckow, S. Kataria, B. Chmielak, T. Wahlbrink, A. Petrozza and M. C. Lemme, Monolithically Integrated Perovskite Semiconductor Lasers on Silicon Photonic Chips by Scalable Top-Down Fabrication. *Nano Lett.*, 2018, **18**, 6915–6923.

[40] Q. Zhang, Q. Shang, R. Su, T. T. H. Do and Q. Xiong, Halide Perovskite Semiconductor Lasers: Materials, Cavity Design, and Low Threshold. *Nano Lett.*, 2021, **21**, 1903–1914.

[41] Q. Shang, M. Li, L. Zhao, D. Chen, S. Zhang, S. Chen, P. Gao, C. Shen, J. Xing, G. Xing, B. Shen, X. Liu and Q. Zhang, Role of the Exciton–Polariton in a Continuous-Wave Optically Pumped $CsPbBr_3$ Perovskite Laser. *Nano Lett.*, 2020, **20**, 6636–6643.

[42] G. Maculan, A. D. Sheikh, A. L. Abdelhady, M. I. Saidaminov, M. A. Haque, B. Murali, E. Alarousu, O. F. Mohammed, T. Wu and O. M. Bakr, $CH_3NH_3PbCl_3$ Single Crystals: Inverse Temperature Crystallization and Visible-Blind UV-Photodetector. *J. Phys. Chem. Lett.*, 2015, **6**, 3781–3786.

[43] Q. Lin, A. Armin, P. L. Burn and P. Meredith, Near infrared photodetectors based on sub-gap absorption in organohalide perovskite single crystals. *Laser Photonics Rev.*, 2016, **10**, 1047–1053.

[44] L. Zhang, L. Mei, K. Wang, Y. Lv, S. Zhang, Y. Lian, X. Liu, Z. Ma, G. Xiao, Q. Liu, S. Zhai, S. Zhang, G. Liu, L. Yuan, B. Guo, Z. Chen, K. Wei, A. Liu, S. Yue, G. Niu, X. Pan, J. Sun, Y. Hua, W.-Q. Wu, D. Di, B. Zhao, J. Tian, Z. Wang, Y. Yang, L. Chu, M. Yuan, H. Zeng, H.-L. Yip, K. Yan, W. Xu, L. Zhu, W. Zhang, G. Xing, F. Gao and L. Ding, Advances in the Application of Perovskite Materials. *Nano-Micro Lett.*, 2023, **15**, 177.

[45] L. Mao, C. C. Stoumpos and M. G. Kanatzidis, Two-Dimensional Hybrid Halide Perovskites: Principles and Promises. *J. Am. Chem. Soc.*, 2019, **141**, 1171–1190.

[46] Z. Yuan, C. Zhou, Y. Tian, Y. Shu, J. Messier, J. C. Wang, L. J. van de Burgt, K. Kountouriotis, Y. Xin, E. Holt, K. Schanze, R. Clark, T. Siegrist and B. Ma, One-dimensional organic lead halide perovskites with efficient bluish white-light emission. *Nat. Commun.*, 2017, **8**, 14051.

[47] M. I. Saidaminov, J. Almutlaq, S. Sarmah, I. Dursun, A. A. Zhumekenov, R. Begum, J. Pan, N. Cho, O. F. Mohammed and O. M. Bakr, Pure Cs_4PbBr_6: Highly Luminescent Zero-Dimensional Perovskite Solids. *Acs Energy Lett.*, 2016, **1**, 840–845.

[48] M. T. Weller, O. J. Weber, P. F. Henry, A. M. Di Pumpo and T. C. Hansen, Complete structure and cation orientation in the perovskite photovoltaic methylammonium lead iodide between 100 and 352 K. *Chem. Commun.*, 2015, **51**, 4180–4183.

[49] D. H. Fabini, C. C. Stoumpos, G. Laurita, A. Kaltzoglou, A. G. Kontos, P. Falaras, M. G. Kanatzidis and R. Seshadri, Reentrant Structural and Optical Properties and Large Positive Thermal Expansion in Perovskite Formamidinium Lead Iodide. *Angew Chem Int Edit*, 2016, **55**, 15392–15396.

[50] S. Ghimire and C. Klinke, Two-dimensional halide perovskites: synthesis, optoelectronic properties, stability, and applications. *Nanoscale*, 2021, **13**, 12394–12422.

[51] L. Zhang, Y. Liu, Z. Yang and S. Liu, Two dimensional metal halide perovskites: Promising candidates for light-emitting diodes. *J. Energy Chem.*, 2019, **37**, 97–110.

[52] G. Long, R. Sabatini, M. I. Saidaminov, G. Lakhwani, A. Rasmita, X. Liu, E. H. Sargent and W. Gao, Chiral-perovskite optoelectronics. *Nat. Rev. Mater.*, 2020, **5**, 423–439.

[53] J. Ma, H. Wang and D. Li, Recent Progress of Chiral Perovskites: Materials, Synthesis, and Properties. *Adv. Mater.*, 2021, **33**, e2008785.

[54] D. G. Billing and A. Lemmerer, Bis [(S)—-phenethylammonium] tribromoplumbate (II). *Acta Crystallogr. Sect. Sect. E: Struct. Rep. Online*, 2003, **59**, m381–m383.

[55] M. Pols, G. Brocks, S. Calero and S. Tao, Temperature-Dependent Chirality in Halide Perovskites. *J. Phys. Chem. Lett.*, 2024, **15**, 8057–8064.

[56] H. Kim, W. Choi, Y. J. Kim, J. Kim, J. Ahn, I. Song, M. Kwak, J. Kim, J. Park, D. Yoo, J. Park, S. K. Kwak and J. H. Oh, Giant chiral amplification of chiral 2D perovskites via dynamic crystal reconstruction. *Sci. Adv.*, 2024, **10**, eado5942.

[57] H. Zhu, K. Miyata, Y. Fu, J. Wang, P. P. Joshi, D. Niesner, K. W. Williams, S. Jin and X.-Y. Zhu, Screening in crystalline liquids protects energetic carriers in hybrid perovskites. *Science*, 2016, **353**, 1409–1413.

[58] A. D. Wright, C. Verdi, R. L. Milot, G. E. Eperon, M. A. Pérez-Osorio, H. J. Snaith, F. Giustino, M. B. Johnston and L. M. Herz, Electron-phonon coupling in hybrid lead halide perovskites. *Nat. Commun.*, 2016, **7**, 11755.

[59] G. R. Berdiyorov, A. Kachmar, F. El-Mellouhi, M. A. Carignano and M. E. Madjet, Role of Cations on the Electronic Transport and Optical Properties of Lead-Iodide Perovskites. *J. Phys. Chem. C*, 2016, **120**, 16259–16270.

[60] L. M. Herz, Charge-Carrier Mobilities in Metal Halide Perovskites: Fundamental Mechanisms and Limits. *Acs Energy Lett.*, 2017, **2**, 1539–1548.

[61] M. Park, A. J. Neukirch, S. E. Reyes-Lillo, M. Lai, S. R. Ellis, D. Dietze, J. B. Neaton, P. Yang, S. Tretiak and R. A. Mathies, Excited-state vibrational dynamics toward the polaron in methylammonium lead iodide perovskite. *Nat. Commun.*, 2018, **9**, 2525.

[62] J. Ibaceta-Jaña, R. Muydinov, P. Rosado, H. Mirhosseini, M. Chugh, O. Nazarenko, D. N. Dirin, D. Heinrich, M. R. Wagner, T. D. Kühne, B. Szyszka, M. V. Kovalenko and A. Hoffmann, Vibrational dynamics in lead halide hybrid perovskites investigated by Raman spectroscopy. *Phys. Chem. Chem. Phys.*, 2020, **22**, 5604–5614.

[63] N. P. Gallop, O. Selig, G. Giubertoni, H. J. Bakker, Y. L. A. Rezus, J. M. Frost, T. L. C. Jansen, R. Lovrincic and A. A. Bakulin, Rotational Cation Dynamics in Metal Halide Perovskites: Effect on Phonons and Material Properties. *J. Phys. Chem. Lett.*, 2018, **9**, 5987–5997.

[64] K. Druzbicki, P. Gila-Herranz, P. Marin-Villa, M. Gaboardi, J. Armstrong and F. Fernandez-Alonso, Cation Dynamics as Structure Explorer in Hybrid PerovskitesThe Case of $MAPbI_3$. *Cryst. Growth Des.*, 2024, **24**, 391–404.

[65] P. Calado, A. M. Telford, D. Bryant, X. Li, J. Nelson, B. C. O'Regan and P. R. F. Barnes, Evidence for ion migration in hybrid perovskite solar cells with minimal hysteresis. *Nat. Commun.*, 2016, **7**, 13831.

[66] Y. Yuan and J. Huang, Ion Migration in Organometal Trihalide Perovskite and Its Impact on Photovoltaic Efficiency and Stability. *Acc. Chem. Res.*, 2016, **49**, 286–293.

[67] D. Weber, $CH_3NH_3PbX_3$, ein Pb(II)-System mit kubischer Perowskitstruktur / $CH_3NH_3PbX_3$, a Pb(II)-System with Cubic Perovskite Structure. *Z. Naturforsch.*, 1978, **33**, 1443–1445.

[68] J. M. Frost, K. T. Butler, F. Brivio, C. H. Hendon, M. van Schilfgaarde and A. Walsh, Atomistic origins of high-performance in hybrid halide perovskite solar cells. *Nano Lett.*, 2014, **14**, 2584–90.

[69] D. A. Egger, A. M. Rappe and L. Kronik, Hybrid Organic–Inorganic Perovskites on the Move. *Acc. Chem. Res.*, 2016, **49**, 573–581.

[70] V. Carpenella, C. Fasolato, D. Di Girolamo, J. Barichello, F. Matteocci, C. Petrillo, D. Dini and A. Nucara, Signatures of Polaron Dynamics in Photoexcited $MAPbBr_3$ by Infrared Spectroscopy. *J. Phys. Chem. C*, 2023, **127**, 22097–22104.

[71] D. J. Kubicki, S. D. Stranks, C. P. Grey and L. Emsley, NMR spectroscopy probes microstructure, dynamics and doping of metal halide perovskites. *Nat. Rev. Chem.*, 2021, **5**, 624–645.

[72] G. M. Bernard, R. E. Wasylishen, C. I. Ratcliffe, V. Terskikh, Q. Wu, J. M. Buriak and T. Hauger, Methylammonium Cation Dynamics in Methylammonium Lead Halide Perovskites: A Solid-State NMR Perspective. *J. Phys. Chem. A*, 2018, **122**, 1560–1573.

[73] D. J. Kubicki, D. Prochowicz, A. Hofstetter, P. Pechy, S. M. Zakeeruddin, M. Gratzel and L. Emsley, Cation Dynamics in Mixed-Cation $MA_xFA_{1-x}PbI_3$ Hybrid Perovskites from Solid-State NMR. *J. Am. Chem. Soc.*, 2017, **139**, 10055–10061.

[74] A. A. Bakulin, O. Selig, H. J. Bakker, Y. L. Rezus, C. Muller, T. Glaser, R. Lovrincic, Z. Sun, Z. Chen, A. Walsh, J. M. Frost and T. L. Jansen, Real-Time Observation of Organic Cation Reorientation in Methylammonium Lead Iodide Perovskites. *J. Phys. Chem. Lett.*, 2015, **6**, 3663–9.

[75] O. Selig, A. Sadhanala, C. Muller, R. Lovrincic, Z. Chen, Y. L. Rezus, J. M. Frost, T. L. Jansen and A. A. Bakulin, Organic Cation Rotation and Immobilization in Pure and Mixed Methylammonium Lead-Halide Perovskites. *J. Am. Chem. Soc.*, 2017, **139**, 4068–4074.

[76] A. Mattoni, A. Filippetti, M. I. Saba and P. Delugas, Methylammonium Rotational Dynamics in Lead Halide Perovskite by Classical Molecular Dynamics: The Role of Temperature. *J. Phys. Chem. C*, 2015, **119**, 17421–17428.

[77] A. Mattoni, A. Filippetti and C. Caddeo, Modeling hybrid perovskites by molecular dynamics. *J. Phys.: Condens. Matter*, 2017, **29**, 043001.

[78] E. Mosconi, C. Quarti, T. Ivanovska, G. Ruani and F. De Angelis, Structural and electronic properties of organo-halide lead perovskites: a combined IR-spectroscopy and ab initio molecular dynamics investigation. *Phys. Chem. Chem. Phys.*, 2014, **16**, 16137–16144.

[79] D. Ghosh, D. Acharya, L. Pedesseau, C. Katan, J. Even, S. Tretiak and A. J. Neukirch, Charge carrier dynamics in two-dimensional hybrid

perovskites: Dion–Jacobson vs. Ruddlesden–Popper phases. *J. Mater. Chem. A*, 2020, **8**, 22009–22022.

[80] F. Brivio, J. M. Frost, J. M. Skelton, A. J. Jackson, O. J. Weber, M. T. Weller, A. R. Goñi, A. M. A. Leguy, P. R. F. Barnes and A. Walsh, Lattice dynamics and vibrational spectra of the orthorhombic, tetragonal, and cubic phases of methylammonium lead iodide. *Phys. Rev. B*, 2015, **92**, 144308.

[81] M. A. Pérez-Osorio, R. L. Milot, M. R. Filip, J. B. Patel, L. M. Herz, M. B. Johnston and F. Giustino, Vibrational Properties of the Organic Inorganic Halide Perovskite $CH_3NH_3PbI_3$ from Theory and Experiment: Factor Group Analysis, First-Principles Calculations, and Low-Temperature Infrared Spectra. *J. Phys. Chem. C*, 2015, **119**, 25703–25718.

[82] T. Glaser, C. Müller, M. Sendner, C. Krekeler, O. E. Semonin, T. D. Hull, O. Yaffe, J. S. Owen, W. Kowalsky, A. Pucci and R. Lovrinčić, Infrared Spectroscopic Study of Vibrational Modes in Methylammonium Lead Halide Perovskites. *J. Phys. Chem. Lett.*, 2015, **6**, 2913–2918.

[83] M. Sendner, P. K. Nayak, D. A. Egger, S. Beck, C. Müller, B. Epding, W. Kowalsky, L. Kronik, H. J. Snaith, A. Pucci and R. Lovrinčić, Optical phonons in methylammonium lead halide perovskites and implications for charge transport. *Mater. Horiz.*, 2016, **3**, 613–620.

[84] C. Quarti, G. Grancini, E. Mosconi, P. Bruno, J. M. Ball, M. M. Lee, H. J. Snaith, A. Petrozza and F. De Angelis, The Raman Spectrum of the $CH_3NH_3Pbl_3$ Hybrid Perovskite: Interplay of Theory and Experiment. *J. Phys. Chem. Lett.*, 2014, **5**, 279–284.

[85] M. Ledinsky, P. Löper, B. Niesen, J. Holovsky, S. J. Moon, J. H. Yum, S. De Wolf, A. Fejfar and C. Ballif, Raman Spectroscopy of Organic-Inorganic Halide Perovskites. *J. Phys. Chem. Lett.*, 2015, **6**, 401–406.

[86] A. M. A. Leguy, A. R. Goñi, J. M. Frost, J. Skelton, F. Brivio, X. Rodríguez-Martínez, O. J. Weber, A. Pallipurath, M. I. Alonso, M. Campoy-Quiles, M. T. Weller, J. Nelson, A. Walsh and P. R. F. Barnes, Dynamic disorder, phonon lifetimes, and the assignment of modes to the vibrational spectra of methylammonium lead halide perovskites. *Phys. Chem. Chem. Phys.*, 2016, **18**, 27051–27066.

[87] A. Létoublon, S. Paofai, B. Rufflé, P. Bourges, B. Hehlen, T. Michel, C. Ecolivet, O. Durand, S. Cordier, C. Katan and J. Even, Elastic Constants, Optical Phonons, and Molecular Relaxations in the High Temperature Plastic Phase of the $CH_3NH_3PbBr_3$ Hybrid Perovskite. *J. Phys. Chem. Lett.*, 2016, **7**, 3776–3784.

[88] R. Lavén, E. Fransson, P. Erhart, F. Juranyi, G. E. Granroth and M. Karlsson, Unraveling the Nature of Vibrational Dynamics in $CsPbI_3$ by Inelastic Neutron Scattering and Molecular Dynamics Simulations. *J. Phys. Chem. Lett.*, 2025, **16**, 4812–4818.

[89] G. Kieslich, J. M. Skelton, J. Armstrong, Y. Wu, F. Wei, K. L. Svane, A. Walsh and K. T. Butler, Hydrogen Bonding versus Entropy: Revealing the Underlying Thermodynamics of the Hybrid Organic–Inorganic Perovskite $[CH_3NH_3]PbBr_3$. *Chem. Mater.*, 2018, **30**, 8782–8788.

[90] O. Yaffe, Y. Guo, L. Z. Tan, D. A. Egger, T. Hull, C. C. Stoumpos, F. Zheng, T. F. Heinz, L. Kronik, M. G. Kanatzidis, J. S. Owen, A. M. Rappe, M. A. Pimenta and L. E. Brus, Local Polar Fluctuations in Lead Halide Perovskite Crystals. *Phys. Rev. Lett.*, 2017, **118**, 136001.

[91] A. N. Beecheri, O. E. Semonin, J. M. Skelton, J. M. Frost, M. W. Terban, H. Zhai, A. Alatas, J. S. Owen, A. Walsh and S. J. L. Billinge, Direct Observation of Dynamic Symmetry Breaking above Room Temperature in Methylammonium Lead Iodide Perovskite. *Acs Energy Lett.*, 2016, **1**, 880–887.

[92] K. Miyata, T. L. Atallah and X. Y. Zhu, Lead halide perovskites: Crystal-liquid duality, phonon glass electron crystals, and large polaron formation. *Sci. Adv.*, 2017, **3**, year.

[93] J. M. Frost, Calculating polaron mobility in halide perovskites. *Phys. Rev. B*, 2017, **96**, year.

[94] H. Seiler, D. Zahn, V. C. A. Taylor, M. I. Bodnarchuk, Y. W. Windsor, M. V. Kovalenko and R. Ernstorfer, Direct Observation of Ultrafast Lattice Distortions during Exciton–Polaron Formation in Lead Halide Perovskite Nanocrystals. *ACS Nano*, 2023, **17**, 1979–1988.

[95] X. X. Wu, L. Z. Tan, X. Z. Shen, T. Hu, K. Miyata, M. T. Trinh, R. K. Li, R. Coffee, S. Liu, D. A. Egger, I. Makasyuk, Q. Zheng, A. Fry, J. S. Robinson, M. D. Smith, B. Guzelturk, H. I. Karunadasa, X. J. Wang, X. Y. Zhu, L. Kronik, A. M. Rappe and A. M. Lindenberg, Light-induced picosecond rotational disordering of the inorganic sublattice in hybrid perovskites. *Sci. Adv.*, 2017, **3**, year.

[96] B. Guzelturk, R. A. Belisle, M. D. Smith, K. Bruening, R. Prasanna, Y. K. Yuan, V. Gopalan, C. J. Tassone, H. I. Karunadasa, M. D. McGehee and A. M. Lindenberg, Terahertz Emission from Hybrid Perovskites Driven by Ultrafast Charge Separation and Strong Electron-Phonon Coupling. *Adv. Mater.*, 2018, **30**, year.

[97] W. D. Cai, C. Y. Kuang, T. J. Liu, Y. Q. Shang, J. Zhang, J. J. Qin and F. Gao, Multicolor light emission in manganese-based metal halide composites. *Appl. Phys. Rev.*, 2022, **9**, 041409.

[98] R. Chiara, M. Morana, G. Folpini, A. Olivati, B. Albini, P. Galinetto, L. Chelazzi, S. Ciattini, E. Fantechi, S. A. Serapian, A. Petrozza and L. Malavasi, The templating effect of diammonium cations on the structural and optical properties of lead bromide perovskites: a guide to design broad light emitters. *J. Mater. Chem. C*, 2022, **10**, 12367–12376.

[99] S. Shao, J. Liu, G. Portale, H.-H. Fang, G. R. Blake, G. H. ten Brink, L. J. A. Koster and M. A. Loi, Highly Reproducible Sn-Based Hybrid Perovskite Solar Cells with 9.

[100] A. Singh, K. M. Boopathi, A. Mohapatra, Y. F. Chen, G. Li and C. W. Chu, Photovoltaic Performance of Vapor-Assisted Solution-Processed Layer Polymorph of $Cs_3Sb_2I_9$. *ACS Appl. Mater. Interfaces*, 2018, **10**, 2566–2573.

[101] T. Zhu, Y. Yang and X. Gong, Recent Advancements and Challenges for Low-Toxicity Perovskite Materials. *ACS Appl. Mater. Interfaces*, 2020, **12**, 26776–26811.

[102] T. Krishnamoorthy, H. Ding, C. Yan, W. L. Leong, T. Baikie, Z. Zhang, M. Sherburne, S. Li, M. Asta, N. Mathews and S. G. Mhaisalkar, Lead-free germanium iodide perovskite materials for photovoltaic applications. *J. Mater. Chem. A*, 2015, **3**, 23829–23832.

[103] A. Babayigit, D. Duy Thanh, A. Ethirajan, J. Manca, M. Muller, H.-G. Boyen and B. Conings, Assessing the toxicity of Pb- and Sn-based perovskite solar cells in model organism Danio rerio. *Sci. Rep.*, 2016, **6**, 18721.

[104] J. P. Cao and F. Yan, Recent progress in tin-based perovskite solar cells. *Energy Environ. Sci.*, 2021, **14**, 1286–1325.

[105] E. C. Schueller, G. Laurita, D. H. Fabini, C. C. Stoumpos, M. G. Kanatzidis and R. Seshadri, Crystal Structure Evolution and Notable Thermal Expansion in Hybrid Perovskites Formamidinium Tin Iodide and Formamidinium Lead Bromide. *Inorg. Chem.*, 2018, **57**, 695–701.

[106] A. E. Maughan, A. M. Ganose, A. M. Candia, J. T. Granger, D. O. Scanlon and J. R. Neilson, Anharmonicity and Octahedral Tilting in Hybrid Vacancy-Ordered Double Perovskites. *Chem. Mater.*, 2018, **30**, 472–483.

[107] C. A. López, M. V. Martínez-Huerta, M. C. Alvarez-Galván, P. Kayser, P. Gant, A. Castellanos-Gomez, M. T. Fernández-Díaz, F. Fauth and J. A. Alonso, Elucidating the Methylammonium (MA) Conformation in $MAPbBr_3$ Perovskite with Application in Solar Cells. *Inorg. Chem.*, 2017, **56**, 14214–14219.

[108] M. Simenas, A. Gagor, J. Banys and M. Maczka, Phase Transitions and Dynamics in Mixed Three- and Low-Dimensional Lead Halide Perovskites. *Chem. Rev.*, 2024, **124**, 2281–2326.

[109] E. Rutherford, Bakerian Lecture: Nuclear constitution of atoms. *Proceedings of the Royal Society of London Series a-Containing Papers of a Mathematical and Physical Character*, 1920, **97**, 374–400.

[110] W. D. Harkins, XXXIX. The constitution and stability of atom nuclei. (A contribution to the subject of inorganic evolution.). *The London, Edinburgh, and Dublin Philosophical Magazine and Journal of Science*, 1921, **42**, 305–339.

[111] J. Chadwick, Possible existence of a neutron. *Nature*, 1932, **129**, 312–312.

[112] R. C. Greenwood and R. E. Chrien, Neutron mass: Measurement of the H1(n,) H2 ray and revised values for selected neutron binding energies. *Phys. Rev. C*, 1980, **21**, 498–502.

[113] G. L. Greene, N. F. Ramsey, W. Mampe, J. M. Pendlebury, K. Smith, W. B. Dress, P. D. Miller and P. Perrin, Measurement of the Neutron Magnetic-Moment. *Phys. Rev. D*, 1979, **20**, 2139–2153.

[114] F. M. Gonzalez, E. M. Fries, C. Cude-Woods, T. Bailey, M. Blatnik, L. J. Broussard, N. B. Callahan, J. H. Choi, S. M. Clayton, S. A. Currie, M. Dawid, E. B. Dees, B. W. Filippone, W. Fox, P. Geltenbort, E. George, L. Hayen, K. P. Hickerson, M. A. Hoffbauer, K. Hoffman, A. T. Holley, T. M. Ito, A. Komives, C. Y. Liu, M. Makela, C. L. Morris, R. Musedinovic, C. O'Shaughnessy, R. W. Pattie, J. Ramsey, D. J. Salvat, A. Saunders, E. I. Sharapov, S. Slutsky, V. Su, X. Sun, C. Swank, Z. Tang, W. Uhrich, J. Vanderwerp, P. Walstrom, Z. Wang, W. Wei, A. R. Young and U. C. Collaboration, Improved Neutron Lifetime Measurement with UCNtau. *Phys. Rev. Lett.*, 2021, **127**, 162501.

[115] R. Hempelmann, *Quasielastic Neutron Scattering and Solid State Diffusion*, Oxford University Press, 2000.

[116] P. C. H. Mitchell, S. F. Parker, A. J. Ramirez-Cuesta and J. Tomkinson, *Vibrational Spectroscopy with Neutrons*, 2005.

[117] D. A. Neumann, Neutron scattering and hydrogenous materials. *Mater. Today*, 2006, **9**, 34–41.

[118] W. E. Fischer, SINQ — The spallation neutron source, a new research facility at PSI. *Physica B*, 1997, **234-236**, 1202–1208.

[119] S. Janssen, J. Mesot, L. Holitzner, A. Furrer and R. Hempelmann, FOCUS: A hybrid TOF-spectrometer at SINQ. *Physica B*, 1997, **234**, 1174–1176.

[120] J. Mesota, S. Janssen, L. Holitzner and R. Hempelmann, FOCUS: Project of a space and time focussing time-of-flight spectrometer for cold neutrons at the Spallation Source SINQ of the Paul Scherrer Institute. *J. Neutron Res.*, 1996, **3**, 293–310.

[121] `https://www.psi.ch/en/sinq/focus/description`.

[122] H. Seto, S. Itoh, T. Yokoo, H. Endo, K. Nakajima, K. Shibata, R. Kajimoto, S. Ohira-Kawamura, M. Nakamura, Y. Kawakita, H. Nakagawa and T. Yamada, Inelastic and quasi-elastic neutron scattering

spectrometers in J-PARC. *Biochimica et Biophysica Acta (BBA) - General Subjects*, 2017, **1861**, 3651–3660.

[123] K. Shibata, N. Takahashi, Y. Kawakita, M. Matsuura, T. Yamada, T. Tominaga, W. Kambara, M. Kobayashi, Y. Inamura and T. Nakatani, *The performance of TOF near backscattering spectrometer DNA in MLF, J-PARC*, 2015.

[124] `https://mlfinfo.jp/en/bl02/`.

[125] R. Lavén, Dynamical properties of metal halide and oxyhydride perovskites. *Thesis*, 2023.

[126] `https://www.isis.stfc.ac.uk/instruments/tosca/`.

[127] D. Colognesi, M. Celli, F. Cilloco, R. J. Newport, S. F. Parker, V. Rossi-Albertini, F. Sacchetti, J. Tomkinson and M. Zoppi, TOSCA neutron spectrometer: The final configuration. *Appl. Phys. A*, 2002, **74**, s64–s66.

[128] S. F. Parker, F. Fernandez-Alonso, A. J. Ramirez-Cuesta, J. Tomkinson, S. Rudic, R. S. Pinna, G. Gorini and J. Fernández Castañon, Recent and future developments on TOSCA at ISIS. *Journal of Physics: Conference Series*, 2014, **554**, 012003.

[129] H. Cavaye and M. Schastny, In situ illumination with inelastic neutron scattering: a study of the photochromic material cis-1,2-dicyano-1,2-bis(2,4,5-trimethyl-3-thienyl)ethene (CMTE). *Phys. Chem. Chem. Phys.*, 2021, **23**, 22324–22329.

[130] W. D. Cai, J. J. Qin, T. Q. Pang, X. Y. Cai, R. X. Jia and F. Gao, Chirality Induced Crystal Structural Difference in Metal Halide Composites. *Adv. Opt. Mater.*, 2022, **10**, 2102140.

[131] R. Shannon, Revised effective ionic radii and systematic studies of interatomic distances in halides and chalcogenides. *Acta Crystallogr. Sect. A*, 1976, **32**, 751–767.

[132] A. Pisanu, A. Mahata, E. Mosconi, M. Patrini, P. Quadrelli, C. Milanese, F. De Angelis and L. Malavasi, Exploring the Limits of Three-Dimensional Perovskites: The Case of $FAPb_{1-x}SnxBr_3$. *Acs Energy Lett.*, 2018, **3**, 1353–1359.

[133] D. J. Kubicki, D. Prochowicz, E. Salager, A. Rakhmatullin, C. P. Grey, L. Emsley and S. D. Stranks, Local Structure and Dynamics in Methylammonium, Formamidinium, and Cesium Tin(II) Mixed-Halide Perovskites from 119Sn Solid-State NMR. *J. Am. Chem. Soc.*, 2020, **142**, 7813–7826.

[134] Z. Guo, Y. Wan, M. Yang, J. Snaider, K. Zhu and L. Huang, Long-range hot-carrier transport in hybrid perovskites visualized by ultrafast microscopy. *Science*, 2017, **356**, 59–62.

[135] D. Ghosh, E. Welch, A. J. Neukirch, A. Zakhidov and S. Tretiak, Polarons in Halide Perovskites: A Perspective. *J. Phys. Chem. Lett.*, 2020, **11**, 3271–3286.

[136] M. Hiraishi, A. Koda, H. Okabe, R. Kadono, K. A. Dagnall, J. J. Choi and S.-H. Lee, Photo-excited charge carrier lifetime enhanced by slow cation molecular dynamics in lead iodide perovskite $FAPbI_3$. *J. Appl. Phys.*, 2023, **134**, 055106.

[137] T. Chen, W.-L. Chen, B. J. Foley and S.-H. Lee, Origin of long lifetime of band-edge charge carriers in organic–inorganic lead iodide perovskites. *Appl. Phys. Sci*, 2017, **114**, 7519–7524.

Appendix A

Working principles of perovskite devices

The brief structures and energy diagrams of common MHP devices are shown in Figure A.1. The general working principle of a perovskite solar cell is that the electrons in the valence band absorb sunlight and transition to the conduction band, passing through the electron transport layer collected by the electrode. The original vacancies of the excited electrons can be regarded as positive charges, called holes, passing through the hole transport layer and

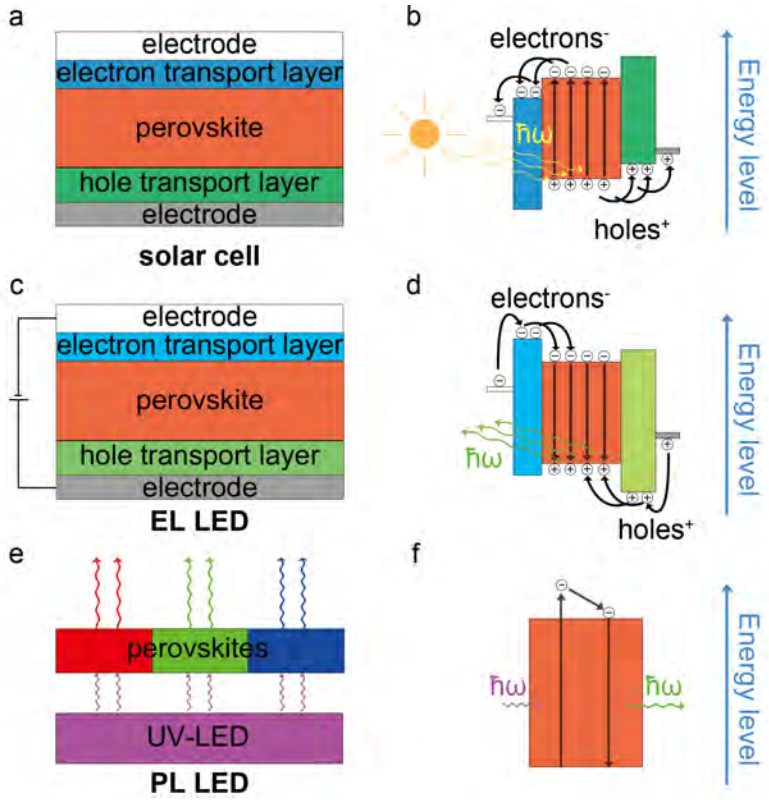

Figure A.1: Schematic of the MHPs devices and energy diagrams including (a) and (b): perovskite solar cell, (c) and (d): electroluminescent (EL) perovskite LED, and (e) and (f): photoluminescent (PL) perovskite LED

being collected by the electrode, thereby converting light energy into electrical energy [Figure A.1(b)]. The working principle of EL perovskite LED is the opposite process to that of a solar cell. Electric energy is input through the electrode from an external voltage source, and electrons are transported to the perovskite layer through the electron transport layer. In the perovskite layer, electrons and holes can have radiative recombination to release photons [Figure A.1(d)]. The working principle of perovskite PL LED is to use a shorter wavelength (ultraviolet or blue light) light source to excite the valence band electrons in perovskites to the conduction band, and then release photons through radiation recombination. This is mainly used to obtain an adjustable emission peak to fabricate the display pixels through the primary colors or to obtain a broader emission peak to obtain white light emission for lighting [Figure A.1(f)]. It is important to point out that the real device structure is usually more complex and can have more layers such as a hole-blocking layer to have better device efficiency and performance.

Appendix B

Several details of neutron scattering theory

B.1 Cross section and scattering length

The incident neutron can be generally described as a plane wave [A.1]:

$$\psi_i(\mathbf{R}) = \frac{1}{\sqrt{Y}} e^{ik\cdot\mathbf{R}} \tag{B.1}$$

where Y represents a normalization constant, and $\mathbf{R}$ is the position operator. The scattered neutron wavefront can be described as a spherical wave [A.1]:

$$\psi_f(\mathbf{R}) = \psi_i(\mathbf{R}_j) \frac{-b_j}{|\mathbf{R}-\mathbf{R}_j|} e^{ik_f|\mathbf{R}-\mathbf{R}_j|} \tag{B.2}$$

where $\mathbf{R}_j$ is the position operator of nuclei j and $|\mathbf{R}-\mathbf{R}_j| \gg b_j$, where b_j is the scattering length which can be considered as the scattering ability/character from the nuclei and it can be found from the wave expansion's first term [A.2]:

$$\lim_{k\to 0} k\cot\delta(k) = -\frac{1}{b_j} \tag{B.3}$$

where $\delta(k)$ is the phase shift of the outgoing spherical wave. The total inelastic scattering cross section can be found [A.1]:

$$\sigma = \int_{4\pi}\int_{-\infty}^{\infty} \frac{d^2\sigma}{d\Omega dE_f} dE_f d\Omega \tag{B.4}$$

$$\frac{d\sigma}{d\Omega} = \int_{-\infty}^{\infty} \frac{d^2\sigma}{d\Omega dE_f} dE_f \tag{B.5}$$

B.2 Correlation functions

Now we consider the situation of scattering interference from multiple nuclei. Considering the scattering as the perturbation $\hat{V}$ and following the Fermi

pseudopotential for nuclear scattering we can get [A.3,A.4]:

$$\hat{V} = \frac{2\pi\hbar^2}{m_n} \sum_j P_j b_j \delta(\mathbf{R} - \mathbf{R}_j) \tag{B.6}$$

where P_j is the statistical weight of the thermal occupancy [A.4]:

$$P_j = \frac{e^{-E_j/k_\mathrm{B}T}}{\sum_n e^{-E_n/k_\mathrm{B}T}} \tag{B.7}$$

and m_n is the neutron mass, R_j is the operator for j_th nucleus position. The initial and final sample states are denoted as $|\lambda_\mathrm{i}\rangle$ and $|\lambda_\mathrm{f}\rangle$, The partial differential cross section for scattering from $|\lambda_\mathrm{i}, k_\mathrm{i}\rangle$ to $|\lambda_\mathrm{f}, k_\mathrm{f}\rangle\rangle$ through the Fermi Golden Rule [A.4,A.5]:

$$\begin{aligned} \left.\frac{d^2\sigma}{d\Omega dE_f}\right|_{\lambda_\mathrm{i}\to\lambda_\mathrm{f}} &= \frac{k_\mathrm{f}}{k_\mathrm{i}} (\frac{m_\mathrm{n}}{2\pi\hbar^2})^2 |\langle\lambda_\mathrm{i} k_\mathrm{i}|\hat{V}|\lambda_\mathrm{f} k_\mathrm{f}\rangle|^2 \delta(E_{\lambda_i} - E_{\lambda_f} + \hbar\omega) \\ &= \frac{k_\mathrm{f}}{k_\mathrm{i}} \sum_{j,j'} \frac{b_j b_{j'}}{2\pi\hbar} \int_{-\infty}^{\infty} \langle e^{-i\mathbf{Q}\cdot\mathbf{R}_j(0)} e^{i\mathbf{Q}\cdot\mathbf{R}_{j'}(t)}\rangle e^{-i\omega t} dt \end{aligned} \tag{B.8}$$

where j' represents the different nuclei which can have different cross-sections when we consider the coherent scattering. We denote thermal averaging by the notation [A.4]:

$$\langle A\rangle \equiv \sum_i p_i \langle\lambda_i|A|\lambda_i\rangle \tag{B.9}$$

where p_i is the Boltzmann probability for the individual states.

The dynamical correlation function as known as the scattering function $S(\mathbf{Q}, \omega)$ is defined as [A.4]:

$$S(\mathbf{Q},\omega) = \sum_{j,j'} \frac{b_j b_{j'}}{2\pi\hbar N} \int_{-\infty}^{\infty} \langle e^{-i\mathbf{Q}\cdot\mathbf{R}_j(0)} e^{i\mathbf{Q}\cdot\mathbf{R}_{j'}(t)}\rangle e^{-i\omega t} dt \tag{B.10}$$

$$\frac{d^2\sigma}{d\Omega dE_f} = \frac{k_\mathrm{f}}{k_\mathrm{i}} N S(\mathbf{Q},\omega) \tag{B.11}$$

where N represents the number of nuclei. From the Fourier transform of the intermediate function over time leads to [A.4]:

$$I(\mathbf{Q},t) = \frac{1}{N} \sum_{j,j'} b_j b_{j'} \langle e^{-i\mathbf{Q}\cdot\mathbf{R}_j(0)} e^{i\mathbf{Q}\cdot\mathbf{R}_{j'}(t)}\rangle \tag{B.12}$$

Applying another Fourier transformation over Q will transform the intermediate correlation function into the space-time correlation function [A.4]:

$$G(\mathbf{R},t) = \frac{1}{(2\pi)^3} \int I(\mathbf{Q},t) e^{-i\mathbf{Q}\cdot\mathbf{R}} d\mathbf{Q} \tag{B.13}$$

B.3 Coherent and incoherent scattering

A sample contains a large amount of different nuclei and isotopes with different cross sections and spin states, which means that when the neutron is scattered by the sample, it may be affected by different nuclei and cause interference. Each nucleus cross section can also be different in time due to the variations of nuclear spin. To explore these problems, assuming that the scattering length of a nucleus in the sample is divided into the time and ensemble mean value $\langle b_j \rangle$ and the local and temporal deviation value δb_j [A.1]:

$$b_j = \langle b_j \rangle + \delta b_j \tag{B.14}$$

where $\langle \delta b_j \rangle = 0$ can be found from the definition. From eq. 3.2, eq. B.2 and eq. B.14, for whole nucleus in the system:

$$\begin{aligned} \langle \frac{d\sigma}{d\Omega} \rangle &= \sum_j \langle (\delta b_j)^2 \rangle + |\sum_j \langle b_j \rangle e^{i\mathbf{Q}\mathbf{R}_j}|^2 \\ &= \frac{d\sigma_{\text{inc}}}{d\Omega} + \frac{d\sigma_{\text{coh}}}{d\Omega} \end{aligned} \tag{B.15}$$

The incoherent quasielastic neutron scattering, which is the main type of scattering involved in this thesis, is caused by atomic self-diffusion. Following the eq. B.8 and B.15, the incoherent part of the double differential of the cross-section can be derived:

$$\left. \frac{d^2\sigma_{\text{inc}}}{d\Omega dE_f} \right|_{\lambda_{\text{i}} \to \lambda_{\text{f}}} = \frac{k_{\text{f}}}{k_{\text{i}}} \sum_j \frac{\langle (\delta b_j)^2 \rangle}{2\pi\hbar} \int_{-\infty}^{\infty} \langle e^{-i\mathbf{Q}\cdot\mathbf{R}_j(0)} e^{i\mathbf{Q}\cdot\mathbf{R}_{j'}(t)} \rangle e^{-i\omega t} dt \tag{B.16}$$

B.4 Jump diffusion models

The jump diffusion model can be described through the probability $p(R_a, t)$ of finding the particle at position r_a at time t with expected residence time τ_a within total N possible sites, and $\tau_{a,b}^{-1}$ is the jump probability from R_a to R_b, then we have:

$$\tau_a^{-1} = \sum_{b=1, b\neq a}^{N} \tau_{a,b}^{-1} \tag{B.17}$$

$$\frac{d}{dt} p(\mathbf{R}_a, t) = \sum_{b=1, b\neq a}^{N} p(\mathbf{R}_b, t) \tau_{b,a}^{-1} - p(\mathbf{R}_a, t) \sum_{b=1, b\neq a}^{N} \tau_{a,b}^{-1} \tag{B.18}$$

Then we can obtain the probability $p(\mathbf{R}_b, t; \mathbf{R}_a, 0)$ which represents the probability the particle at position $\mathbf{R}_a$ at $t = 0$ can be found at position $\mathbf{R}_b$ at t by setting the initial condition $p(\mathbf{R}_a, 0) = 1$ to solve the differential eq. B.18.

we can obtain the incoherent intermediate scattering function $I(\mathbf{Q},t)$ (trans-

fer from the general form eq. B.12):

$$I(\mathbf{Q},t) = \sum_{a=1}^{N} p(\mathbf{R}_a,0)\langle e^{i\mathbf{Q}[\mathbf{R}_a(t)-\mathbf{R}_a(0)]}\rangle \tag{B.19}$$

$$= \sum_{a=1}^{N} p(\mathbf{R}_a,0)[\sum_{b=1}^{N} p(\mathbf{R}_b,t;\mathbf{R}_a,0)e^{i\mathbf{Q}(\mathbf{R}_b-\mathbf{R}_a)}] \tag{B.20}$$

Subsequently, by setting the equilibrium conditions of initial distribution ($t = 0$):

$$p(\mathbf{R}_a,0) = \tau_a / \sum_{n=1}^{N} \tau_n = P_a \tag{B.21}$$

we can obtain the $S(\mathbf{Q},\omega)$ through the Fourier transform of $I(\mathbf{Q},t)$:

$$S(\mathbf{Q},E) = \frac{1}{2\pi}\int I(\mathbf{Q},t)e^{-iEt}dt \tag{B.22}$$

$$= \sum_{a=1}^{N} P_a A_{0\_a}(\mathbf{Q})\delta(\mathbf{Q},E) + \sum_{a=1}^{N} P_a \sum_{b\neq a}^{N} p(\mathbf{R}_b,t;\mathbf{R}_a,0)A_{a,b}(\mathbf{Q})\mathcal{L}_{a,b}(\mathbf{Q},E) \tag{B.23}$$

The structure factors for several common models are presented below:

2-site jump diffusion

The 2-site jump diffusion can be obtained by considering the particle jump between two sites with mean residence time τ_1 and τ_2 and jump distance $d = |\mathbf{R}_1 - \mathbf{R}_2|$, see Figure 3.5(a).[A.4] From eq.3.10:

$$S(Q,E) = A_0(Q)\delta(E) + A_1(Q)\frac{1}{\pi}\frac{\hbar(\tau_1^{-1}+\tau_2^{-1})}{[\hbar(\tau_1^{-1}+\tau_2^{-1}]^2 + E^2} \tag{B.24}$$

$$A_0(Q) = P_1^2 + P_2^2 + 2P_1P_2j_0(Qd) \tag{B.25}$$

$$A_1(Q) = 2P_1P_2[1 - j_0(Qd)] \tag{B.26}$$

Diffusion on a circle

In this model, it is supposed that the particle can only directly go to the nearest two sites on the circle, for instance in Figure 3.5(b), when the particle is on the site $\mathbf{R}_i$ the next jump of it can only jump to $\mathbf{R}_{i-1}$ or $\mathbf{R}_{i+1}$. In other words, $\tau_{i,j}^{-1} = 0$ when $|i-j|>1$. Considering the equivalent site model, N residence

sites are evenly separated on the circle, from eq. 3.10 [A.4,A.6]:

$$S(Q,E) = A_0(Q)\delta(E) + \sum_{i=1}^{N-1} A_i(Q)\frac{1}{\pi}\frac{\hbar/\tau_i}{(\hbar/\tau_i)^2 + E^2} \tag{B.27}$$

$$A_i(Q) = \frac{1}{N}\sum_{n=1}^{N} j_0(Qr_n)cos(\frac{2in\pi}{N}) \tag{B.28}$$

$$r_n = 2r \cdot sin(\frac{n\pi}{N}) \tag{B.29}$$

$$\tau_i^{-1} = 2\tau^{-1}sin^2(\frac{\pi \cdot i}{N}) \tag{B.30}$$

it can be considered as a continuously rotational diffusion when $N \to +\infty$.

Diffusion on a sphere

As known as the isotropic reorientation, it is similar to the underlying logic of the previous model, an equivalent site model is also considered, but considering the spatial angle, see Figure 3.5(c). The function is as follows [A.4,A.6]:

$$S(Q,E) = A_0(Q)\delta(E) + \sum_{i=1}^{\infty} A_i(Q)\frac{1}{\pi}\frac{\hbar/\tau}{(\hbar/\tau)^2 + E^2} \tag{B.31}$$

$$A_i(Q) = (2i+1)j_i^2(Qr) \tag{B.32}$$

$$\tau_i^{-1} = i(i+1)D_{\mathrm{R}} \tag{B.33}$$

where r is the radius of the sphere, D_{R} is the rotational diffusion coefficient (in units of radians^2/s).

Since there are numerous independent variables τ_a, we cannot provide an analytical solution for the $A_{a,b}(\mathbf{Q})\mathcal{L}_{a,b}(\mathbf{Q},\omega)$. But here is the general solution for elastic incoherent structure factor (EISF) $A_0(\mathbf{Q})$ by setting $t \to \infty$. The equilibrium distribution is obtained when $t \to \infty$, $p(R_b, t; R_a, 0) = P_b$ which is independent of the initial site for the particle.

Thus from eq. B.21, B.20 we can have the t independent term $A_0(\mathbf{Q})$ of $I(\mathbf{Q},t)$:

$$I(\mathbf{Q}, t \to \infty) = \sum_{a=1,b=1}^{N} P_a P_b \cdot \cos[\mathbf{Q}(\mathbf{R}_a - \mathbf{R}_b)] \tag{B.34}$$

$$= A_0(\mathbf{Q}) = \mathrm{EISF} \tag{B.35}$$

By Fourier transformation over time:

$$S(\mathbf{Q}, E \to 0) = A_0(\mathbf{Q})\delta(E) \tag{B.36}$$

in the case of a powder sample:

$$\text{EISF} = \frac{1}{4\pi}\int_0^{2\pi} d\varphi \int_0^{\pi} A_0(\mathbf{Q})\sin(\theta)d\theta \tag{B.37}$$

$$= \sum_{a=1,b=1}^{N} P_a P_b \cdot j_0(Q|\mathbf{R}_a - \mathbf{R}_b|) \tag{B.38}$$

where $j_0(x) = \sin(x)/x$ is the zeroth-order spherical Bessel function.

B.5 Detailed balance

It is important to introduce the principle of detailed balance which can help us to understand the asymmetry of the $S(\mathbf{Q},E)$ spectrum, especially at relatively low temperatures (Figure 3.3) [A.1]:

$$\begin{aligned} S(-\mathbf{Q},-E)\Big|_{\lambda_f\to\lambda_i} &= S(\mathbf{Q},E)\Big|_{\lambda_i\to\lambda_f} \\ S(-\mathbf{Q},-E) &= \sum_{\lambda_i,\lambda_f} p_{\lambda_f} S(-\mathbf{Q},-E)\Big|_{\lambda_f\to\lambda_i} \\ &= \sum_{\lambda_i,\lambda_f} p_{\lambda_i} \frac{p_{\lambda_f}}{p_{\lambda_i}} S(\mathbf{Q},E)\Big|_{\lambda_i\to\lambda_f} \\ &= e^{-E/(k_B T)} S(\mathbf{Q},E)\Big|_{\lambda_i\to\lambda_f} \end{aligned} \tag{B.39}$$

where k_B is the Boltzmann constant, T is the temperature. It is a vital step that applies the detail balance before the $S(\mathbf{Q},E)$ spectrum fitting with the QENS signal fitted by the symmetric lorentzians.

Appendix References

[A.1] K. Lefmann, *Neutron scattering: Theory, instrumentation, and simulation*, 2021.

[A.2] S. Weinberg, *Lectures on Quantum Mechanics*, Cambridge University Press, Cambridge, 2nd edn, 2015.

[A.3] E. Fermi, Sul moto dei neutroni nelle sostanze idrogenate. *Ric. Sci.*, 1936, **7**, 13–52.

[A.4] R. Hempelmann, *Quasielastic Neutron Scattering and Solid State Diffusion*, Oxford University Press, 2000.

[A.5] E. Fermi, *Nuclear physics: a course given by Enrico Fermi at the University of Chicago*, University of Chicago press, 1950.

[A.6] M. Bée, *Quasielastic neutron scattering*, Adam Hilger, United Kingdom, 1988.